UNIVERSIDADE FEDERAL DO CEARÁ
CENTRO DE TECNOLOGIA
DEPARTAMENTO DE ENGENHARIA ESTRUTURAL E CONSTRUÇÃO CIVIL
PROGRAMA DE PÓS-GRADUAÇÃO EM ENGENHARIA CIVIL

LUCAS BENÍCIO RODRIGUES ARAÚJO

RHEOLOGICAL, MECHANICAL AND DURABILITY EVALUATION OF ALKALI-ACTIVATED PASTES AND CONCRETES DESIGNED BASED ON FLY ASH AND STEEL SLAG

FORTALEZA

2023

LUCAS BENÍCIO RODRIGUES ARAÚJO

RHEOLOGICAL, MECHANICAL AND DURABILITY EVALUATION OF ALKALI-ACTIVATED PASTES AND CONCRETES DESIGNED BASED ON FLY ASH AND STEEL SLAG

M.Sc. thesis presented to the Post-Graduate Program in Structures and Civil Construction, as a partial fulfillment of the requirements for the Master's degree in Civil Engineering at Federal University of Ceará.
Area within the Graduate Program: Civil Construction

Advisor: Prof. Lucas Feitosa de Albuquerque Lima Babadopulos Ph.D.

FORTALEZA

2023

Dados Internacionais de Catalogação na Publicação
Universidade Federal do Ceará
Sistema de Bibliotecas
Gerada automaticamente pelo módulo Catalog, mediante os dados fornecidos pelo(a) autor(a)

A69r Araújo, Lucas Benício Rodrigues.
Rheological, mechanical and durability evaluation of alkali-activated pastes and concretes designed based on fly ash and steel slag / Lucas Benício Rodrigues Araújo. – 2023.
144 f. : il. color.

Dissertação (mestrado) – Universidade Federal do Ceará, Centro de Tecnologia, Programa de Pós-Graduação em Engenharia Civil: Estruturas e Construção Civil, Fortaleza, 2023.
Orientação: Prof. Dr. Lucas Feitosa de Albuquerque Lima Babadopulos .

1. Alkali-activated pastes and concretes. 2. Steel slag. 3. Fly ash. 4. Mechanical and rheological characterization. 5. Mix design. I. Título.

CDD 624.1

LUCAS BENÍCIO RODRIGUES ARAÚJO

RHEOLOGICAL, MECHANICAL AND DURABILITY EVALUATION OF ALKALI-ACTIVATED PASTES AND CONCRETES DESIGNED BASED ON FLY ASH AND STEEL SLAG

M.Sc. thesis presented to the Post-Graduate Program in Structures and Civil Construction, as a partial fulfillment of the requirements for the Master's degree in Civil Engineering at Federal University of Ceará.
Area within the Graduate Program: Civil Construction

Advisor: Prof. Lucas Feitosa de Albuquerque Lima Babadopulos Ph.D.

Approved in: 04/05/2023.

COMMITTEE

_____

Prof. Lucas Feitosa de Albuquerque Lima Babadopulos Ph.D (advisor)
Federal University of Ceará

_____

Prof. Dra. Juceline Batista dos Santos Bastos
Federal Institute of Science and Technology of Ceará (IFCE)

_____

Prof. Dr. Antonio Eduardo Bezerra Cabral
Federal University of Ceará

_____

Prof. Antonin Fabbri Ph.D
Ecole Nationale des Travaux Publics de l'Etat (ENTPE) of the University of Lyon

ACKNOWLEDGEMENTS

Gostaria de agradecer a minha mãe Marleny Benício que sempre foi um exemplo de fé e persistência. A minha irmã Fernanda Benício e ao meu cunhado Kayo Soeiro que sempre me deram suporte na minha jornada docente. Ao meu pai Gilberto Rodrigues que foi meu exemplo de docência e caráter. Aos meus avós Odilon e Ruth, que sempre me incentivaram a estudar.

A minha parceira no mestrado e na vida Leonária Araújo, que percorreu toda essa jornada ao meu lado e que fez os meus dias ficarem melhores nos momentos difíceis. Aos meus amigos mais próximos no mestrado Madson Lucas, Ana Karoliny, Andressa Cristina, Danilo Morais, Daniel Lira, Alverne Paiva, Wanner Kelly, e Lucas Sassaki que me acompanharam nessa jornada produzindo conhecimento, criando laços e dividindo esse percurso.

À Universidade Federal do Ceará e ao Programa de Pós-Graduação em Engenharia Civil por terem sido a mola-mestre na obtenção dos meus conhecimentos nas diversas áreas da construção civil ao longo dos 2 últimos anos. Que auxiliaram o meu crescimento profissional nessa etapa da minha jornada para a docência no ensino superior.

Ao meu orientador, professor Dr. Lucas Babadopulos, que me acompanhou e guiou no desenvolvimento dessa e de outras pesquisas e me levou a produzir estudos bem fundamentados e de alta relevância. Me fez refletir sobre os limites do conhecimento e evoluir como pessoa e profissional. Além de me fazer perceber que a pesquisa pode mudar a minha realidade e me lavar a um mundo ao qual eu nem considerava estar por nunca ter tido contato.

Ao professor Antonin Fabri Ph.d e ao corpo técnico do LTDS que me receberam e me ensinaram muito durante o estágio desenvolvido em Lyon. Além de me motivar a continuar como pesquisador e ingressar no doutorado.

À professora Dra. Heloina Costa, que me motivou a estudar essa área e me forneceu suporte técnico no desenvolvimento da dissertação e de outras pesquisas.

Aos professores Dra. Juceline Bastos e Dr. Eduardo Cabral por contribuírem diretamente para o desenvolvimento e melhoria desse estudo com intervenções imprescindíveis.

Ao Laboratório de Materiais e Construção Civil (LMCC) e ao seu corpo técnico. Em especial, aos profissionais Helano, Paulo Vitor e Manoel, quem me auxiliaram tecnicamente, na produção e avaliação dos ligantes e concretos álcali-ativados.

Ao Laboratório de Mecânica dos Pavimentos (LMP) e ao seu corpo técnico. Em especial, aos profissionais Johnny, Flávia, Wesley e Assis, que me ajudaram nas análises químicas e reológicas.

A Empresa Cimento Apodi, por fornecer as cinzas volantes utilizadas nessa pesquisa. À Companhia Siderúrgica do Pecém (CSP), por fornecer as escórias utilizadas nessa pesquisa. À empresa Shimadzu, pela realização de alguns ensaios nos materiais da pesquisa.

Agradeço também a todas as outras pessoas ou instituições que colaboraram direta ou indiretamente para a realização da presente pesquisa.

“The knowledge frontiers have no limits. The more you acquire knowledge, the more you realize how much you still must learn. Knowledge is a powerful tool, and it can change the world, including your own.”

(Babadopulos adapted from Platão, 2022)

ABSTRACT

The development of societies presents a high impact on the environment, which includes the consumption of natural resources, environmental pollution with greenhouse gases, and a high generation of solid waste. Portland cement production is one of the main causes of such impacts, and the search for more sustainable materials to replace it is a challenge to overcome. In this scenario, there are the Alkali-Activated Binders (AAB), frequently called "geopolymers" in the literature related to construction. This is a new generation of non-hydraulic binders, activated by the reaction of precursors, composed of aluminosilicate sources, associated with alkaline activators. It can represent a reduction in CO_2 emissions between 55% and 75% compared to Portland cement concrete. Thus, this MSc work focuses on the evaluation of alkali-activated pastes and concretes produced based on fly ash (FA) and steel slag (SS) precursors with alkaline activators composed of different proportions of sodium hydroxide and sodium silicate. The experimental approach was distributed in three stages. The first stage focused on the development the design procedure to formulate and mechanically evaluate AAB pastes and concrete. In this stage, 36 binder's formulations were evaluated by compressive strength, aiming to achieve 60 MPa under thermal curing. They were composed by silica modulus (S/N) of the activator of 0.75, 1.25 and 1.75, alkali dosage (N%) of 6%, 8% and 10%, proportions of FA to basic oxygen furnace (BOF) SS from 50% to 50% and 75% to 25%, and ambient and thermal curing (65 ^{o}C). At this stage, it was found that lower silica modulus and lower alkali dosage were beneficial to the increase of compressive strength. An AAB paste based on N% of 10%, S/N of 0.75 and 75% to 25% of FA to SS proportion presented a suitable combination to produce concrete with high slump flow (575 mm) and compressive strength (64 MPa). The second stage focused on the multipoint rheological characterization of pastes and concretes. The tests were performed using flow tests and oscillatory tests in wither a bench dynamic shear rheometer for pastes or using a planetary rheometer for concretes. The pastes presented a plastic viscosity of 1.63 Pa.s to 10.1 Pa.s and no yield stress and the AAB concrete exhibited 3 times higher mixing energy than Portland cement concrete. Both paste and concrete had rheological behaviors that were well-adjusted by pseudoplastic models. The third stage focused on assessing the impact of replacing conventional aggregates by Baosteel's Slag Short Flow (BSSF) SS aggregates on the fresh and hardened state properties, besides the characterization of the concretes regarding durability. The concretes presented good passing ability, but slow flow related to the high viscosity of the activator. In the hardened state, the concretes with conventional aggregate showed better mechanical performance, with compressive strength of 64 MPa and Young's modulus up to 26.2 GPa, under thermal curing. The utilization of steel slag aggregates produced a decrease in compressive strength, to values of 49.6 MPa under thermal curing, but an improvement in self-compacting properties, reaching slump flow values of 737 mm. Compared to conventional concrete, AAB concrete presented controversial indications of durability, with low water penetration under pressure but high indications of chloride ion penetration, based on electrical measurements. In other words, conflicting conclusions depend on the chosen tests, which suggests that further research is necessary for developing proper methods for durability analysis. At the end of the study, knowledge about AAB pastes and concretes was produced, as well as an efficient mix design methodology.

Keywords: Alkali-activated pastes and concretes; Steel slag; Fly Ash; Mechanical and rheological characterization; Mix design.

RESUMO

O desenvolvimento das sociedades apresenta um alto impacto sobre o meio ambiente, que inclui o consumo de recursos naturais, poluição ambiental e uma alta geração de resíduos sólidos. A produção de cimento Portland é uma das principais causas de tais impactos, e a busca por materiais mais sustentáveis para substituí-la é um desafio a ser superado. Neste cenário, existem os ligantes álcali-ativados (LAA), frequentemente chamados de "geopolímeros" na literatura relacionada à construção. Trata-se de uma nova geração de ligantes não-hidráulicos, ativados pela reação de precursores, compostos de fontes de aluminosilicatos, associados a ativadores alcalinos. Vale ressaltar que o uso de LAAs pode representar uma redução nas emissões de CO_2 entre 55% e 75% em comparação com o cimento Portland. Assim, este estudo de mestrado concentra-se na formulação e caracterização de pastas e concretos alcalinos ativados à base de cinzas volantes (CV) e de escórias de aciaria (EA) com ativadores alcalinos compostos de diferentes proporções de hidróxido de sódio e silicato de sódio. A abordagem experimental adotada foi distribuída em três etapas. A primeira etapa focou no desenvolvimento de uma metodologia de dosagem aplicada em pastas e concretos de LAA. Nesse estágio, 36 formulações de pastas foram avaliadas à resistência compressão, visando atingir 60 MPa sob cura térmica (65 ^{o}C). Elas foram compostas pelo módulo de sílica (S/N) do ativador de 0,75, 1,25 e 1,75, teor de álcalis (N%) de 6%, 8% e 10%, proporções de CV para EA do tipo basic oxygen furnace (BOF) de 50% para 50% e 75% para 25%, e cura ambiente e térmica (65 ^{o}C). Nesta fase, verificou-se que módulos de sílica e teores de álcalis menores são benéficos para o aumento da resistência à compressão. A pasta com 10% de N%, S/N de 0,75 e 75% a 25% da proporção FA a EA apresentou combinação adequada para produzir concreto com alto slump flow (575 mm) e resistência à compressão (64 MPa). A segunda etapa concentrou-se na caracterização reológica pastas e concretos de AAL. Os testes foram realizados utilizando ensaios de fluxo e oscilatórios em um reômetro de cisalhamento dinâmico de bancada para pastas ou utilizando um reômetro planetário para concretos. As pastas de LAA apresentaram uma viscosidade plástica de 1,63 Pa.s a 10,1 Pa.s e sem tensão de escoamento e o concreto de LAA exibiu 3 vezes mais energia de mistura que o concreto de cimento Portland. Tanto a pasta quanto o concreto apresentaram comportamentos reológicos bem ajustados pelos modelos pseudoplásticos. A terceira etapa se concentrou em avaliar o impacto da substituição de agregados convencionais por agregados de EA do tipo baosteel's slag short flow (BSSF) nas propriedades de estado fresco e endurecido, além da caracterização em relação à durabilidade. Os concretos apresentavam boa habilidade passante, mas fluxo lento. No estado endurecido, o concreto com agregado convencional apresentou melhor desempenho mecânico, com resistência à compressão de até 64 MPa e módulo de elasticidade de até 26,2 GPa, sob cura térmica. A utilização de agregados de EA produziu uma diminuição na resistência à compressão, para valores de 49,6 MPa, sob cura térmica, mas melhora nas propriedades de autoadensáveis, atingindo valores slump flow de 737 mm. Em comparação com o concreto convencional, o concreto de LAA apresentou baixa penetração de água sob pressão, mas altas indicações de penetração de íons cloreto, com base em medições elétricas. Em outras palavras, houve conclusões conflitantes dependendo dos testes escolhidos, o que sugere que são necessárias mais pesquisas para e análise da durabilidade. No final do estudo, foram produzidos conhecimentos sobre pastas e concretos álcali-ativados, assim como uma metodologia de dosagem eficiente.

Palavras-chave: Pastas e concretos álcali-ativados; Escórias de aciaria; Cinzas volantes; Caracterização mecânica e reológica; Dosagem de mistura.

LIST OF FIGURES

Figure 1.1 - Research motivations..... 21
Figure 2.1 - Field application of alkali-activated concretes...……. 24
Figure 2.2 - Timeline of alkali-activated binders development……. 25
Figure 2.3 - Main products of alkaline activation…….,……. 26
Figure 2.4 - Potential products of alkaline activation…….....…….. 26
Figure 2.5 - Alkali-activation process……...…..…….. 27
Figure 2.6 - Structure of C-A-S-H gels……...……..…… 28
Figure 2.7 - Structure of N-A-S-H gels……...…….. 28
Figure 2.8 - Mix design methodologies of alkali-activated binders…….. 30
Figure 2.9 - Conventional concrete x Alkali-activated concrete..... 31
Figure 2.10 - Ternary diagram of different alkali-activeted binders' compositions…… 32
Figure 2.11 - Fly Ash obtaining process……...……... 33
Figure 2.12 - Thermoelectric Complex Production of Pecém……. 34
Figure 2.13 - Production process for steel slag…… 35
Figure 2.14 - Siderurgical Complex of Pecém..... 36
Figure 2.15 - Alkali-activated mixtures: paste to concrete……..…… 38
Figure 2.16 - Relevant research regarding steel slag as a precursor in AAB……..... 40
Figure 2.17 - Background of UFC's research conducted in this area…….. 42
Figure 3.1 - Schematic illustration of alkali-activated mixtures ……... 45
Figure 3.2 - SEM images of precursors ……..……...…… 49
Figure 3.3 - Mix design of alkali-activated pastes and concrete …….. 50
Figure 3.4 - Alkali-activated pastes aspect ……...…… 52
Figure 3.5 - Alkali-activated binder in the concrete application …….. 53
Figure 3.6 - Summary of binder mix design ……..……... 56
Figure 3.7 - 28 days compressive strength results of AAB pastes ……..……. 58
Figure 3.8 - Compressive strength at 28 days of AAB pastes …….. 59
Figure 3.9 - 28-day flexural strength results of AAB, ambient cured ……..... 61
Figure 3.10 - Setting time of AABs pastes 3, 5 and 11……..……. 61
Figure 3.11 - Spreading diameter by the mini-slump method, for pastes 3, 5 and 11…. 62
Figure 3.12 - Compressive strength of AABs pastes 3, 5 e 11…….……... 63
Figure 3.13 - Compressive strength over time of AAB paste 3 …….. 64
Figure 3.14 - SEM/EDS aspect of gels formed by AAB paste 3..……... 65

Figure 3.15 - Compressive strength of AAB concretes at 28 days..…… 66
Figure 4.1 - Rheology tests photographs on (a) AAB pastes, (b) AAB concretes…… 73
Figure 4.2 - The particle size distribution of the investigated precursors …… 74
Figure 4.3 - The particle size distribution of the investigated aggregates …… 75
Figure 4.4 - Schematical representation for the rheological tests procedure on AAB pastes ……...…… 78
Figure 4.5 - Procedure for the oscillatory rheological test of AAB pastes…… 80
Figure 4.6 - Schematical representation for the rheological tests procedure on AAB concretes ……...……... 81
Figure 4.7 - Results of the loading histories from the flow tests (a) 10 min., (b) 60 min..... 83
Figure 4.8 - Flow test results based on Bingh. model approach: Shear stress vs. Shear rate…….. 84
Figure 4.9 - Flow test results based on pseudoplastic model approach: Shear stress vs. Shear rate……..……..……..……..…… 85
Figure 4.10 - Flow test results based on pseudoplastic model approach: Apparent viscosity vs. Shear rate ……..……..……..……..…….. 86
Figure 4.11 - Results (storage modul., loss modul. and phase angle over time) from the oscillatory tests……..……..……..……..…….. 87
Figure 4.12 - SEM images of AAB under ambient cure for: a) M1; b) M2; c) M3…… 88
Figure 4.13 - SEM images of AAB under thermal cure for: a) M1; b) M2; c) M3……. 88
Figure 4.14 - Mixing test results of mortars and concretes: Torque vs. Time …..…….. 89
Figure 4.15 - Flow test results of mortars and concretes: Torque vs. Rotation speed vs. Apparent viscosity ……...……. 90
Figure 4.16 - Concretes and mortars results based on pseudopl. model approach: Torque vs. Rot.speed……..... 91
Figure 4.17 - Compressive strength of alkali-activated concretes……... 93
Figure 5.1 - Precursors PSD……..……...……. 98
Figure 5.2 - Aggregates PSD ……...……..... 100
Figure 5.3 - Aspect of sections of the produced AAB concretes ……. 101
Figure 5.4 - Void content analysis (a) natural aggregate and (b) BSSF type steel slag aggregate……..... 102

Figure 5.5 - Compressive strength of AAB concretes with conventional and BSSF-SS aggregates, at 28 days …….……..…….. 108
Figure 5.6 - Comparison between the methods for determining Young´s modulus for AABs concretes, at 28 days.……... 109
Figure 5.7 - Bulk electrical resistivity of AAB concretes, at 28 days …….……. 112
Figure 5.8 - Rapid chloride ion penetration test of AAB concretes, under thermal cure, at 28 days……. 113
Figure 5.9 - Water penetration under pressure of AABs concretes under thermal cure, at 28 days……. 114
Figure 5.10 - SEM images of AAB paste, at 28 days ……..... 115
Figure 5.11 - Microstructure of the interface zone of AAB concretes with conventional aggregates, at 28 days……. 116
Figure A.1 - Standardized residuals presented by the compressive strength tested species……..... 141
Figure A.2 - Duncan test for alkali-activated binders……..... 142

LIST OF TABLES

Table 3.1 -	Chemical composition of precursors…….…….……..	49
Table 3.2 -	Binder mix design experimental verification, 36 combinations….....	51
Table 3.3 -	Formulations design for the initial assessment of the pastes mix design..	54
Table 3.4 -	AAB concrete formulation…….……..……..	56
Table 4.1 -	Chemical composition of the investigated steel slag and fly ash……...	74
Table 4.2 -	Mix proportions of AAB pastes…….……..……..……	75
Table 4.3 -	Mix proportions of AAB concrete…….……..……..	76
Table 4.4 -	Slopes evaluation of AAB pastes.....	85
Table 4.5 -	Mixing step results ……...……	90
Table 4.6 -	Fresh state test results for alkali-activated concretes…….	92
Table 5.1 -	Chemical composition of precursors by XRF……	99
Table 5.2 -	Aggregates physical properties…….……...…..…….	100
Table 5.3 -	Mix parameters of AAB concretes…….…….....	102
Table 5.4 -	Results of fresh state AAB concretes…….……	106
Table 5.5 -	Poisson's ratio value for equivalence between ultrasonic and the others Young´s modulus…….	111
Table A.1 -	Complete results of AABs compressive strengths at 28 days, ambient curing…….…….…….…….…….…….…….…….....	139
Table A.2 -	Complete results of AABs compressive strengths at 28 days, thermal curing…….…….…….…….…….…….…….…….....	140
Table A.3 -	Complete result of the flexural strength at 28 of the AABs, ambient curing…..…..…..…..…..…..…..…..…..…..…..……..…….	140
Table A.4 -	Abbreviations used for statistical analysis…….	141
Table A.5 -	Compressive strength at 7 days of pastes 3, 5 and 11……	143
Table A.6 -	Compressive strength of paste S/N 0.75, N% 6%, FA-SS 75-25, several ages……...	143
Table A.7 -	Compressive strength of alkali-activated concretes……...	143
Table A.8 -	Ultrasonic pulse velocity (m/s) of alkali-activated concretes, 28 days.....	144
Table A.9 -	Young's modulus of alkali-activated concretes, 28 days……...	144
Table A.10 -	Electrical resistivity (kΩ) of alkali-activated concretes, 28 days……..	144
Table A.11 -	Alkali-activated concrete chloride ion penetrability (Coulomb), 28 days	144

LIST OF ABBREVIATIONS AND ACRONYMS

AAB	Alkali-Activated Binders
ABNT	Associação Brasileira de Normas Térmicas (Technical Standards Brazilian Association)
ASTM	American Society for Testing and Materials
Al_2O_3	Alumina or Aluminum Oxide
BOF	Basic Oxygen Furnace
BSI	Brazilian steel institute (Instituto Aço Brasil)
BSSF	Baosteel's Slag Short Flow
C-A-S-H	Gel composed of CaO-Al_2O_3-SiO_2-H_2O
CaO	Calcium oxide
CSP	Companhia Siderurgica do Pecém (Pecém Steelmaking Company)
EN	European Standards
FA	Fly Ash
Fe_2O_3	Iron oxide
GHG	Greenhouse Gas missions
GGBFS	Ground Granulated Blast-Furnace Slag
HPSCC	High-Performance Self-Compacting Concrete
KR	Kambara Reactor
MK	Metakaolin
MgO	Magnesium Oxide
N%	Alkali dosage
NBR	Norma Brasileira Regulamentada (Brazilian Standard)
N-A-S-H	Gel composed of Na_2O-Al_2O_3-SiO_2-H_2O
Na_2SiO_3	Sodium Silicate
NaOH	Sodium Hydroxide
OPC	Ordinary Portland Cement
P%	Paste content
PCC	Portland Cement Concrete
SEM	Scanning Electron Microscope
S/N	Silica Modulus
SS	Steel Slag

TABLE OF CONTENTS

1 INTRODUCTION 18

1.1 Research objectives 21

1.1.1 Main Objective 21

1.1.2 Specific Objectives 21

1.2 Manuscript structure 22

2 LITERATURE REVIEW 24

2.1 Alkali-activated binders 24

2.2 Formulation of alkali-activated binders 29

2.3 Precursors and aggregates 31

2.3.1 Fly ash 32

2.3.2 Steel slag 34

2.4 Alkaline activators 37

2.5 Characterization of alkali-activated mixtures 38

2.6 Main studies on alkali-activated binders 38

2.7 Background of the research developed in the UFC 41

3 DESIGN AND EVALUATION OF ALKALI-ACTIVATED PASTES AND CONCRETES PRODUCED WITH FLY ASH AND STEEL SLAG 43

3.1 Introduction 43

3.1.1 General Motivation for the Research 43

3.1.2 Mix design strategies for alkali-activated binders and concretes and the specific motivation of this study 46

3.1.3 Research objective and basic scope of materials 48

3.2 Materials 48

3.3 Mix design procedure for alkali-activated binder (AAB) pastes and concrete 50

3.3.1 Proposed general scheme for an alkali-activate mix design method 50

3.3.2 Pastes and concrete mix designs 53

3.3.3 Mixture, specimens manufacturing and testing procedure 56

3.4 Compressive strength and complementary tests in the fresh and hardened states . 58

3.4.1 Alkali-activated pastes 58

3.4.2 Alkali-activated concrete 65

3.5 Conclusions 67

4 RHEOLOGICAL EVALUATION OF HIGH-STRENGTH SELF-COMPACTING ALKALI-ACTIVATED MATERIALS PRODUCED WITH FLY ASH AND STEEL SLAG 70

4.1 Introduction 71

4.2 Materials and mix design 73

4.2.1. Materials 73

4.2.2. Mix Design of Alkali-Activated Binder (AAB) pastes and concretes 75

4.2.3 Mixing procedure of AAB pastes and concretes 76

4.3 Experimental methods 77

4.3.1 Setting time 77

4.3.2 Rheological tests 77

4.3.3 Microstructure AAB pastes analysis 81

4.3.4 Fresh and hardened states tests on AAB concretes 81

4.4 Results and discussion 82

4.4.1 AAB pastes 82

4.4.2 AAB concrete 89

4.5 Conclusions 93

5 HIGH-PERFORMANCE SELF-COMPACTING ALKALI-ACTIVATED CONCRETE, BASED ON FLY ASH AND STEEL SLAG, WITH CONVENTIONAL AND STEEL SLAG AGGREGATES 95

5.1 Introduction 95

5.2 Materials and methods 98

5.2.1 Constituent materials of the AAB concrete 98

5.2.2 AAB concretes mix proportions 100

5.2.3 Mixing, fresh state properties and specimen fabrication 102

5.2.4 Mechanical Properties 103

5.2.5 Durability properties: chloride ion penetration; microstructure; porosity 104

5.3 Results and discussions 106

5.3.1 Self-compacting evaluation 106

5.3.2 Mechanical evaluation 107

5.3.3 Durability evaluation 111

5.4 Conclusions 117

6 FINAL CONSIDERATIONS AND SUGGESTION FOR FUTURE RESEARCH 119

6.1 Final considerations 119

6.2 Future research suggestions 120

REFERENCES 122

APPENDIX A - RESULTS OF THE ALKALI-ACTIVATED MIXTURES 139

1 INTRODUCTION

Civil construction is one of the sectors that most impact the environment, in terms of waste generation, energy use and natural reserves (TRINDADE et al., 2020), especially in the production of conventional concrete due to the use of Portland cement. Its production to supply the global demand is responsible for 5% to 7% of the world's CO_2 production, one of the main gases associated with the greenhouse effect (SINGH; MIDDENDORF, 2019). In 2020, Brazilian cement production was 61 million tons (SINDICATO NACIONAL DA INDÚSTRIA DE CIMENTO, 2020).

The tendency in productive sectors is the demand for solutions and more sustainable products. The main motivation is the comprehension of the utilization limit of natural resources and the necessity of rational use as a strategic factor for economic advancement. However, the construction industry presents limited advances compared to other productive sectors. This can be attributed to the sector's organizational culture or the use of inefficient processes (DELGADO et al., 2019). The construction industry is pointed out as one of the largest producers of environmental liabilities compared to other segments. This occurs due to the high aggregate energy demand and the huge consumption of non-renewable raw materials, being responsible for 60% of the material extracted from the earth's surface (BRIBIBIÁN; CAPILLA; USÓN, 2011).

In this context, several studies have been developed to replace the components of conventional concrete partially or completely with products with less environmental impact. The main industrial by-products and wastes are metakaolin, silica fume, nano-silica, fly ash, blast furnace slag, steel slag (RAMANATHAN et al., 2013; ALMEIDA, 2014; ZHANG et al., 2020) and construction waste (SANTOS; DA SILVA; DE BRITO, 2019). These applications reduce the environmental impact, due to the lower extraction of new raw materials, and can reduce the final cost of concrete. Recommendations from CONAMA's Resolution 307:2002 and Brazilian Law 12,305:2010, which is responsible for the National Solid Waste Policy.

The development of new materials with lower environmental impact and superior properties is required. In this scenario, Alkali-Activated Binders (AABs) appear as a new generation of non-hydraulic binders that figure as an alternative to Portland cement, with the potential to reduce CO_2 emissions (SUMESH et al., 2017). Their use can represent a reduction rate in CO_2 emissions between 55% and 75% compared to Portland Cement Concrete - PCC (YANG; SONG; SONG, 2012). The AABs are obtained by alkaline activation of an aluminosilicate precursor combined with a highly concentrated alkaline solution, resulting in a

structure amorphous to semi-crystalline (ZERZOURI et al., 2021). This material presents several names and often appears commercially under the name of geopolymer (LI et al., 2019), even when it does not present a geopolymeric structure.

Several materials are used as a source of aluminosilicates in precursors of alkali-activated binders, being more consolidated in the studies involving Fly Ash (FA), Ground Granulated Blast Furnace Slag (GGBFS) and Metakaolin (MK) (ZHANG et al., 2020, XIE et al., 2020). However, there are still precursors barely explored and with insufficient applications to consume their production. Among them, it is the Steel Slag (SS), which originated from the process of transformation of pig iron into steel (NUNES; BORGES, 2021). To understand the generation of steel slag, it is necessary to analyze how much steel is produced and how much steel slag is generated during this production. In Brazil, 31.4 million tons of steel are produced per year, and Ceará produces 2.8 million tons of this total (INSTITUTO AÇO BRASIL, 2021). Approximately, each ton of steel produced generates between 100 kg and 120 kg of steel slag (HORII et al., 2015). Moreover, of the total produced annually, only 36% of this slag is sold (INSTITUTO AÇO BRASIL, 2018). Using these data, it is possible to estimate the Brazilian production of steel slag to 3.54 thousand tons per year, but only 1.24 thousand tons are sold, being necessary to find new uses for the material. It is worth mentioning that 74.5% of the steel produced is obtained using the system called Basic Oxygen Furnace - BOF (BSI, 2021). Thus, steel slag still presents itself as an environmental liability and research show that its application as an alkali-activated binder may present a way to reduce this problem (NUNES; BORGES, 2021).

ABBs based on slag usually have a fast setting time (XIE et al., 2020) and can have their properties improved when produced in combined with other precursors, especially when combined with fly ash. When properly combined, these materials produce AAB of high strength and adequate setting time for field application (RAFEET et al., 2017; HADI; ZHANG; PARKINSON, 2019). Moreover, even though fly ash is already used on a large scale, mainly as an addition to commercial Portland cements of types of CP II-Z and CP IV, there is still a production excess. It is estimated that approximately 3 million tons of ash originating from the coal-burning process are produced annually in Brazil (KNIES et al., 2019). The thermoelectric power plants in Ceará are responsible for a monthly production of 13.5 thousand tons of ash, of this total 87% is composed of fly ash, of which 40% is sold and 60% is stored (ALCANTARA, 2018).

The materials widely used as alkaline activators are sodium hydroxide - NaOH, potassium hydroxide - KOH, sodium silicate - Na_2SiO_3 and potassium silicate - K_2SiO_3, among these, the cheapest and most used activators are sodium-based (ZHANG et al., 2020). Xie et al. (2020) reported 167 studies among pastes to alkali-activated concretes between 2000 and 2019, conducted with the activators NaOH and Na_2SiO_3. Sodium hydroxide is the main activator, acting as a catalyst for reactions as well as providing OH^- ions, while sodium silicate provides soluble silica participating as the structure-forming element (XIE et al., 2020). In the present study, NaOH and Na_2SiO_3 were used as activators.

Some challenges need to be overcome for the commercial application of AAB concretes. One of them is associated with the characterization and rheological optimization of the material. This is necessary since AABs present higher viscosity than Portland cement binders (ALNAHHAL; KIM; HAJIMOHAMMADI, 2021), which may difficult its field application. Another relevant factor is the production of materials that satisfy mechanical performance and durability requirements. Factors that are linked to the chemical composition of the precursors and activators used, the type of aggregate and the curing process (PROVIS; VAN DEVENTER, 2013; THOMAS; PEETHAMPARAN, 2017, LEE et al., 2019; ALDAWSARI et al., 2022). Although AAB concrete design methodologies exist, there is still no consolidated methodology for their production with adequate consistency, strength, and durability (XIE et al., 2020). Configuring the issues as research gaps.

Based on the motivations summarized in Figure 1.1, this study focuses on the rheological, mechanical, and durability evaluation of pastes and concretes, with low carbon emission produced, using alkali-activated binders. Besides the proposition of a mix design methodology. The AABs used in this work were synthesized from precursors composed of fly ash and steel slag obtained in the process known as Basic Oxygen Furnace (BOF), while the alkaline activators were composed of a mixture of different proportions between sodium hydroxide and sodium silicate. To produce AAB concretes, natural aggregates and steel slag aggregates were used. At the end of the study, it is expected to produce technically feasible AAB and concretes, to support future industrial waste management actions.

Figure 1.1 - Research motivations

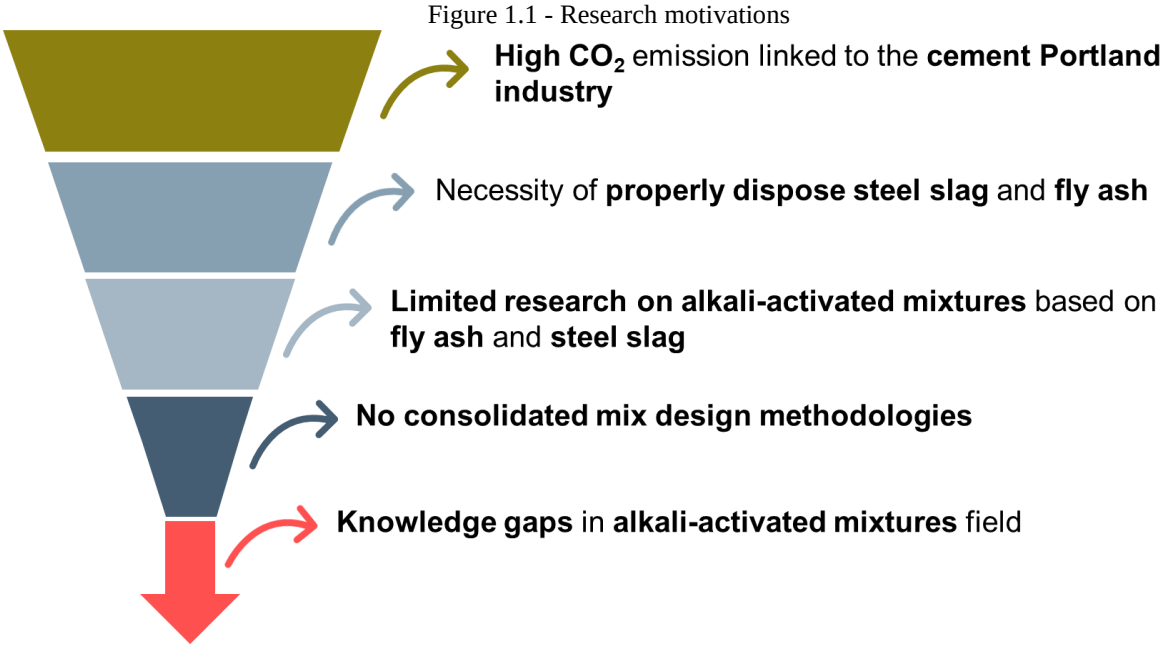

Source: elaborated by the author

1.1 Research objectives

1.1.1 Main Objective

It is expected to produce significant scientific contributions regarding the comprehension of AAB pastes and concretes produced with these non-hydraulic binders. Thus, the main objective of this research is to evaluate rheologically, mechanically, and microstructurally alkali-activated binders (AABs) based on steel slag and fly ash. In addition, it intends to evaluate the influence of the replacement of natural aggregates by steel slag aggregates as well as the curing process on the properties of AAB concretes. Besides, it proposes an effective methodology for the mix design of alkali-activated pastes and concretes.

1.1.2 Specific Objectives

To achieve the general objective, the specific objectives addressed in this research are presented below. They are organized in such a way that they fit in different Chapters in this MSc work covering some of them.

Specific objectives for Chapter 3:

- To evaluate the influence of design parameters, such as alkali content, silica modulus, precursor ratios, as well as the curing process, on the mechanical properties of AAB pastes based on fly ash and steel slag;
- To propose an efficient mix design methodology for low-carbon AAB mixtures.

Specific objectives for Chapter 4:

- To evaluate the effect of different formulations of AAB pastes and concretes on their rheological classification;
- To evaluate the effect of the mixing procedure on the rheological classification and performance of AAB self-compacting concretes.

Specific objectives for Chapter 5:

- To evaluate the influence of different aggregate types (including recycled steel slag aggregates) on the mechanical properties of AAB concretes;
- To evaluate the accuracy of dynamic non-destructive test methodologies for determining Young's modulus of AAB concretes;
- To evaluate the durability indicators of AAB concretes based on conventional methodologies and to investigate if they are adequate for such types of special concretes.

1.2 Manuscript structure

This study is divided into 6 Chapters. Chapter 1 presents reflections on the problem context, research purpose, and relevance. Chapter 2 presents a general literature review on alkali-activated binders and characterization strategies, while more specific aspects related to each of the objectives are left for Chapters 3, 4 and 5. Then, Chapters 3, 4 e 5 are presented in academic format papers to facilitate the organization and publication process after the end of this MSc work. Their content is briefly described below. Chapter 3 is already submitted to the Construction and Building Materials Journal.

Chapter 3 focused on the development and application of an alkali-activated pastes' and concretes' mix design. 36 alkali-activated binder formulations were evaluated by compressive strength, with a target compressive strength of 60 MPa under thermal curing. They were composed by the combination of parameters as: silica modulus (S/N) of the activator of 0.75, 1.25 and 1.75, alkali dosage (N%) of 6%, 8% and 10%, proportions of FA to SS from 50% to 50% and 75% to 25%, and room and thermal curing (65 ^{o}C). In this step, it was evaluated how the design parameters influence the strength values of the material. The main contribution of Chapter 3 is the production of an effective and simplified mix design, as well as the valorization of steel slag as a precursor to producing AAB.

Chapter 4 focused on the multipoint rheological characterization of the best pastes and concrete from Chapter 3. Characterization was performed using flow tests and oscillatory tests, either with a bench dynamic shear rheometer for pastes or with a planetary rheometer for

concretes. This step of the MSc work aimed to determine the material's apparent viscosity, yield stress, mixing energy and the rheological model that best describes rheological behavior in the fresh state. Besides, this Chapter evaluated the influence of the mixer type on the fresh and hardened state properties. The rheological characterization allowed the evaluation of this material application to replace more consolidated binders such as Portland cement pastes. The main contribution of this Chapter is the determination of the rheological model that best describes the behavior of AAB pastes and concretes and the discussion of the mixer method's impact on the rheological and mechanical performance of AAB concretes. The results provided information to better understand the behavior of this material and to support future applications, particularly with respect to rheology.

Chapter 5 analyzed the effect of replacing conventional aggregates by steel slag aggregates on the fresh state properties and on the hardened state properties, besides the characterization of the concretes regarding durability. For the mechanical analyses, static and dynamic Young's modulus tests and simple compressive strength tests were performed. For the durability analysis, electrical resistivity, resistance to chloride ion penetration and water penetration under pressure were performed. For the fresh state analyses, slump flow, T50 and J-ring tests were performed. The main contribution of this Chapter is the evaluation of the impact of replacing conventional aggregates by steel slag aggregates on the rheological and mechanical properties of the AAB concretes. In addition, the discussion about the accuracy of the current methodologies to assess the durability of AAB concretes.

The research ends with a list of major conclusions, challenges, limitations, improvements, and proposed future directions, described in Chapter 6. It is expected that this work helps to understand the rheological and durability performance of alkali-activated binders, which are extremely important for the future of civil construction, as well as to contribute to future design methods for these kinds of materials.

2 LITERATURE REVIEW

2.1 Alkali-activated binders

The first patents for alkali-activated concretes (AAC) date back to 1908 (KUEHL, 1908). In the last two decades, its commercial application in rigid pavements, structural parts of buildings, cast in place or precast concretes among other applications has already begun in European countries such as the Netherlands, Czech Republic, England, and it is increasingly becoming more relevant, especially with the combined use of precursors such as blast furnace slag and fly ash (PROVIS; BERNAL, 2014). As an example, there is the runway of the Brisbane West Wellcamp Airport and the construction of pavements with alkali-activated concrete, both in Australia, presented in Figure 2.1.

Figure 2.1 - Field application of alkali-activated concretes

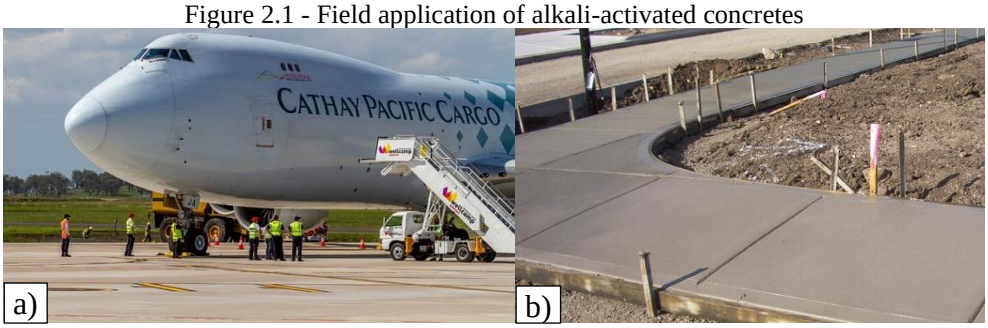

Source: a) Geopolymer institute (2015); b) Zeobond group (2022)

Alkali-activated binders are obtained by mixing two components, which are an alkaline activator (e.g. sodium hydroxide and sodium silicate) and a precursor (e.g. fly ash, slag, silica fume), the second one is the source of aluminosilicates, usually amorphous (PROVIS, 2014). They perform as a potential replacement for Portland cement as a binder in concretes (SINGH; MIDDENDORF, 2019), as well as presenting the ability to give direction to industrial coproducts through their use as a precursor (LI et al., 2018; SINGH; MIDDENDORF, 2019).

To understand the historical evolution of the alkali-activated aluminosilicate theme, Figure 2.2 was created, which lists the first studies developed, the most relevant events and the most recent advances.

Figure 2.2 - Timeline of alkali-activated binders development

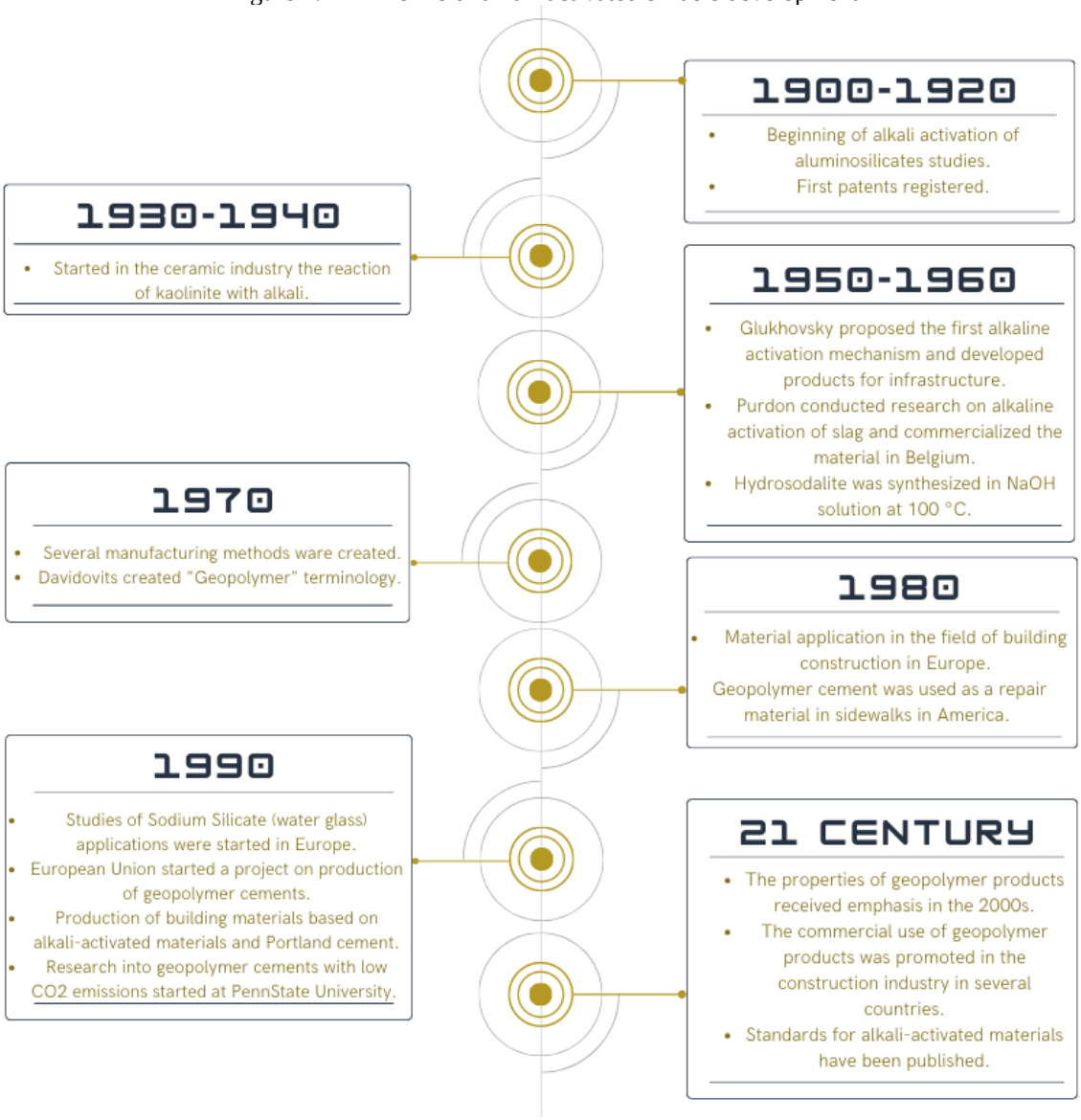

Source: adapted by Provis e Bernal (2014) and Zhang et al. (2020).

There is no unanimity of nomenclatures to designate the AAB in the literature. Thus, the same product receives different names, such as geopolymer, geocement, hydroceramics, mineral polymer and inorganic polymer (PROVIS; VAN DEVENTER, 2013), which difficult the comprehension and research on the subject. The creation of the term "geopolymer" occurred in 1978, by Joseph Davidovits, to define a new material obtained through polymerization containing structures similar to zeolites, crystalline aluminosilicates of high organizational level, presented in rocks (DAVIDOVITS, 2008). However, different products are formed during the alkaline activation of an aluminosilicate source, and the presence of calcium in the precursors is one of the main parameters which affect the products formed. When the presence of calcium is higher, such as steel slags, it leads to a formation of amorphous to semi-crystalline structures composed of C-A-S-H type gels, which can be similar

to tobermorite, depending on the gel organization form. When the presence of calcium is low, such as in silica fume and fly ash, amorphous to semi-crystalline structures tend to form N-A-S-H gel type, which can be similar to zeolites, based on the gel organization structure (PROVIS; VAN DEVENTER, 2013), as illustrated in Figure 2.3.

Figure 2.3 - Main products of alkaline activation

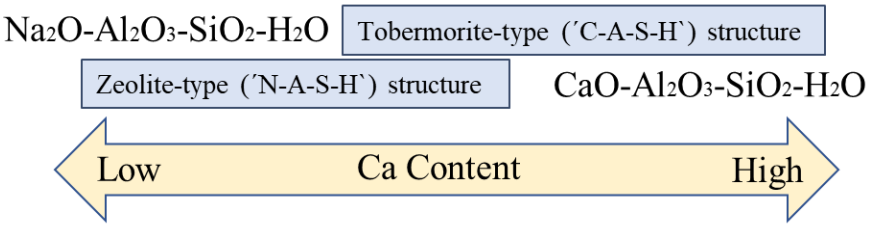

Source: adapted by Provis and Van Deventer (2019)

For some authors, such as Davidovits (2008), all products obtained from alkaline-activated precursors can be classified as geopolymers, regardless of whether the N-A-S-H type gels are not mainly formed. Nevertheless, in the present study, such nomenclature will only be assigned to materials obtained from precursors with low calcium content and that form mostly N-A-S-H gels, as identified in red in Figure 2.4, a view consistent with authors such as Provis and Van Deventer (2013). For precursors that do not agree with this criterion, the term alkali-activated binder (AAB) will be used, the majority class that incorporates all products obtained by the alkali-activation process (MARVILA; AZEVEDO; VIEIRA, 2021).

Figure 2.4 - Potential products of alkaline activation

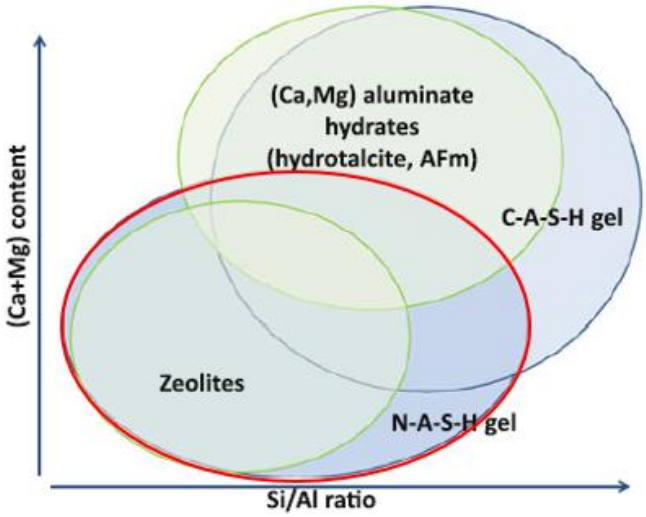

Source: adapted by Provis and Van Deventer (2014)

Thus, for the present study, the term alkali-activated binder will be adopted to define the material obtained by the combined activation of the precursors fly ash and steel slag instead of the term geopolymer, because this term, although more widespread and recognized, does not apply to the mixture of precursors used, due to its calcium content (PROVIS; VAN

DEVENTER, 2013). AAB has the potential to replace the binder known as Portland cement for concrete production. Complementarily, AAB concrete is the concrete produced from the union of aggregates using the AAB. It is not uncommon in literature to use the term "geopolymer concrete" for these materials (DAVIDOVITS, 1994; NATH; SARKER 2014; DING; SHI; LI, 2018).

To understand the products formed during the alkaline activation mentioned above, it is important to understand the N-A-S-H and C-A-S-H formation processes. In this process, there is the dissolution of the precursors (Al_2O_3, SiO_2 and CaO), their interaction with the activators (Na_2SiO_3 and NaOH), reorganization, nucleation, formation of the gels ($CaO\text{-}Al_2O_3\text{-}SiO_2\text{-}H_2O$ (C-A-S-H) and $Na_2O\text{-}Al_2O3\text{-}SiO_2\text{-}H_2O$ (N-A-S-H)), polymerization and setting (PROVIS; BERNAL, 2014; SINGH; SINGH, 2019). The entire process is illustrated in Figure 2.5. It is important to highlight that the gels formed in alkaline activation are conditioned to a range of factors such as: the chemical composition of the activators and precursors; the thermal regime of curing; the amount of free water; the specific surface of the precursors; and the presence of calcium and magnesium in the precursors (PROVIS; VAN DEVENTER, 2013).

Figure 2.5 - Alkali-activation process

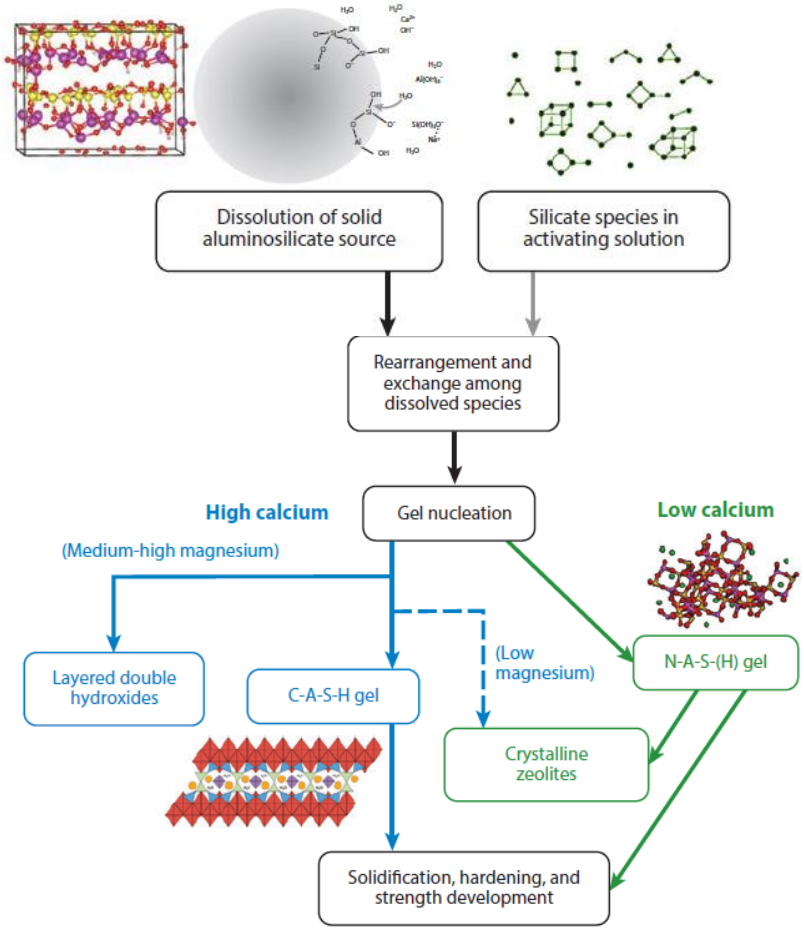

Source: Provis and Bernal (2014)

The formation of C-A-S-H gel types usually occurs with high Ca/(Si + Al) ratios, usually greater than 1, presented in precursors such as slags (PROVIS; VAN DEVENTER, 2019). Similar to Portland cement, gels can present a tobermorite-like structure formed by crosslinked and uncrosslinked bonds (MYERS et al., 2013). These structures are formed by outer layers of CaO, tetrahedral interlayers coordinated by chains of three silicates with two paired and one bonded side (dreierketten-type structures), the region between layers, which is formed by alkali, Ca^{+} cations, and chemically incorporated water (PROVIS; BERNAL, 2014), as illustrated in Figure 2.6. The presence of Aluminum (Al), illustrated in red, is restricted by the chemical structure of the tobermorite and it is usually present in the binding sites of the tetrahedral structures and in the interlayer regions, as Al^{+3} (MYERS et al., 2013; PROVIS; BERNAL, 2014).

Figure 2.6 - Structure of C-A-S-H gels

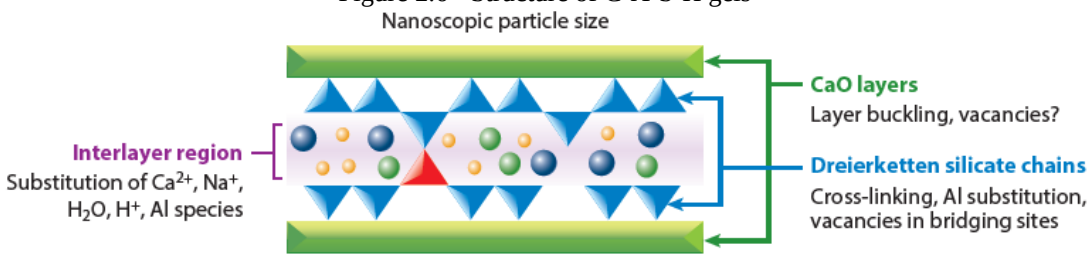

Source: Provis and Bernal (2014)

The N-A-S-H gel types are obtained by alkaline activation of precursors such as fly ash and silica fume. These gels exhibit a cross-linked nature (PROVIS, 2014). N-A-S-H is formed by tetrahedral chains of SiO_4 and AlO_4, linked by sharing one oxygen. In these chains, the charges are balanced by Na^{+} ions (EL HAFID; HAJJAJI; EL HAFID, 2017) coordinated through oxygen atoms and water molecules. In these structures, the components (Si, Al, O, Na, H) are presented in different proportions (WALKLEY et al., 2018). A schematic model of N-A-S-H gels is presented in Figure 2.7.

Figure 2.7 - Structure of N-A-S-H gels

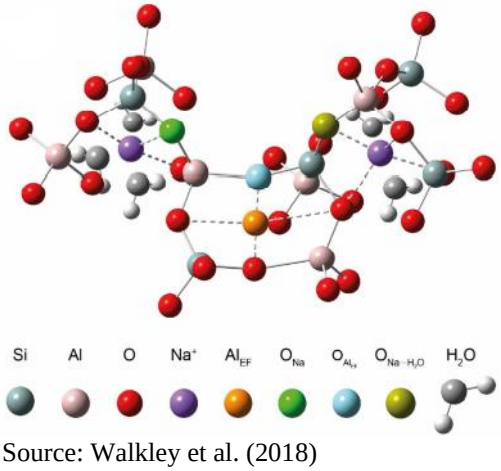

Source: Walkley et al. (2018)

2.2 Formulation of alkali-activated binders

The combined use of precursors with different calcium contents, such as slag and ash, aims the coexistence of different gels, mainly N-A-S-H and C-A-S-H gels (ISMAIL, et al., 2014). AABs obtained from mixed precursors show good resistance to chemical attack compared to Portland cement-based pastes (SHI, 2003; ZHANG et al., 2017) and good mechanical performance at high temperatures (BERNAL et al., 2013; ZHANG et al., 2020), a property linked to N-A-S-H gels. Besides, AABs can show lower porosity as the contents of C-A-S-H gels increase (BERNAL et al., 2014).

The coexistence of gels that provide good mechanical and rheological properties is not so simple to achieve, since the kinetics of the reactions processed during alkaline activation is very complex (PROVIS; VAN DEVENTER, 2019). If calcium is released quickly without sufficient silica present, it can quickly precipitate as portlandite (calcium hydroxide crystal), interfering negatively with the formation of the C-A-S-H type gels (WALKLEY et al., 2016), which causes efflorescence. Moreover, if the calcium-rich precursors consume a large amount of alkali from the activators, part of the aluminosilicates of lower reactivity, present in precursors with lower calcium content, may remain unreacted or partially reacted, impacting negatively the hardening process and strength gain of the mixture (WALKLEY et al., 2016).

Another important item in AAB is the curing process. High temperatures accelerate the setting and hardening of alkali-activated binders, combined with other factors, such as solution alkalinity and water/binder ratio, which influence the phases formed during alkaline activation (PROVIS, 2014; PROVIS; VAN DEVENTER, 2019). Previous research has found strength gains, especially at early ages, for AAB under thermal curing for 24 hours at temperatures between 60 °C and 70 °C for binary blends of blast furnace slag and fly ash (YUSUF et al., 2014; SOUTSOS et al., 2015, COSTA, 2022). Therefore, it will be adopted as thermal curing the temperature of 65 °C and as ambient curing the temperature between 25 °C and 30 °C (NCEI, 2022), average temperatures in the city of Fortaleza.

The formulation of alkali-activated binders is also important. There are different mix design approaches to determine the activators and precursors proportions. Some approaches are based on the amounts of activator and precursor solution masses. Others attempt to dose activators and precursors based on their chemical composition (relating the proportions of SiO_2 and Na_2O contained in activators). The main literature approaches will be briefly described below.

To establish the proportions between the activators there are two main different dosing approaches. The first is to use the mass ratio between the solutions, as the masses of sodium silicate and sodium hydroxide (COSTA, 2022). The second is to use the indicator called Silica Modulus (S/N) of the activator. For activators based on sodium silicate and sodium hydroxide, its design is composed of the mass ratio between SiO_2/Na_2O of the chemical components of the activators, as illustrated in Figure 2.8. SiO_2 derives from sodium silicate and Na_2O comes from both sodium silicate and sodium hydroxide (LEE; LEE, 2013; XIE et al., 2020). In this case, sodium hydroxide is used to change the silica modulus of sodium silicate (RAFEET et al., 2017). For other activators, such as potassium based, the terms of the equation changed.

To delimit the ratio between activators and precursors, there are two main approaches: the alkali content (usually abbreviated by M+, N/B or N%), represented by the mass ratio between the amount of Na_2O, and precursors (SOUTSOS et al., 2015; LI et al., 2018), as illustrated in Figure 2.8; or else the use of the direct ratio between the amount of activator and precursor, by mass (THOMAS; PEETHAMPARAN, 2017).

Figure 2.8 - Mix design methodologies of alkali-activated binders

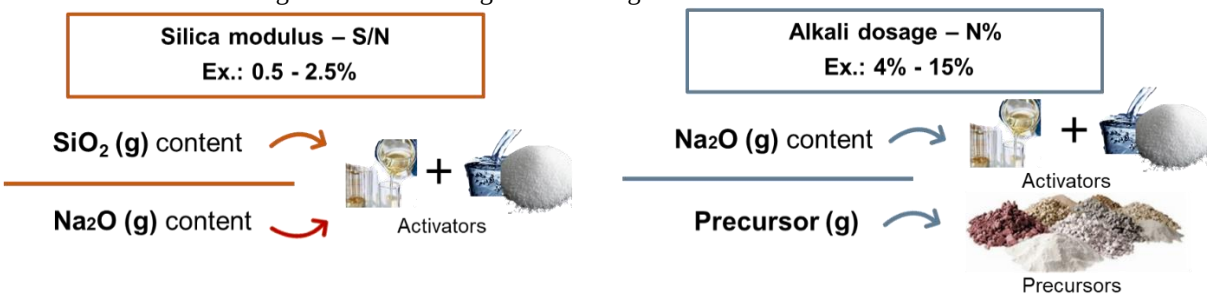

Source: elaborated by the author

In this study, the silica modulus (S/N) and alkali content (N%), were used to formulate the proportions of activators and precursors. The literature reports studies using S/N between 0.5 and 2.5 (SOUTSOS et al., 2015; THOMAS; PEETHAMPARAN, 2017; DING; SHI; HI, 2018) and concentrated N% between 4% and 15% (SOUTSOS et al., 2015; LI et al., 2018) for blends based on fly ash and blast furnace slag activated with NaOH (sodium hydroxide) and Na_2SiO_3 (sodium silicate).

Compared to conventional concretes, the AAB concretes does not present consolidated design methodologies, being common in the literature recent studies that develop design methodologies such as Junaid et al. (2015), Pavithra et al. (2016) and Xie et al. (2020). This is mainly due to the large number of factors involved in mix design, such as the different physical and chemical properties of activators and precursors, the complex interaction between

paste, the need to determine the amount of free water in the mixture, and finally the proportions of aggregates. Among the design methodologies for AAB concretes, fixing the paste content is one of the most applied methodologies. Thus, the paste content is chosen according to the voids to be filled between the aggregates, considering the desired strength or workability parameters, being common values of paste content higher than 10% of the voids content (GOMES; BARROS, 2009; RAFEET et al., 2017; LI et al., 2018; LI et al., 2019).

Figure 2.9 illustrates some differences in volumetric composition between alkali-activated and conventional concrete. In AAB concrete, the additional water is mainly used to make the mixture workable, while the strength is ensured by the interaction between the activator and the precursor, whereas for conventional concrete the strength is obtained by the hydration of Portland cement (LI et al., 2019). The water used to give workability to the mixtures, often added together with alkaline activators, has a negative effect on the mechanical properties of AAB concrete, producing an increase in the porosity of the hardened concrete and interfering in the interaction between precursors and activators (LI et al., 2019; XIE et al., 2020; ZHANG et al., 2020).

Figure 2.9 - Conventional concrete × Alkali-activated concrete

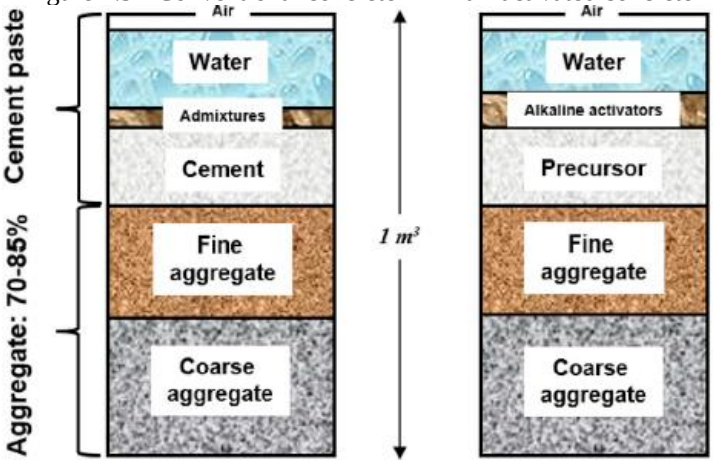

Source: Li et al. (2019)

2.3 Precursors and aggregates

AABs are produced from industrial by-products such as metakaolin, fly ash and slag, or by-products of agricultural origins, such as rice husk ash and sugar cane ash (AZEVEDO; STRECKER, 2017; ELAHI et al., 2020). The properties of AABs are closely linked to the type of precursor used and its characteristics, such as its chemical composition, the size of its particles, and the content of aluminosilicates and the calcium content (SOUTSOS et al., 2015; ZHANG et al., 2018, XIE et al., 2020).

As the present study focused on precursors consisting of a binary mixture of fly ash and steel slag, these will be discussed. The combined use of the precursors mentioned leads to the coexistence of N-A-S-H and C-A-S-H gels. Figure 2.10 presents a ternary diagram containing examples of the combined use of slag and fly ash, explaining details of the composition in terms of the relative amounts of CaO, Al_2O_3 and SiO_2 and detailing the type of gel that tends to be formed as a function of composition. The green and yellow points in Figure 2.10 represent the use of the two precursors in different proportions (according to the legend), while the white and blue points represent the precursors in isolation. As can be seen, the use of associated precursors most commonly generates the coexistence of C-(N)-A-S-H gels, which is desirable, as already presented.

Figure 2.10 - Ternary diagram of different alkali-activated binders' compositions

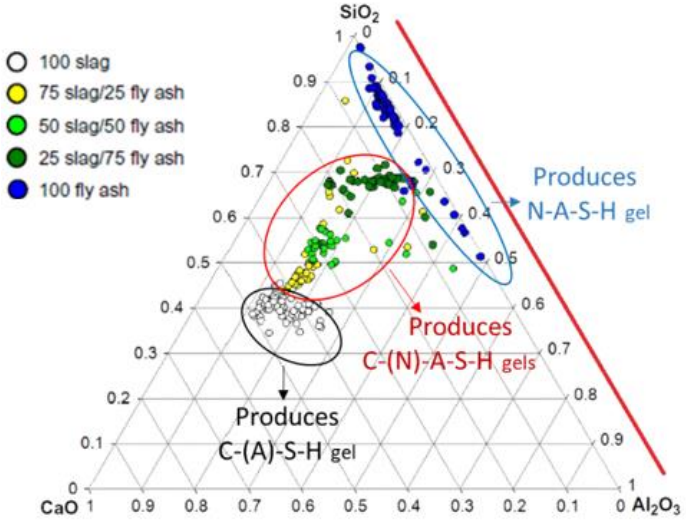

Source: adapted by Provis and Van Deventer (2019)

2.3.1 Fly ash

According to the American Society for Testing Materials (ASTM) C618 (2019), fly ash is an industrial byproduct obtained from burning charcoal or mineral coal, which belongs mainly to two classes, class "C" and class "F", depending on the amount of CaO present in its composition. If this value is less than 18% of the mass of its composition, it is classified in class "F", and if the value is higher than 18%, it is classified in class "C". Fly ash, especially class "F", is a great source of aluminosilicates, besides having a competitive price and the presence of reactive amorphous phases (ELAHI et al., 2020). It is also mentioned that fly ash can present a pozzolanic character according to NBR 12,653 (2015) and NBR 5,751 (2015). This means that, in the presence of hydrated lime, fly ash can produce hydration products similar to those of Portland cement hardening (hydrated calcium silicate, CSH) (MEHTA; MONTEIRO, 2013).

Therefore, fly ash already finds use in construction, but there is still a necessity to develop applications to promote the utilization of these materials, such as geopolymers (JUNAID et al., 2015; PAVITHRA et al., 2016).

Fly ash is composed of spherical particles usually extremely fine (less than 150 µm and with an average diameter of around 25 µm), composed mainly of alumina (Al_2O_3), silica (SiO_2), iron oxide (Fe_2O_3) and, in smaller quantities, calcium oxide (CaO) and magnesium oxide (MgO) (SOUTSOS et al., 2015; ROHDE; MACHADO, 2016). They come from burning coal in thermoelectric power plants and are obtained from the outlet of combustion gases through electrostatic precipitators, fabric filters and other systems (BARROS, 2015; ROHDE; MACHADO, 2016), a process represented in Figure 2.11. Their characteristics will depend on the chemical composition of the coal used. The Brazilian matrix is composed of 76.55% sub-bituminous coal and lignite and 23.45% bituminous coal and anthracite (BRITISH PETROLEUM, 2018). Sub-bituminous coals tend to generate ashes falling into class "C", while bituminous coals and anthracite tend to generate fly ash belonging to class "F" (BARROS, 2015).

Figure 2.11 - Fly Ash obtaining process

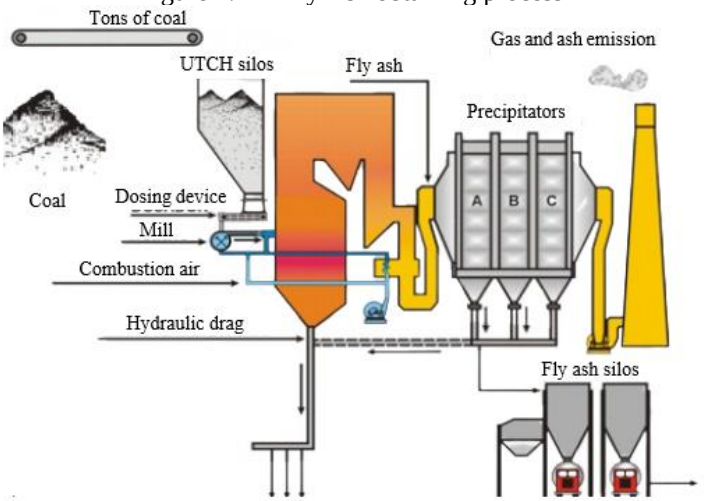

Source: adapted by Rohde (2016)

The by-products generated during the production of electric energy in thermoelectric power plants are not limited to fly ash, which represents 70% to 90% of the production. Besides them, it can mention the heavy ash (bottom ash) from 10% to 20% and, in smaller quantities, ash from the desulfurization process (spray dryer ash) (ALCANTARA, 2018; VIEIRA, 2020). In Brazil, the annual production of coal ash is about 3 million tons (KNIESS et al., 2019). In the state of Ceará, the plants of the Pecém thermoelectric complex have an average daily production of about 900 tons of coal ash, which represents approximately 0.328 million tons/year, and of this production, 60% are usually stored in an internal yard and

40% are commercialized (ALCANTARA, 2018). Its structure and storage tanks are illustrated in Figure 2.12.

Figure 2.12 - Thermoelectric Complex Production of Pecém

Source: adapted by Eneva (2021) and Google Earth images (2022)

2.3.2 Steel slag

Steel slag is a by-product of the steel industry, obtained from the transformation of pig iron and scrap into steel (NAIDU; SHERIDAN; VAN DYK, 2020; NUNES; BORGES, 2021). Its main chemical components are the following oxides: CaO, SiO_2, Al_2O_3, Fe_2O_3, FeO, MgO, and MnO. The values of the contents of each component change according to the type of furnace and production process (YI et al., 2012). Steel slag has applications in soil stabilization (MANSO et al., 2012), aggregates in concrete (ABU-EISHAH; EL-DIEB; BEDIR, 2012, CRISTELO et al., 2019) and asphalt mixtures (CHEN et al., 2015; LIU et al., 2020), water treatment (BOVE et al., 2018) and as supplementary material to Portland cement (JUANG et al., 2018).

Steel slag is a co-product of low added value compared to other slags due to its low amount of amorphous silica and significant iron oxide content compared to other slags such as blast furnace slag, which already has wide application, including in the cement industry (METWALLY; FARIED; TAWFIK, 2017; NUNES; BORGES, 2021). However, its application in AABs is pointed out as a possible solution for use on an industrial scale. However, studies with this type of slag are still emerging, and most of the research is concentrated around AABs using blast furnace slag (NUNES; BORGES, 2021).

The transformation of pig iron and steel scraps into steel differs from industry to industry. There are two main transformation systems: one that employs an oxygen converter furnace, known as Basic Oxygen Furnace (BOF), also known as the Linz-Donawitz process, and another system that employs electric arc furnaces, known as Electric Arc Furnace (NUNES; BORGES, 2021). Both are represented in Figure 2.13. The small amount of research involving

the activation of this type of precursor does not always cite the origin of the type of steel slag, referring only as steel slag, as can be observed, for example, in Dhoble and Ahmed (2018) and Guo and Pan (2018).

Figure 2.13 - Production process for steel slag

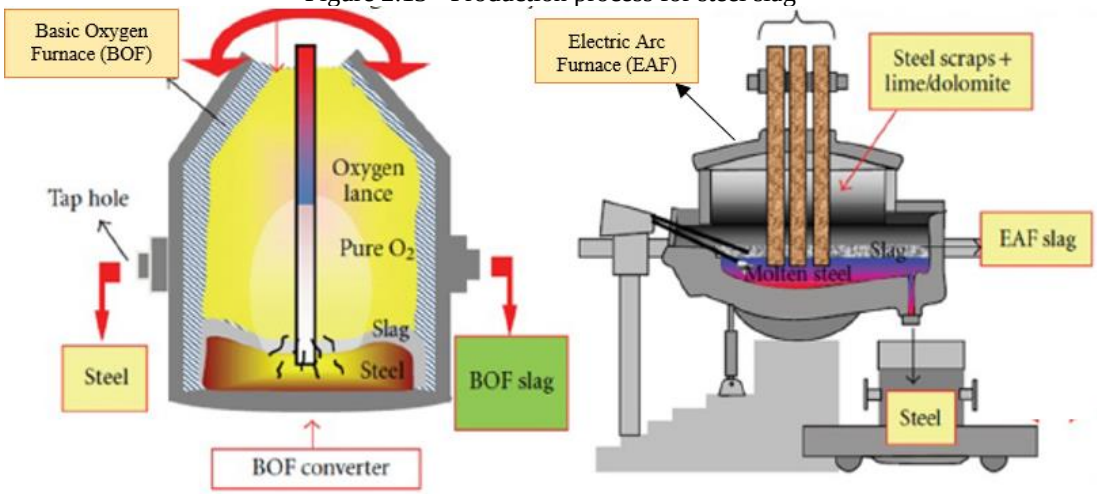

Source: adapted by Nunes and Borges (2021)

In 2020, world steel production was 1,877.3 million tons (BSI, 2021). In this scenario, Brazil is the 9th largest producer with 31.4 million tons (BSI, 2021). Among the Brazilian production, Ceará represented about 9.1%, with 2.86 million tons (BSI, 2021). Of the total amount of steel produced annually in Brazil, 74.5% was obtained using the BOF system, with 23.4 million tons (BSI, 2021). It is estimated that for each ton of steel produced, about 607 kg of waste and coproducts are generated, and of this total the production of steel slag represents about 27% (BSI, 2018), or about nearly 165 kg. Other research indicates that for each ton of steel produced, between 100 kg and 150 kg of steel slag is produced (WIMMER et al., 2014; HORII et al., 2015), a value lower than that indicated in the BSI (2018) research. Regardless of the reference adopted, the large-scale destination of steel slag is an environmental and business challenge given its low utilization rate (only about 36%) in the face of the large production volume (NAIDU; SHERIDAN; VAN DYK; 2020; NUNES; BORGES, 2021).

The Siderurgical Company of Pecém (CSP), located in the state of Ceará, was the place of supply of the slag used in this research. This company (Figure 2.14) produces a range of slags, their nomenclatures, and chemical characteristics depend on which part of the production line they were obtained and which method for cooling was used. The first slag produced during steel production is the granular blast furnace slag, during the transformation of iron ore into pig iron, and if this slag does not go through the granulation process, it is called dry pit (AMANCIO, 2019). Next, the melt furnace process is started. On it, the pig iron

produced in the blast furnace goes through a pre-treatment of desulfurization to reduce the sulfur content and other impurities. From this process, the first slag of the melt shop processes is produced, called Kambara Reactor (KR) slag (AMANCIO, 2019). Next, the primary refining of pig iron occurs, in which, in furnaces via oxygen converter, pig iron is transformed into steel, a process that also produces the second and third types of steel slag, called BOF and Baosteel's Slag Short Flow (BSSF), which differ just by the cooling process of the material. BSSF slags undergo a granulation process using water, while BOF slags are cooled slowly at room temperature (BSI, 2018; AMANCIO, 2019). The last slag produced is the so-called "pan" slag, a slag that results from the secondary refining of the steel (AMANCIO, 2019).

Figure 2.14 - Siderurgical Complex of Pecém

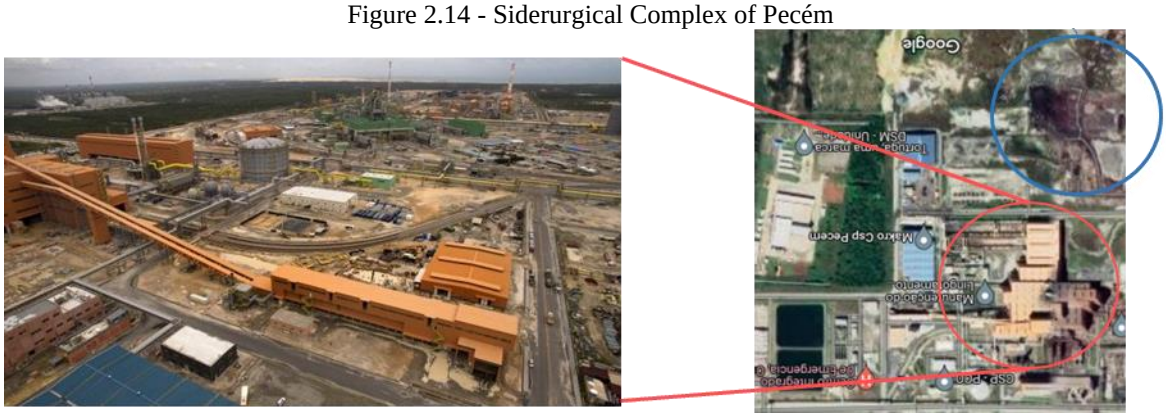

Source: adapted by Companhia Siderúrgica do Pecém (2021) and Google Earth images (2022)

In this study, the steel slag used as a precursor is from the BOF process, obtained from the primary refining and given the same name as the BOF process, without the granulation process. This slag tends to be more crystalline due to its slow cooling. As an aggregate, steel slags BSSF type were used, which presents a more amorphous structure and with lower calcium oxide content, which reduces its expansibility and makes the BSSF present a greater potential application as aggregate (SOUZA, 2016; AMANCIO 2019, NUNES; BORGES 2021). Throughout the text, slags will be treated only as steel slag or simply BOF SS or BSSF SS type.

The BSSF-type steel slag results from the instantaneous cooling of the material with the aid of water jets in rotating drums, a process that promotes stabilization through thermal shock (SOUZA, 2016; CAMPOS; RAFAEL; CABRAL, 2018). In addition, this water-assisted process reduces the amounts of free lime, which mitigates the expansive problems presented by aggregates of steel origin (SOUZA, 2016). This slag treatment system is pioneering, being developed by the Chinese and South Korean steel industries (BSI, 2018). The use of this type of aggregate in alkali-activated concretes can be even more potential, since this material presents silicoaluminates like those used in precursors. Thus, greater interaction between binder and aggregate and possibly a transition zone of lower brittleness may occur.

Furthermore, the use of recycled aggregates may represent a reduction in the use of natural resources since natural resources are no longer extracted from the environment. For example, in Brazil, around 519 million tons of aggregates are consumed per year according to the National Association of Aggregates Producers for Construction (NAAPC, 2016). Thus, the use of alternative aggregates compared to conventional ones in the production of alkali-activated concretes is justified. In the present research, BOF steel slag will be used as precursor while BSSF steel slag will be used as aggregate.

2.4 Alkaline activators

The alkaline activators combined with the precursors produce alkali-activated pastes. Generally, these materials are composed of hydroxides, silicates, sulfates, or carbonates (REVATHI; JEYALAKSHMI, 2021), being most used sodium (most common) and potassium hydroxides and silicates (PROVIS; VAN DEVENTER, 2013; ZHANG et al., 2020). Sodium silicates represent a relevant portion of the published studies on alkaline activation (XIE et al., 2020). Sodium hydroxide is responsible for ensuring the high alkalinity of the solution, important to catalyze alkaline activation, while sodium silicate performs as an additional source of soluble silica (XIE et al., 2020).

Sodium silicate is commercialized in solution form, produced by dissolving SiO_2 and Na_2O in H_2O, in different proportions. Sodium hydroxide, on the other hand, is marketed in flakes or micro-pearls with a certain purity degree (with values above 97%) and its concentration in solution form varies according to the scope of each research.

The proper use of activators is essential for the coexistence of C-A-S-H and N-A-S-H gels (WALKLEY et al., 2016). It is important to consider the pH of the activator solution, such that it is not high enough to cause the precipitation of calcium into portlandite, as when only sodium hydroxide solutions are used (pH ~ 14) (WALKLEY et al., 2016). Thus, it is important the use activators such as sodium silicate (pH between 11 and 13.5) only or combines with higher pH activators such as sodium hydroxide, in solution, (DONATELLO; FERNÁNDEZ-JIMENEZ; PALOMO, 2013; PROVIS; BERNAL, 2014). Research involving the variation of molarity of sodium hydroxide solution in binary mixtures of blast furnace slag and fly ash concluded that concentrations of 10 mol/L are the most suitable and showed higher strength values when different activators were combined (YUSUF et al., 2014; NAGARAJ; VENKATESH BABU, 2018).

2.5 Characterization of alkali-activated mixtures

Although some studies have studied the mechanical behavior of AABs (SOUTSOS et al., 2015; CRISTELO et al., 2019), scarce researches have attempted to relate this property to the rheological response of the material and its microstructure, especially for precursors such as steel slag, which are still understudied (XIE; KAYALI, 2016; MA et al., 2022). Understanding the microstructural properties of AABs is also important since parameters such as durability, mechanical and workability, among other properties, are closely linked to the chemical structures formed during alkaline activation (ELAHI et al., 2020; ZHANG, et al., 2020). Their microstructural and chemical characterization can be performed with the aid of techniques such as Scanning Electron Microscopy (SEM) (PROVIS; VAN DEVENTER, 2013). Considering this, AABs must go through a mechanical, microstructural, and rheological characterization process. In addition, it is necessary to understand the application of AABs in concrete and their impact on fresh state properties and mechanical properties, as well as to evaluate the durability of this new material. To better understand how AAB pastes and concretes are produced, Figure 2.15 was elaborated.

Figure 2.15 - Alkali-activated mixtures: paste to concrete

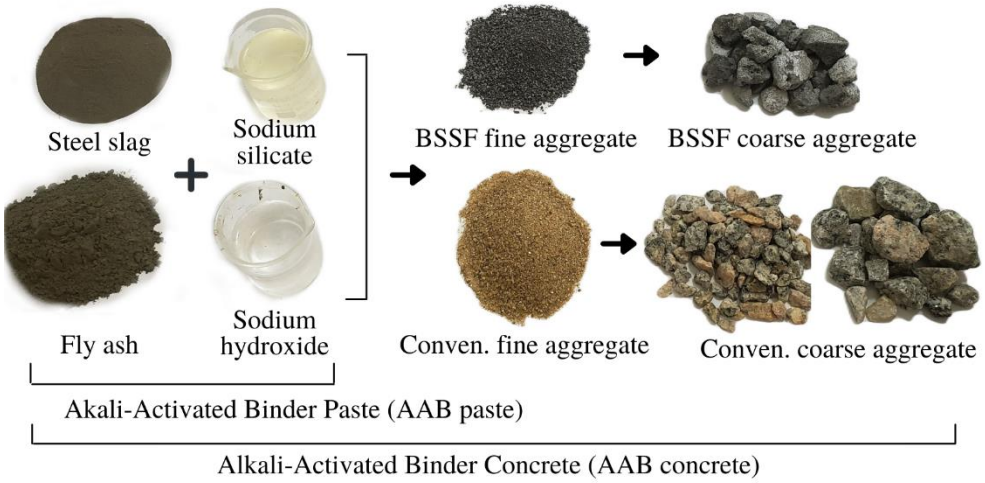

Source: elaborated by the author

2.6 Main studies on alkali-activated binders

Based on the rheological characterization of AABs, some studies focus on the determination of the apparent viscosity and yield stress and other parameters of the material. Puentas, Vargas and Alonso (2014) found that pastes based on blast furnace slag presented different rheological behaviors according to the activator used. When NaOH associated with Na_2CO_3 was used, the paste showed behavior like that presented by Portland cement-based pastes, with experimental results fitting well into a Bingham model. As for pastes activated with

Na_2SiO_3, the material required more rheological parameters and had rheological behavior represented more accurately by a Hershel-Bulkley model. Another relevant factor in the rheology of alkali-activated binders was determined by Güllü et al. (2019), who found that the rheological model of the material is affected by the type of precursor used, as their pastes behaved as dilatant, pseudoplastic or Bingham fluid, using different variations of fly ash and silica fume. Since the present research will make use of Na_2SiO_3 and NaOH as activators, and fly ash and steel slag as precursors, in different arrangements, their rheological characterization must be performed to understand the behavior of these different compositions of alkali-activated pastes.

To evaluate the mechanical performance Mehta et al. (2020) replaced 20% fly ash with blast furnace slag and obtained pastes with up to 65 MPa of compressive strength at 90 days. In addition, they observed a porosity reduction of the material as the slag was added. Thomas and Peethamparan (2017) worked with binders, changing the silica modulus of the activator in the proportions of 0.1, 1.0, 1.5 and 2. 5, with alkali content of 2%, 3%, 4%, 4.2%, 4.4%, 4.6%, 4.8%, 5%, 6% and 7% and solution/precursor ratios, for concrete, of 0.35, 0.40, 0.425, 0.45 and 0.50, and several compositions among ash and slag. They obtained compressive strength of 55 MPa for ambient curing and 75 MPa for thermal curing. Soutsos et al. (2015) studied the variation of alkali content between 3% and 15% and silica modulus between 0 (NaOH only) and 2 (Na_2SiO_3 only), achieving the best results for silica modulus between 0.67 and 0.80 and alkali content between 7.5% and 12.5%, reaching strength values up to 70 MPa. Ding, Shi, and Li (2018) in their study varied the silica modulus of the activator between 1 and 2, with alkali contents of 3% and 5%, total liquids/binder ratio between 0.40 and 0.45, and obtained the best results for alkali contents of 5% and silica modulus of 1.5, with strengths up to 65 MPa.

Studies regarding the alkaline activation of steel slag, both by the BOF process and by an electric arc, are still initial when compared to studies involving GGBSF. Guo and Pan (2018) studied alkali-activated mortars reinforced with steel and polypropylene fibers that had unspecified steel slag (30%) and fly ash (70%) as precursors coactivated with Na_2SiO_3 and solid NaOH, with alkali content of 10% and silica modulus of 1.5, obtaining compressive strengths up to 39 MPa. Song et al. (2019), on the other hand, used steel slag from the electric arc process as a substitute for fly ash in the contents of 10%, 20%, 30% 40%, and 50%. NaOH and Na_2SiO_3 were used as activators, composing a solution with a silica modulus of 1.6 and a solution/binder ratio of 0.65. As a result, these authors found that the best replacement rate was 20%, since it

combined improved workability, intermediate setting time, and maximum strength of 25 MPa, as presented in Figure 2.16. Cristelo et al. (2019) evaluated the use of steel slag from the electric arc process as precursor (25%, 50%, 75% and 100% in replacement of slag) and as aggregate, activated with NaOH (8 mol/L), obtaining as conclusions that the most appropriate content of replacement as precursor was 50%, with strength around 28 MPa and that its use as aggregate also contributes to the improvement of mechanical properties, as presented in Figure 2.16.

Costa (2022) conducted a study of AABs using BOF steel slag as the only precursor and combined with fly ash and bottom ash, activated with sodium hydroxide and sodium silicate. The pastes containing BOF steel slag as the only precursor reached compressive strengths between 1.6 MPa and 17.7 MPa, these results are related to the variation in mixing parameters, such as molars concentration of the sodium hydroxide solution and the ratio between activator solution and precursor. In the pastes composed of BOF steel slag and fly ash activated with sodium silicate and sodium hydroxide (14.2 mol/L) solution in a 1:1 ratio, compressive strength between 18.1 MPa and 62.3 MPa was obtained, illustrated in Figure 2.16. This variation is related to the BOF steel slag content, with the best result observed in the paste composed of 50% fly ash and 50% BOF steel slag.

Figure 2.16 - Relevant research regarding steel slag as a precursor in AAB

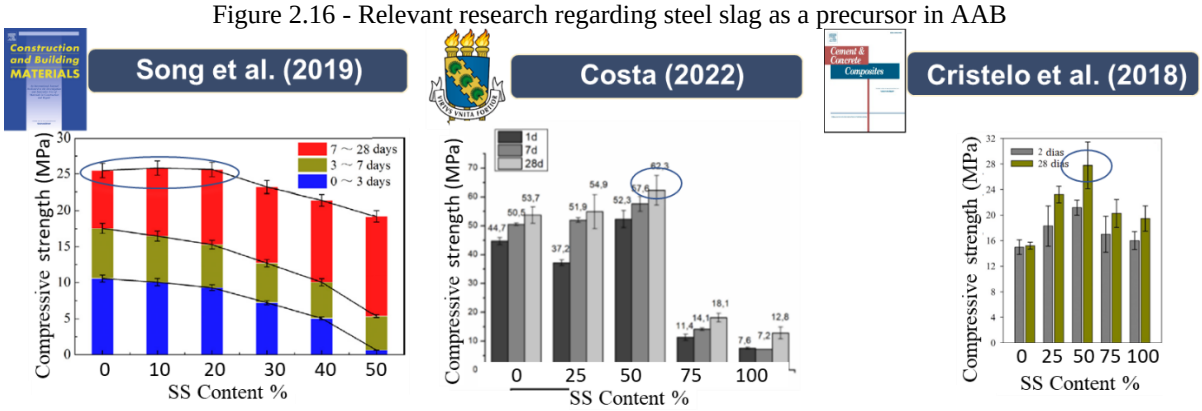

Source: adapted by Song et al. (2019); Cristelo et al. (2018); Costa (2022)

Among the microstructural evaluation, Nath and Sarker (2014) evaluated the replacement of fly ash with blast furnace slag at the contents of 10% and 50%, activated with sodium silicate to sodium hydroxide ratio of 2.5, by mass, and found that the increase of blast furnace slag content leads to the reduction of the porosity of the mixture, they also found the coexistence of the C-A-S-H and N-A-S-H gels. Yusuf et al. (2014) found similar results and conclude that the porosity reduction improved the mechanical properties with the combined use of fly ash and slag precursors.

Costa (2022), in his microstructural analyses, indicated that the incorporation of BOF slag modified the microstructure formation, since the coexistence of C-A-S-H and C-N-A-S-H gels and the densification of the cementitious matrix were observed, i.e., the absence of pores and cracks commonly observed in the N-A-S-H gel, formed in matrices containing only the low calcium fly ash.

2.7 Background of the research developed in the UFC

Several researches have been developed, at the Federal University of Ceará, using steel slag from the Pecém steel company and fly ash from the Pecém thermoelectric complex. Figure 2.17 brings a summary of the researchers found.

Silva (2018), Amancio (2019) and Dias (2019) evaluated the potential application of the material as aggregate. Freitas (2019) studied the synthesis of zeolites and other composites from fly ash. Caetano (2021), Costa (2022), Targino et al. (2022), Guimarães (2022) and Moreira (2022) studied binary mixes of slag and ash for AAB pastes or concretes production.

It is noteworthy that the present research had as its main motivation the studies developed by Costa (2022), detailed previously, and motivated the studies of Guimarães (2022), and Moreira (2022). Other studies were also conducted in the UFC but were not attached to not make the review too extensive.

Figure 2.17 - Background of UFC's research conducted in this area

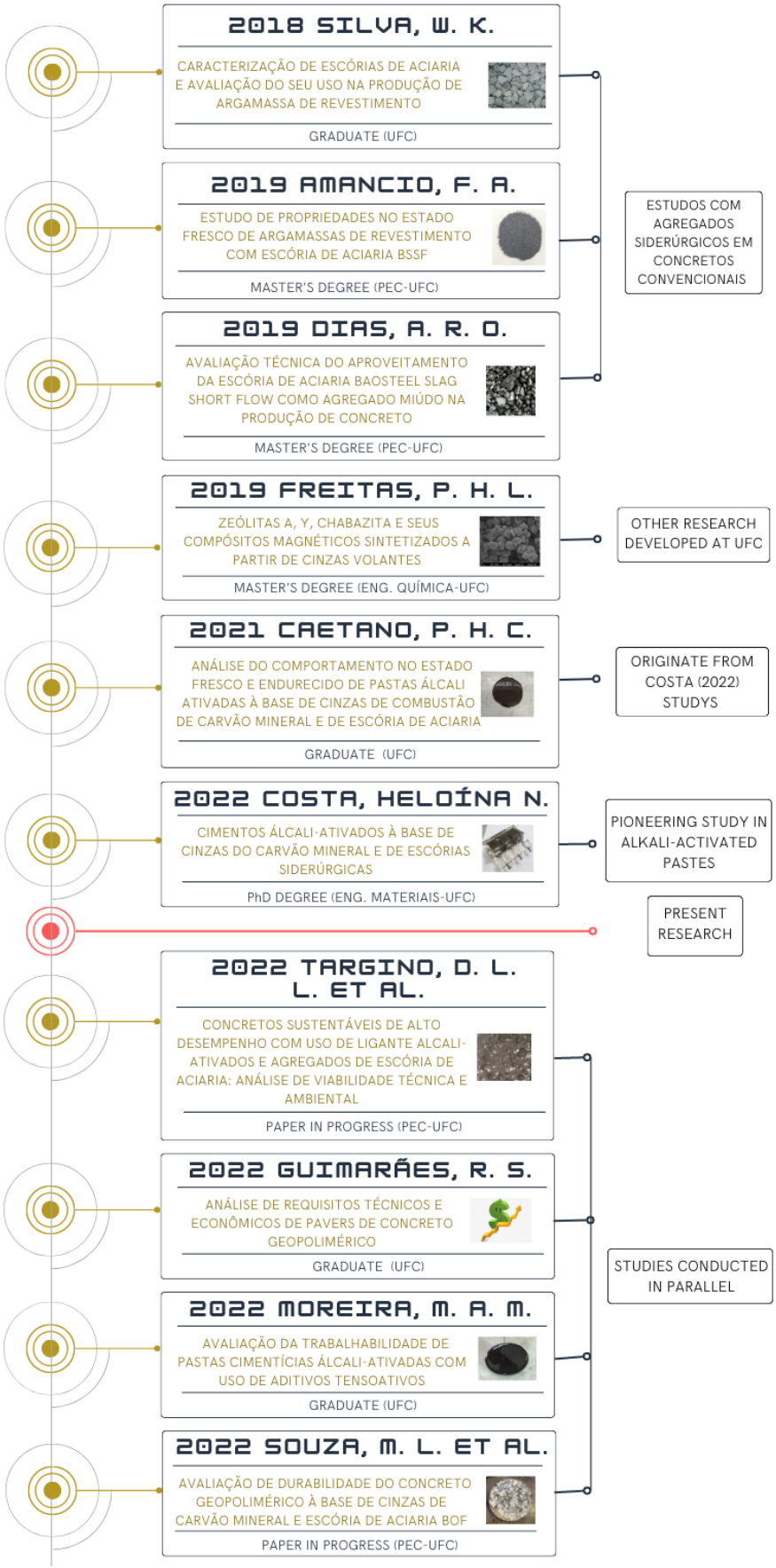

Source: elaborated by the author

3 DESIGN AND EVALUATION OF ALKALI-ACTIVATED PASTES AND CONCRETES PRODUCED WITH FLY ASH AND STEEL SLAG

Abstract

This study aims to propose a design procedure to formulate and mechanically evaluate alkali-activated binder (AAB) pastes and concrete, also known as geopolymers. The investigated binder was based on thermoelectric powerplant coal fly ash and steel slag (Basic Oxygen Furnace type) activated with sodium silicate and sodium hydroxide solutions. The binder design procedure begins with sweeping different compositional parameters (alkali content from 6% to 10%, silica modulus from 0.75 to 1.75, and ash-slag ratios of 75%-25% and 50%-50%) of an AAB paste binary composition, then composing a mechanical resistance parameter heatmap (in this paper compressive strength of the hardened paste). The influence of the curing process was also investigated, with either ambient (25 °C) or thermal (65 °C) conditions. Consistency (evaluated with mini-slump tests and setting time) is also considered to choose amongst the best AAB paste candidates for concrete. Results suggest that lowering silica modulus amongst the tested range improves the mechanical performance of the AAB pastes, with the compressive strength of concrete, reaching values up to 80.1 MPa. The manufacturing procedure starts with sweeping different proportions for coarse (crushed granitic) and fine (river sand) aggregates (0%-45% of

substitution, by mass), aiming for the lowest voids content, followed by sweeping different paste content (32%-38.4%) aiming to produce a self-compacting concrete (SCC). The concrete was then evaluated as having a high fluidity (class SF1, by T50 testing) in the fresh state, reaching a compressive strength of 64.1 MPa and Young's modulus of 26.2 GPa at 28 days of age in thermal cure conditions.

Keywords: Alkali-activated concretes and pastes; mix design; geopolymers; mechanical properties; alkali dosage.

Highlights

- A mix design method for resistant and fluid alkali-activated pastes and concrete is proposed.
- Binary alkali-activated pastes of fly ash and steel slag present higher compressive strength for lower silica modulus and ash-slag ratios.
- Alkali-activated concrete presented a lower Young's modulus than typical Portland cement concretes with similar compressive strength levels.
- Thermal curing improves strength at early ages compared to ambient curing, but not for higher ages (28 days).

3.1 Introduction

3.1.1 General Motivation for the Research

Over the years, the research on the development of solutions and products with more environmental efficiency is increasing, which is highly related to the concept of limited

resources and the urgent need for more sustainable approaches worldwide, particularly in construction materials. The construction industry is usually referred to as one with the most liability and environmental impact (DELGADO et al., 2019), with massive consumption of non-renewable raw materials (BAIC; KOZIOŁ; MIROS, 2021), and high greenhouse gas emissions (GHG), highly associated to the ordinary Portland cement (OPC) production, corresponding up 5 to 7% of global emissions [SINGH; MIDDENDORF, 2019). In that context, there is a growing tendency concerning the use of alkali-activated binder (AAB) (SINGH; MIDDENDORF, 2019) as a potential replacement for OPC (SINGH; MIDDENDORF, 2019). AABs have the potential to provide further use for industrial coproducts and wastes through their usage as precursors in binder manufacturing (LI et al., 2018; SINGH; MIDDENDORF, 2019).

AABs are obtained by mixing two groups of components: (i) alkaline activation solutions, to dissolve and promote catalysis reactions in (ii) materials with high content of silicon, aluminum (aluminosilicates), and calcium, named precursors, which are typically powder materials, industrial wastes, rich in the aforementioned elements (PROVIS; BERNAL 2014; PROVIS; VAN DEVENTER, 2019; FAROOQ et al., 2021). Examples of activators are solutions of sodium or potassium, hydroxides, and silicates (PROVIS; VAN DEVENTER, 2019; XIE et al., 2020). Examples of precursors are by-products or wastes such as fly ash. blast-furnace slag and steel slag, due to their chemical composition and low value-added (PROVIS; VAN DEVENTER, 2013; SINGH; MIDDENDORF, 2019).

Such binders can either be applied to pastes, mortars or even concretes (PROVIS; VAN DEVENTER, 2013; SINGH 2019, FAROOQ et al., 2021). The main difference in such cases is concerning the presence or not of aggregates, both fine, in the case of mortar, and coarse, in the case of concretes. In all cases, AABs can be used as a partial or total replacement for the Portland cement binder (LI et al., 2019; XIE et al., 2020). Their commercial application in rigid paving, structural building parts, cast in situ or even pre-cast, is already present in countries such as Netherlands, Holland, Czech Republic, and England (PROVIS; BERNAL; 2014). Figure 3.1 illustrates a general overview concerning alkali-activated binders and composites.

Figure 3.1 - Schematic illustration of alkali-activated mixtures

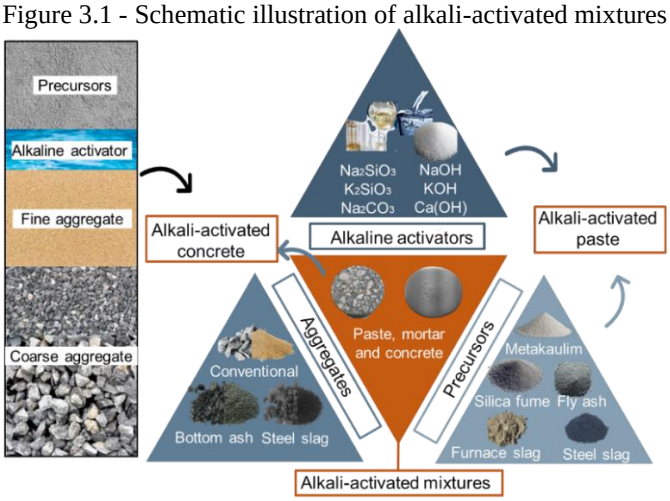

Source: elaborated by the author

The gels formations in alkali activation are dependent on a range of factors such as (i) the chemical composition (activators and precursors); (ii) activator solution alkalinity; (iii) thermal or ambient (room) curing; (iv) the proportion between solution and precursors (solution-to-binder ratio); (v) the precursors specific surface area; as well as the (vi) calcium and magnesium content in the precursors (SOUTSOS et al., 2016; PROVIS; VAN DEVENTER, 2019; XIE et al., 2020). In the alkali activation process, the main product gels are the C-A-S-H (CaO-Al_2O_3-SiO_2-H_2O) and N-A-S-H (Na_2O-Al_2O_3-SiO_2-H_2O). The formation of C-A-S-H or N-A-S-H is a variable depending on the amount of calcium available for the binder (PROVIS; VAN DEVENTER, 2013; PROVIS; VAN DEVENTER, 2019). With the increase of calcium, there is more formation of C-A-S-H.

The adoption of different precursors, due to their different calcium contents, can optimize the AAB formation, by obtaining different proportions of N-A-S-H and C-A-S-H (PROVIS; VAN DEVENTER, 2013; PROVIS; VAN DEVENTER, 2019). Both formed gels impact directly the AAB behavior. However, when compared to OPC, the AAB tends to present a higher chemical attack resistance (BERNAL; PROVIS, 2014; ZHANG et al., 2017), high strength at high temperatures (ZHANG et al., 2020) and lower porosity (BERNAL; PROVIS, 2014; PROVIS; BERNAL 2014). Then, it seems that AAB composition optimization from the investigation of the mix of binary precursors is a feasible approach to design composites with better behavior.

3.1.2 Mix design strategies for alkali-activated binders and concretes and the specific motivation of this study

Concerning mix design for AAB mixtures manufacturing, there are some factors to be accounted for, such as a variation in the activators' and precursors' chemical composition, the complex interaction between the binders' components and the aggregate proportion (XIE et al., 2020; FAROOQ et al., 2021). In addition, the final intended application, either in pastes, mortars or concretes, should also be an influencing factor to be accounted for in the chosen parameters for the design.

The paste mix design method through chemical composition was proven to be efficient (LEE; LEE, 2013; RAFEET et al., 2017; XIE et al., 2020), adopting parameters such as (i) silica modulus (S/N, i.e. SiO_2/Na_2O mass ratio), and (ii) alkali content (N/B, i.e. Na_2O/binder precursors, given in terms of a mass ratio). SiO_2 is derived from sodium silicate and Na_2O from sodium silicate and sodium hydroxide (LEE; LEE, 2013; XIE et al., 2020).

The sodium hydroxide content can be used to change the original S/N of the sodium silicate solution (RAFEET et al., 2017). To establish the ratio between activators and precursors, the N/B can be used (SOUTSOS et al., 2016; LI et al., 2018). The literature reports better results using S/N between 0.5 and 2.5 (SOUTSOS et al., 2016; THOMAS; PEETHAMPARAN, 2017; DING; SHI; LI, 2018) and N/B between 4% and 15% (SOUTSOS et al., 2016; LI et al., 2018).

Concerning composite applications, such as AAB concretes, several studies have proposed mix design methods (PAVITHRA et al., 2016; BONDAR et al., 2019; LI et al., 2019; XIE et al., 2020). Among them, methodologies that apply packing to determine the aggregate ratios and adjust the paste content are one of the most efficient, for reaching good workability, strength, and other aspects. However, there is still an important remaining gap in the literature, concerning the development of simplified methodologies that enable starting from a chosen set of viable precursors and activators and obtaining concretes with desired strength and consistency.

Concerning the adopted materials as precursors, the literature frequently highlights fly ash (FA) and blast furnace slag combination (SOUTSOS et al., 2016; LI et al., 2018; PROVIS; VAN DEVENTER, 2019) as a good set with potential for AAB paste manufacturing, but other precursors with lower value-added, such as steel slag, produced in the Basic Oxygen Furnace (BOF) and Electric Arc Furnace (EAF) processes, (NAIDU; SHERIDAN; VAN DYK, 2020; NUNES; BORGES, 2021) have also interesting potential. The low application of steel

slag occurs due to the lower amount of amorphous silica and significant contents of iron oxide compared to other slags, being nowadays used mainly for soil stabilization and concrete applications, as aggregate (NUNES; BORGES, 2021).

The application of steel slag in AAB is presented as a solution for proper management of such by-products, with potential use on an industrial scale (NUNES; BORGES, 2021). In 2021, the world production of crude steel was 1.95 billion tons (WSA, 2021), with a major part having no other high-value destination, frequently destinated to landfill. Each ton of steel produced is estimated from 10% to 15% of steel slag generation (HORII et al., 2015). Fly ash, on the other hand, is a great source of aluminosilicates (in particular class "F" (fly ash, with low calcium oxide content (CaO $\leq$ 18%) and potentially presenting pozzolanic activity) (ELAHI et al., 2020). In 2016, its production was 1.1 billion tons worldwide, with a productive surplus, and an average use rate of 60% (JIN et al., 2021). Its combination with steel slag is potentially able to produce a good mix for binary designs.

Song et al. (SONG et al., 2019) adopted electric arc furnace steel slag as FA partial replacement, in the contents of 10%, 20%, 30% 40%, and 50%, w/w. Sodium hydroxide and silicate were used as activators, composing a solution with 1.6 silica modulus (S/B) and 0.65 solution/binder ratio (N/B). The best replacement rate was 20% once there was an improvement in workability, setting time, and compressive strength (25 MPa), considering the analysis of the binder's behavior.

Cristelo et al. (2019) evaluated the replacement of electric arc furnace steel slag both as precursor and aggregate in alkali-activated mortars based on fly ash as a precursor and normalized sand as aggregate, activated with sodium hydroxide (8 mol/L). It was concluded that the most appropriate fly ash replacement proportion was 50% for the precursor and 100% for the aggregate, achieving a compressive strength of 28 MPa, for 28 days, considering the analysis of pastes and mortar behaviors.

Despite the number of cited studies on the mechanical properties of alkali-activated binders, there are still few thorough studies starting from the binder mix design going through the pastes and the composite's fresh state and evaluating the composite's strength evolution with age. Also, studies on alkali-activated materials based on fly ash and steel slag are still incipient and not integrated concerning paste or concrete (CRISTELO et al., 2019; NAIDU; SHERIDAN; VAN DYK, 2020, NUNES; BORGES, 2021).

3.1.3 Research objective and basic scope of materials

The current paper aims to propose an efficient mix design method for low-carbon AAB mixtures, by using fly ash and steel slag to manufacture pastes and concretes and evaluating materials' fresh and hardened states. In addition, it intends to: (i) evaluate the mix design parameters (S/N and N/B), and curing method influence on the achieved results of setting time, mini-slump and compressive strength; (ii) analyze the potential use of steel slag in binary designs with FA for AAB manufacturing; and (iii) assess the performance of AAB applied in a concrete application by determining some composite parameters such as slump flow, T50, compressive strength, and Young's modulus, and comparing with expected results for a typical conventional cement Portland concrete.

The AAB pastes used in this study are manufactured with a binary mixture of fly ash (FA) and a type of steel slag (SS) obtained in the basic oxygen furnace process (BOF), both by-products obtained from local industry in Ceará, Brazil. Meanwhile, the alkaline activators are composed of sodium hydroxide and silicate, obtained commercially. Concretes were cast to validate the proposed mix design method by incorporating AAB to natural fine aggregate (river quartz sand) and two sizes of crushed aggregate (obtained from granite rocks), as typically used in conventional concrete in the region of the study.

3.2 Materials

The precursors were pre-processed using mechanical crushing and sieving to the reduce particles' size. For both precursors only particles passing 150 µm sieve were used, aiming at improving the AAB paste formation and the quality control of the raw materials (PROVIS; VAN DEVENTER, 2013, SOUTSOS et al., 2016).

The investigated FA presented 2.341 for specific gravity (NBR 16,605, 2017) and 4,790 cm^2/g for specific surface area **(**NBR 16,372, 2015**).** For the SS, the values were 3.127 g/cm^3 and 3,360, respectively. Both the specific surface area and particle size distribution (PSD) influence the water demand on the mixture and its respective reaction kinetics (2016). The specific surface area values were higher for FA and lower for SS than those presented by Lee and Lee (2013) with 2,900 cm^2/g and 4,850 cm^2/g and Li et al. (2018) with 2,900 cm^2/g and 4,460 cm^2/g, for the FA and SS, respectively.

The precursors' laser particle size distribution (PSD) was obtained with a Shimadzu SALD-2300. FA obtained an average diameter of 5.6 µm and a maximum size of 106.9 µm, while the SS had an average of 35.4 µm with a maximum diameter of 141.0 µm. For the X-Ray

Fluorescence (XRF), a Rigaku ZSX Mini II was used, obtaining the oxides contents composition expressed in Table 3.1.

Table 3.1 - Chemical composition of precursors

Material	Al_2O_3	SiO_2	P_2O_5	SO_3	Cl	K_2O	CaO	TiO_2	MnO	Fe_2O_3
Steel Slag (%m.)	**1.94**	**5.64**	0.84	0.83	0.04	0.14	**53.14**	-	2.97	**34.40**
Fly Ash (%m.)	**11.14**	**42.17**	0.53	1.08	0.06	3.97	**10.25**	2.74	0.27	**26.98**

Source: research data

The FA presented Al_2O_3 contents of 11.14%, 42.17% of SiO_2, and 10.25% of CaO, being classified as class "F" (ASTM C618, 2019), which means that it may present pozzolanic activity. Both precursors presented significant Fe_2O_3 contents, which can inhibit the formation of C-A-S-H in high calcium AABs and/or take up the position of Al^{3+} in octahedral sites for low calcium AABs (XIE et al., 2020) The precursors' microscopy by scanning electronic microscopy (SEM) is presented in Figure 3.2.

Figure 3.2 - SEM images of precursors

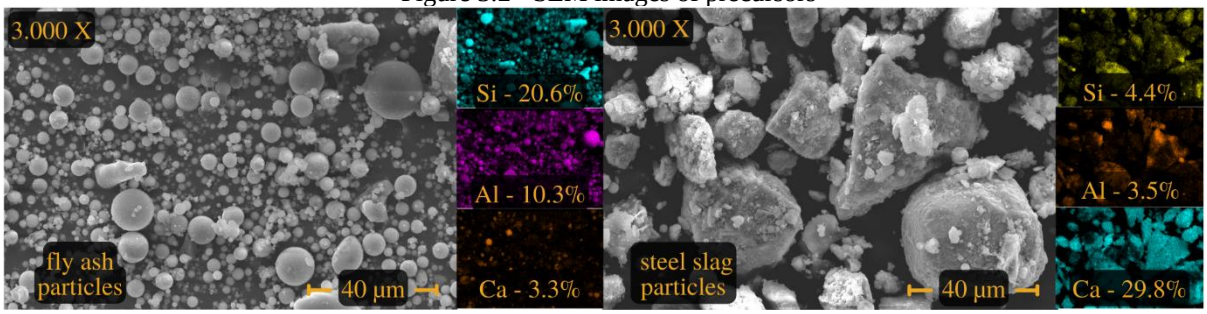

Source: elaborated by the author

As expected, FA particles presented a spherical shape finer than the slag particles, which presented an angular shape. With the energy dispersive spectroscopy (EDS), performed simultaneously with the SEM, it was also possible to estimate its calcium, silicon, and aluminum contents. The steel slag presented a higher calcium content, directly influencing the gels' formation (PROVIS; VAN DEVENTER, 2013) as mentioned before.

The sodium hydroxide presented a purity of 97.9% being used as a solution with a concentration of 10 mol/L. In mass proportion, it was defined as 31.3% hydroxide and 68.7% of water, proportions like those of Rafeet et al. (2017). The hydroxide solution concentration (10 mol/L) was chosen according to literature recommendations (YUSUF et al., 2014, NAGARAJ; VENKATESH BABU, 2018) and presented specific gravity of 1.305. The sodium silicate showed a chemical composition, by mass ratio, of 14.98% Na_2O, 31.83% SiO_2, and 53.19% H_2O and specific gravity of 1.575.

Concerning the aggregates, as fine aggregate it was used river quartz sand with a specific_gravity of 2.573, void content of 42%, and 2.66 of fineness modulus (NBR NM 248,

2003; NBR 7,211, 2019; NBR 16,916, 2021)**.** For the coarse aggregate, crushed granite was used, with two different gradations (one ranging from 4.75 mm to 12.5 mm and the other from 9.5 mm to 25 mm). Specific gravities were 2.617 and 2.629, void content of 46.3% and 43.4%, 0.61% and 0.59% of water absorption, respectively **(**NBR NM 248, 2003; NBR 7,211, 2019; NBR 16,972, 2021; NBR 16,916, 2021). The aggregate composition was chosen aiming to achieve a minimum void content, as discussed in Section 3.3.3.1.

3.3 Mix design procedure for alkali-activated binder (AAB) pastes and concrete

3.3.1 Proposed general scheme for an alkali-activate mix design method

A brief schematical description of the general mix design methodology is presented in Figure 3.3 and is divided into two stages: whereas the first stage focuses on the pastes, the second focuses on the concrete. It is inspired by previous results and recommendations from the literature (O'REILLY, 1998; GOMES; BARROS, 2009; SOUTSOS et al., 2016; RAFEET et al., 2017; THOMAS; PEETHAMPARAN, 2017; DING; SHI; LI, 2018; LI et al., 2018; LI et al., 2019), but contributes by proposing simplified mix design methodology to produced binders and concretes with the desired strength and consistency.

Figure 3.3 - Mix design of alkali-activated pastes and concrete

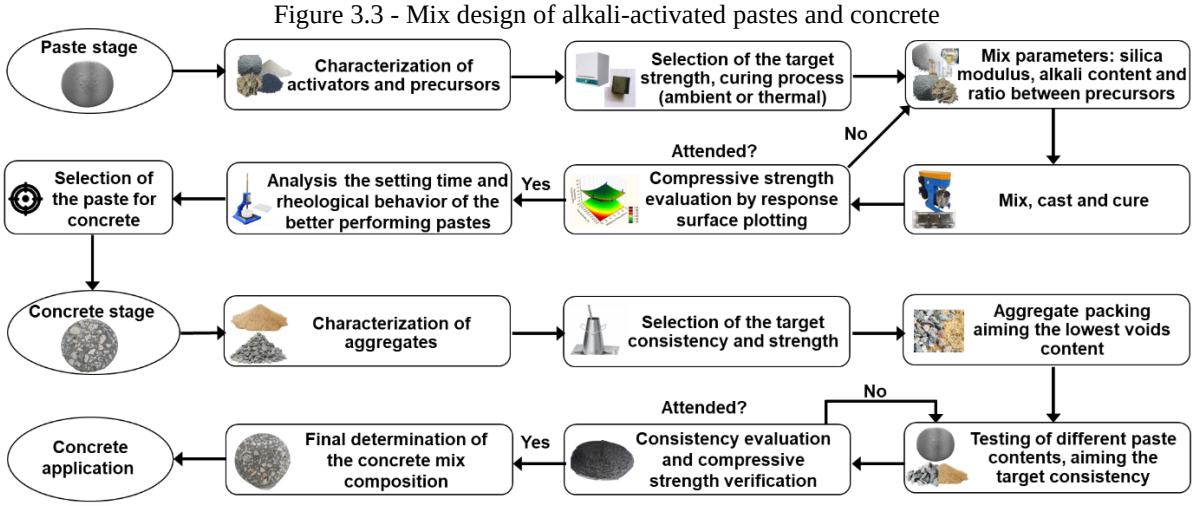

Source: elaborated by the author

For the paste mix design, the first aspect to be accounted for is the desired compressive strength. From this requirement, the activator mix design parameters, its concentration, and the proportion between the adopted types of activators and precursors, when applicable, can be determined.

Based on the chemical composition of the activators, it is feasible to determine both S/N and N/B parameters, accounting for the design parameters defined previously. Activators'

molar concentration is also a parameter to be defined simultaneously to calculate S/N and N/B. For silica modulus (S/N), it is recommended a range of from 0.5 to 2.5 (SOUTSOS et al., 2016; THOMAS; PEETHAMPARAN, 2017, DING; SHI; LI, 2018), and for alkali dosage (N/B) a range of 4 to 15% (SOUTSOS et al., 2016; LI et al., 2018).

In the next step, it is established the precursors' proportions. One key parameter for that case, based on literature, is their chemical composition. According to the literature, Si/Al proportion ratios between 1 and 3 can be adopted for better mechanical properties (ZHANG; AHMARI; ZHANG, 2011; PROVIS; VAN DEVENTER, 2013). Additionally, the literature also points out that the proportions of aluminum, silicon, and especially calcium influence setting time and microstructural enhancement on the different gels synthesis (C-A-S-H and N-A-S-H) (PROVIS; VAN DEVENTER, 2013). Then, this is an interesting aspect for investigation, where the calcium proportion is more intrinsic to the setting time properties, whereas its increase occurs in a decrease of such parameters (NATH; SARKER, 2014).

Finally, the curing method is defined either as ambient temperature or as thermal curing for different groups of specimens. For ambient curing, performed at room temperature, the specimens were stored in ambient temperature and humidity conditions. For thermal curing, the literature points out temperatures from 60 to 70 °C, for the first 24 hours (YUSUF et al., 2014; COSTA, 2022) and the chosen value for this paper was 65 °C during 24 hours in the laboratory oven.

With the determination of the alkali content, silica modulus, type and ratio between precursors and the curing process the evaluation step of the pastes can be started. Additional specifics of the formulation evaluated in this research are discussed in Section 3.3.2. The bounds of the experimental program are summarized in Table 3.2.

Table 3.2 - Binder mix design experimental verification, 36 combinations

Parameters	Min.	Max.	Var.	Total
S/N (ad)	0.75	1.75	0.50	3
N/B (%)	6.0	10.0	2.0	3
Precursors (FA-SS)	75-25	50-50	-	2
Curing Method	Ambient (25 °C)	Thermal (65 °C)	-	2

Source: research data

After the definition of the experimental bounds, different pastes within those bounds were manufactured and tested for compressive strength at 28 days, as its first evaluation. Based on the results, it was possible to interpolate a compressive strength surface response for the pastes, relating the parameters of silica modulus and alkali dosage with the strength output. The visual aspect of the alkali-activated pastes manufactured is presented in Figure 3.4.

Figure 3.4 - Alkali-activated pastes aspect

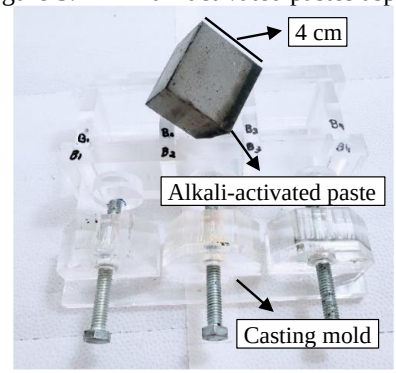

Source: elaborated by the author

Based on the results, the most resistant pastes were replicated for complementary tests (single-point or multipoint rheological tests and setting time), to assess fresh state properties, in addition to the compressive strength for other ages (7, 14 and 28 days) to evaluate the material's behavior over time. Fresh state properties can be assessed through mini-slump and rheological flow tests. Furthermore, it is necessary a proper setting time, that permits conditions for production, transportation, and densification, with a minimum recommended time of 150 minutes (ASTM C94, 2014**;** NBR 7,212, 2021).

For the application in concretes, there are also some additional parameters and procedures to be accounted for, such as: (i) aggregates characterization (specific and apparent specific gravity, water absorption, voids content, particle size distribution, etc.); (ii) determination of the best aggregates' proportion, based on the packing proportion through void content analysis (%V); (iii) determination of the compressive strength and required consistency; and (iv) the initial estimation of paste content based on the aggregates' void content. The paste content was chosen according to the voids to be filled between the aggregates, considering the targeted strength and workability parameters, being common values of paste content higher than 10% of the voids content to obtain concrete with high workability in the fresh state (GOMES; BARROS, 2009; RAFEET et al., 2017; LI et al., 2019). Figure 3.5 presents the aspect of the cast alkali-activated concretes.

Figure 3.5 - Alkali-activated binder in the concrete application

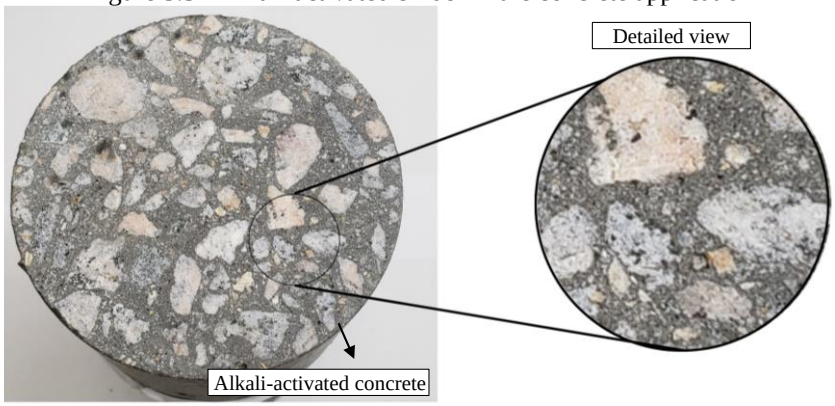

Source: elaborated by the author

Regarding AAB concrete strength, small decreases with respect to AAB are expected due to aggregate resistance and the presence of an interfacial transition zone (binder/aggregate) (LUO et al., 2021; FAROOQ et al., 2021). Concerning the adjustments during the concrete preparation, it proceeded in gradual corrections of 5% of binder mass until it reached the desired consistency (slump flow class 1 or higher). Once those criteria were fulfilled, the concrete formulations for each curing process were chosen. Then, a minimum of three specimens for each mechanical analysis was prepared to calculate the average and standard deviation of the results.

3.3.2 Pastes and concrete mix designs

Once the binder design method was defined, different pastes were cast to initially assess their compressive and flexural strength at 28 days. The target compressive strength was defined as 50 MPa for ambient curing, at room temperature, and 60 MPa for thermal curing (65 °C), to support the production of high-strength concrete. Formulations with the 3 highest strengths were evaluated for the fresh state, conducting mini-slump tests, and then, at the hardened state, compressive strength tests were conducted at 7 days. SEM tests were performed on binder pieces obtained from the rupture for microstructural analysis on the equipment Quanta 450 FEG – FEI.

The paste formulations were designed with varied parameters whose ranges were based on literature, accounting for precursors and activators' chemical profiles, sweeping different compositions to construct strength outputs afterward. Silica modulus (S/N), alkali content (N/B), and curing process were variated according to the targeted bounds in Table 3.2, resulting in 18 combinations. Table 3.3 presents the design for each formulation, which then will be prepared either with ambient curing or thermal curing.

Table 3.3 - Formulations design for the initial assessment of the pastes mix design

Paste ID	FA-SS	S/N	N/B	Sodium Hydroxide		Sodium Silicate		Fly Ash		Steel slag	
				(kg/m³)	% vol.	(kg/m³)	% vol.	(kg/m³)	% vol.	(kg/m³)	% vol.
1	75-25	0.75	6.0	261.1	20.0	230.6	14.6	1223.3	52.3	407.8	13.0
2	75-25	0.75	8.0	312.0	23.9	275.6	17.4	1096.5	46.8	365.5	11.7
3	75-25	0.75	10.0	353.4	27.1	312.1	19.7	993.5	42.4	331.2	10.6
4	75-25	1.25	6.0	162.1	12.4	374.9	23.7	1193.3	51.0	397.8	12.7
5	75-25	1.25	8.0	192.8	14.8	445.9	28.2	1064.5	45.5	354.8	11.3
6	75-25	1.25	10.0	217.5	16.7	503.1	31.8	960.8	41.0	320.3	10.2
7	75-25	1.75	6.0	67.8	5.2	512.3	32.4	1164.7	49.8	388.2	12.4
8	75-25	1.75	8.0	80.2	6.1	606.6	38.3	1034.3	44.2	344.8	11.0
9	75-25	1.75	10.0	90.2	6.9	681.9	43.1	930.2	39.7	310.1	9.9
10	50-50	0.75	6.0	273.1	20.9	241.2	15.2	852.9	36.4	852.9	27.3
11	50-50	0.75	8.0	324.8	24.9	286.9	18.1	760.9	32.5	760.9	24.3
12	50-50	0.75	10.0	366.5	28.1	323.7	20.4	686.8	29.3	686.8	22.0
13	50-50	1.25	6.0	169.3	13.0	391.6	24.7	831.1	35.5	831.1	26.6
14	50-50	1.25	8.0	200.4	15.4	463.6	29.3	737.8	31.5	737.8	23.6
15	50-50	1.25	10.0	225.2	17.3	521.0	32.9	663.4	28.3	663.4	21.2
16	50-50	1.75	6.0	70.7	5.4	534.6	33.8	810.3	34.6	810.3	25.9
17	50-50	1.75	8.0	83.3	6.4	629.9	39.8	716.1	30.6	716.1	22.9
18	50-50	1.75	10.0	93.3	7.2	705.4	44.6	641.5	27.4	641.5	20.5

Source: research data

The aforementioned proportions were near those of Song et al. (2019), Cristelo et al. (2019) and Costa (2022), concerning the replacement of FA with steel slag up to 50%. The silicon-aluminum ratio was kept between the median values ($1 < Si/Al < 3$) (ZHANG; AHMARI; ZHANG, 2011; PROVIS; VAN DEVENTER, 2013).

Ambient curing had an average temperature near 25 °C (room temperature at the air in a lab in Fortaleza, Brazil, where humidity is around 65%-85%). The specimens were maintained for 24 hours minimum until the unmolding. Thermal curing was at a temperature of 65 °C for 24 hours in the laboratory oven. After unmolding and prior to testing, all specimens (both for ambient and for thermal curing) were kept at room temperature (25 °C). Thus, 36 binders (18 formulations for ambient curing and 18 formulations for thermal curing, as presented in Table 3.3) were analyzed. In the initial evaluation, all compressive tests were conducted at 28 days. The highest strength pastes were replicated and submitted to mini-slump and setting time determination (NBR 16,607, 2018; ASTM C191, 2021). This second criterion aimed to align the best strength with appropriate consistency and fluidity, aiming at a lower viscosity, an important matter for concrete applications (XIE et al., 2020).

The results of compressive strength were statistically analyzed using the software Statistica V10®. Outliers were identified, through standardized residuals, and suppressed (a total of 2/126 data points were suppressed). Analysis of variances (ANOVA) was applied to identify what parameters had the most significant influence, individually and combined, and

also to evaluate the homogeneity of variances. This allowed identifying the best combinations for compressive strength at 28 days.

With the best binder defined, it was employed in concrete manufacturing. Regarding the mechanical properties, it was sought to obtain a compressive strength higher than 50 MPa, regardless of the curing method. One of the major concerns about AAB paste applications for concretes is about the workability and consistency in the fresh state (RAFEET et al., 2017, LI et al., 2019). In this way, the consistency parameter chosen for the fresh state was concrete with self-compacting characteristics, i.e., a material that can flow homogeneously under the action of its own weight.

The optimal aggregate proportion was determined through packing analysis (O'REILLY, 1998; GOMES; BARROS, 2009) on different combinations, 5% by 5% of increment, using the two gravels mentioned earlier. The best arrangement for the coarse aggregate was found for 40% crushed 4.75-12.5 mm aggregate and 60% crushed 9.5-25 mm aggregate, achieving a voids content of 41.37%, similar to the results of Rafeet et al. (2017). Then, the packing between the coarse and fine aggregate was done in the same manner. The best composition was 35% of sand and 65% of the previously resultant coarse aggregate, with a voids content of 31.95%, similar to Bondar et al. (2019).

Concerning the binder volume, as mentioned, the voids content to be fulfilled was nearly 32%. So, it was tested with paste contents of 33.6% (5% higher than the void content), 35.2% (10%), 36.8% (15%) and 38.4% (20%), being paste content aligned with Bernal et al. (2011), Rafeet et al. (2017), and Bondar et al. (2019), with employed binder content ranging from 30% to 40% in volume.

The initial consistency verification was conducted through a slump test (ASTM C143, 2015; NBR 16,889, 2020), aiming at increasing the slump, up to its test limit of 270 mm. Once this level was achieved, the specimen was subjected to the slump flow and T50 (ASTM C1611, 2010, NBR 15,823-2, 2017). With this latest parameter, consistency could be determined, aiming at high fluidity. The above dynamic is illustrated in Figure 5.6, concerning the main stages for binder mix design and final composite applications.

Figure 3.6 - Summary of binder mix design

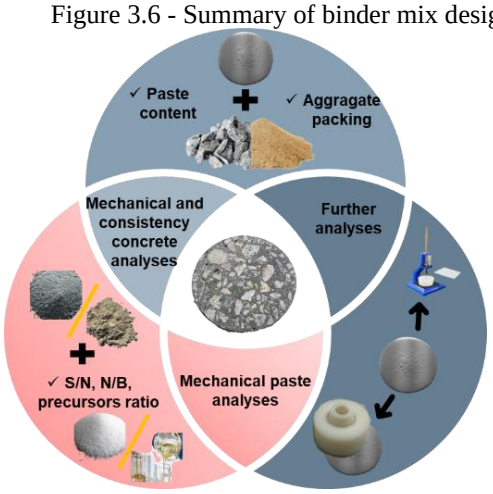

Source: elaborated by the author

The chosen paste formulation parameters for concrete application were: an alkali content of 10%, a silica modulus of 0.75, and a fly ash-steel slag ratio of 75%-25%. Concerning the concrete aggregate, it was defined a proportion of 35% sand to 65% gravel, by mass and a paste content of 38.4% (20% higher than the void content). The concrete formulation produced is illustrated in Table 3.4.

Table 3.4 - AAB concrete formulation

Materials	(kg/m³)	% vol.
Fly Ash	382.1	16.3
Steel Slag prec.	127.4	4.1
NaOH (solution) - 10 mol/L	135.9	10.4
Na_2SiO_3 (solution)	120.1	7.6
Fine aggr.	561.6	21.8
Coarse aggr. 4.75-12.5 mm	417.2	16.0
Coarse aggr. 9.5-25 mm	625.8	23.8

Source: research data

3.3.3 Mixture, specimens manufacturing and testing procedure

The mix procedure of AAB paste manufacturing was standardized as follows: (i) 1-minute pre-homogenization; (ii) 1 minute and 30 seconds of low rotation mixing at 62 ± 5 rpm (low speed); (iii) 1-minute pause for homogeneity check; (iv) 1 minute and 30 seconds mixing at 62 ± 5 rpm. All procedures were performed in a planetary mixer with a volume of prepared material of 1.5 L. After, it proceeded with the molding.

All specimens for thermal curing were cast in acrylic cubic forms, with a 4 cm edge. A minimum of triplicate specimens was fabricated for each mix design and curing method (3 specimens for each formulation). The specimens for ambient curing were molded in 4 cm × 4 cm × 16 cm with the same material. Three prisms were tested for flexural strength, and from

the resulting parts after rupture, three samples were meant for compressive strength, all for 28 days of age.

The binder compressive tests (NBR 13,279, 2005; ASTM C349, 2018) were performed at 28 days with a loading rate of 500 ± 50 N/s. For flexural strength (ASTM C348, 2021), it was used a three-point flexion loading application, with a rate of 50 ± 10 N/s. The tests were performed on a universal testing machine with a capacity of 300 kN (EMIC GR048). The thermal curing for prismatic specimens may lead to the formation of cracks in the material, directly affecting flexural strength (SONG et al., 2019). Therefore, only the flexural strength of AABs pastes under ambient cure was evaluated **(**NBR 13,279, 2005**).**

As mentioned before, the 3 pastes with the highest strengths were selected to also be investigated with mini-slump and setting time analyses (NBR 16,607, 2018; ASTM C191, 2021). In addition, all those pastes were meant for SEM analysis to assess microstructure.

As detailed in the previous section, the AAB concretes were cast using: (i) the best AAB paste formulation, based on mechanical and rheological aspects, (ii) natural fine aggregate, and (iii) two granulometries of coarse aggregate. Concerning the concrete mixing, the procedure was standardized as follows: (i) insertion of the coarse aggregate and 10% of the activator solution in the mixer with 2 minutes of mixing, (ii) addition of the homogenized precursors and 80% of the activator solution over 4 minutes of mixing, (iii) addition of the fine aggregate with 4 minutes mixture (iv) addition of the remaining activator solution with 2 minutes mixing. All procedures were performed in a planetary mixer with a volume of prepared material of 24 liters.

Once finished the concrete mix, it was proceeded with the fresh state characterization through slump test and slump flow (ASTM C1611, 2010; ASTM C143, 2015; NBR 15,823-2, 2017**).** At last, the specimens were cast (NBR 5,738, 2016). The concrete was molded using PVC formworks with a cylindrical shape of 10 cm diameter and 20 cm height, whereas 3 specimens were molded to compressive strength (NBR 5,739, 2018; ASTM C39, 2020**)** and 3 only to Young´s modulus (NBR 8,522-1, 2021; ASTM C469, 2022) testing. The tests were performed on a universal testing machine (EMIC PCE100C) with 1000 kN capacity with a loading incremental rate of (0.45 ± 0.15) MPa/s. Young´s modulus was estimated based on the strain of 30% of the ultimate strength. The longitudinal deformations were measured with a linear variable differential transformer (LVDT). The concretes were also characterized by the physical aspects of density and porosity. Analyses were performed on specimens submitted to ambient and thermal curing, considering the same conditions applied to the pastes.

3.4 Compressive strength and complementary tests in the fresh and hardened states

3.4.1 Alkali-activated pastes

3.4.1.1 Compressive strength and flexural strength results

Figure 3.7 presents the results of the pastes tested during mix design for all 18 formulations and the 2 curing processes (Table 3.3). The highest average strength values (pastes 1, 4, 7, 10, 13 and 16), under the thermal curing process, were obtained for an N/B of 6%. This can be attributed to the lower amount of free water associated with this content compared to the 8% and 10% contents, as visualized in Table 3.3 due to the low amount quantity of activator solution (LI et al., 2019). Even though they had more volume of solution, those pastes presented a difficult casting. Then, despite the high strength, they were not selected for the concrete application.

Figure 3.7 - 28 days compressive strength results of AAB pastes

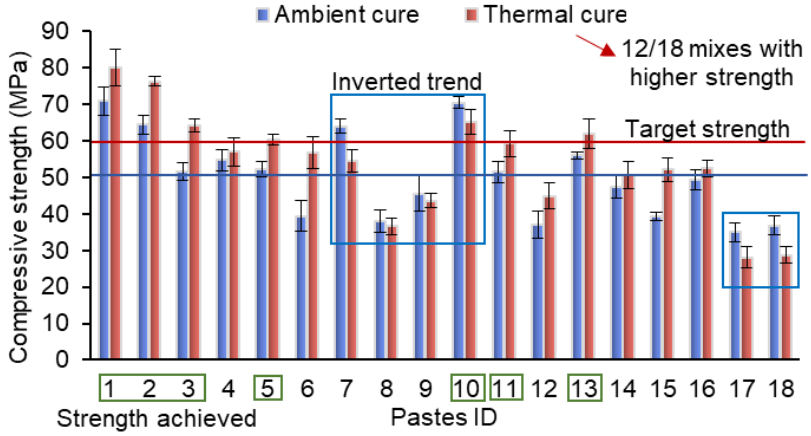

Source: elaborated by the author

Analyzing the results, 9 out of the 18 formulations presented high compressive strength, with values above 50 MPa under ambient curing, and 7 out of 18 above 60 MPa under thermal curing (pastes 1, 2, 3, 5, 10, 11 and 13). The higher compressive strength (paste 1) was 70.9 MPa for ambient curing and 80.1 MPa for thermal curing. Paste 1 is composed of 0.75 of silica modulus, 6% of alkali content, and FA-SS of 75-25. It is highlighted that the presented values exceed previous results from the literature concerning steel slag and FA, with the same activator solutions, which had obtained compressive strength average results of 25 MPa for ambient curing and 39 MPa for thermal curing (GUO; PAN, 2018; SONG et al., 2019; CRISTELO et al., 2019). This is probably due to the chemical composition of activators and precursors, the granulometry and reactivity of the precursors, and the binder mix design.

The thermal curing did not lead to a compressive strength increase in all formulations (6 out of 18 formulations had an inverted trend). The strength reductions noticed

for those cases happened especially for compositions with S/N of 1.75. In all combinations with this observation, high strengths were obtained (identified by the blue samples in Figure 3.7). This phenomenon may be associated with the larger amount of SiO_2 initially available for structure formation. Although the literature review points out that thermal curing usually leads to a strength increase, the opposite behavior had already been observed. Soutsos et al. (2016) found higher compressive strength for AAB pastes under ambient curing at 20 °C compared to thermal curing at 70 °C for a similar proportion of FA (40%) and a blast furnace slag (60%).

Using the results from Figure 3.7 and the compositions from Table 3.3, response surfaces were constructed (Figure 3.8). The response surface figures allow a clear evaluation of how the variation of N/B (x-axis), S/N (y-axis), the proportion of precursors (Fig 8 "a" and "b" with 75-25% FA-SS and "c" and "d" with 50-50% of FA-SS) and curing process (Fig 8 "a" and "c" as ambient and "b" and "d" as thermal) impact the compressive strength results (z-axis).

Figure 3.8 - Compressive strength at 28 days of AAB pastes
(a) FA-SS 75%-25%, ambient cure (25 °C), (b) FA-SS 75%-25%, thermal cure (65 °C)
(c) FA-SS 50%-50%, ambient cure (25 °C), (d) FA-SS 50%-50%, thermal cure (65 °C)

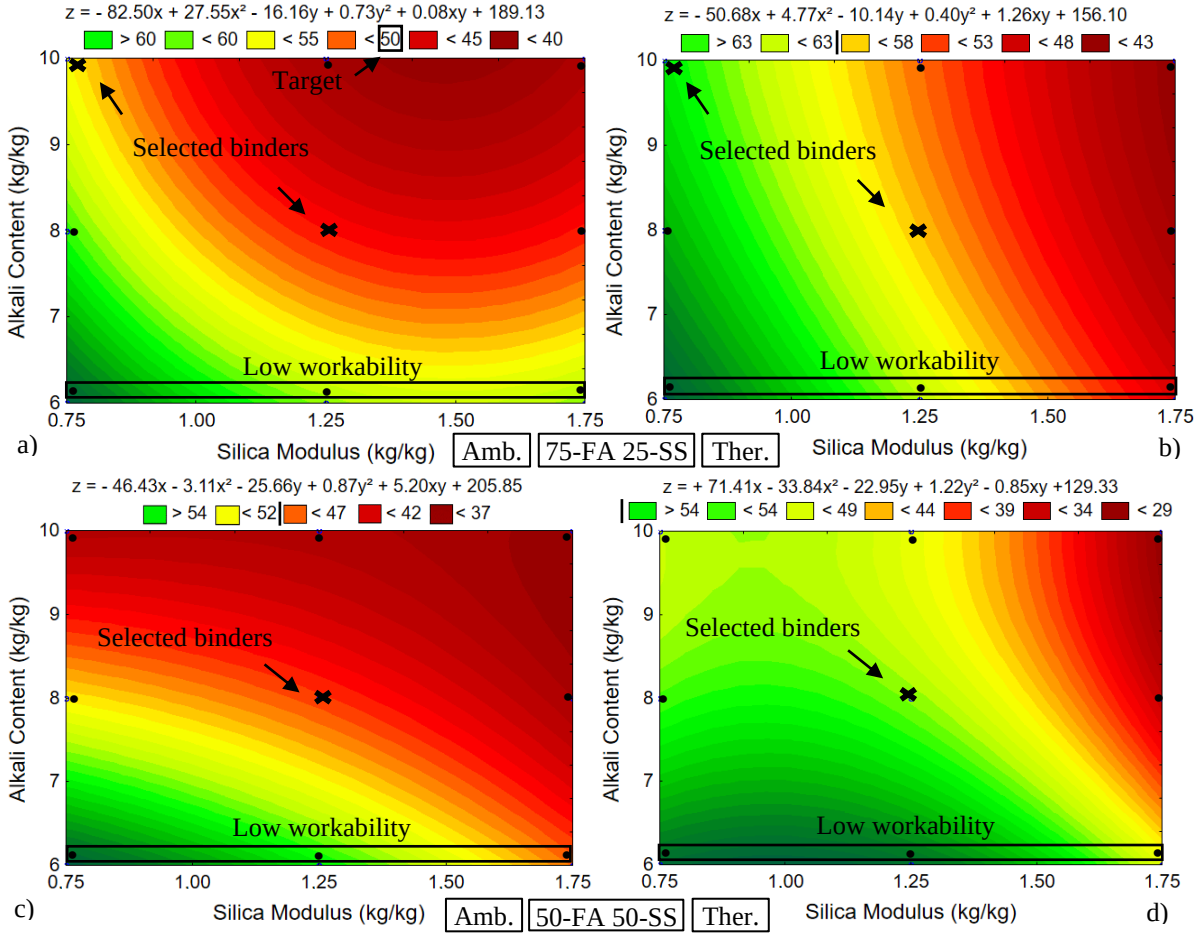

Source: elaborated by the author

The variation of the silica modulus of the activator demonstrated a significant influence on the compressive strength. A lower silica modulus (S/N) results in higher compressive strength, and the best results were those obtained for the silica modulus of 0.75. This result diverged from the literature for binary blends of blast furnace slag with FA. It usually shows better strength for S/N between 1.25 and 2.5 (XIE et al., 2020). This reveals that this kind of slag still needs further research and cannot be considered with the same parameters as blast furnace slag, which are more common in the literature. The high Fe_2O_3 contents in the investigated slag (Basic oxygen furnace slag) may be associated with this phenomenon because there are almost no studies to evaluate its influence on alkali-activation reactions (XIE et al., 2020, CHOI; LEE, 2012). The results of thermal curing presented higher strength for S/N of 0.75 and 1.25. Furthermore, thermal curing showed higher strength gains for higher alkali contents and lower silica modulus, especially for N/B of 10% and S/N of 0.75, as seen in Figure 3.8. This may be associated with the higher amount of alkalis and the proper amount of soluble silica to accomplish the alkali-activation process.

Concerning the analysis of variance (ANOVA), all variables (N/B, S/N, precursor ratio and curing process) had a significant influence on the compressive strength, as well as the interaction between the variables also proved the same behavior, with a significance level of 95% (“F” value of 1.585). By the Duncan test results, it was observed that, concerning thermal curing, only 4 formulations fulfilled the minimum resistance requirements (60 MPa), whereas only 3 of them presented a significant difference from each other (binders 3, 5 and 11), identified with an "x" mark in Figure 3.8. Then, then were chosen for the upcoming analysis (fresh state criterion and hardened state strength evolution). It is important to highlight that, to this selection, the pastes with an alkali content of 6% were not considered, due to their apparent high viscosity, as outlined in Figure 3.8.

The flexural strength values of the pastes cured at room temperature, as well as their percentage in comparison to the compressive strength, are presented in Figure 3.9. The AABs pastes showed an average flexural strength of 4 MPa. The results of flexural strength in terms of maximum admissible tensile stress presented an average of 8.2% of the compressive strength of the same AAB paste. These values were lower than those found in the literature. Song et al. (2019) found proportions of 13% for the FA-based AAB and 19% with 50% steel slag content. Guo and Pan (2018) found a 19% average for a binder of 70% FA and 30% steel slag.

Figure 3.9 - 28-day flexural strength results of AAB, ambient cured
(a) Flexural strength, (b) Flexural/compressive strength ratio

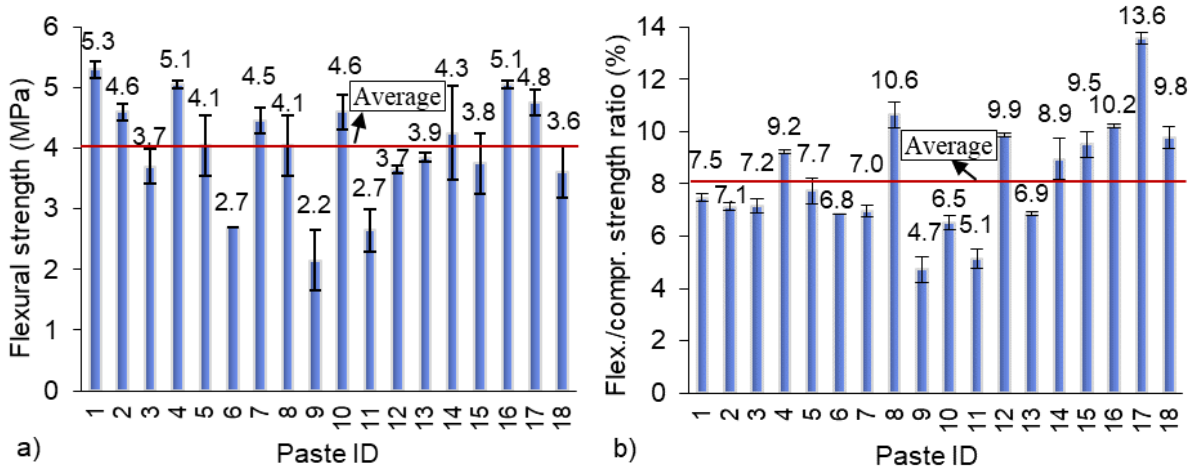

Source: elaborated by the author

3.4.1.2 Results of complementary tests in the fresh and hardened states

The pastes chosen by the first strength criterion (Section 3.1.1) were formulations 3, 5, and 11, whose formulations can be assessed in Table 3. Due to their design parameters, pastes 3, 5, and 11 presented solution/binder (S/B) ratios of 0.5, 0.45, and 0.40, respectively. Pastes 3 and 11, with 0.75 of S/N, presented the same proportions for hydroxide and silicate, while paste 5, with 1.25, presented a greater content of sodium silicate compared to the content of hydroxide. Another important aspect is that Paste 3 had an alkali dosage of 10% (N/B). Despite that, paste 3 had a greater amount of activator than Pastes 5 and 11, which have an alkali content of 8%. It is also important to mention that Pastes 3 and 5 had a ratio between the precursors of 75% fly ash to 25% BOF-type steel slag, while Paste 11 was composed of a 50%-50% ratio of ash to steel slag.

These formulations were replicated for setting time and mini-slump tests. Figure 3.10 presents the results for the initial and final setting time test.

Figure 3.10 - Setting time of AABs pastes 3, 5 and 11

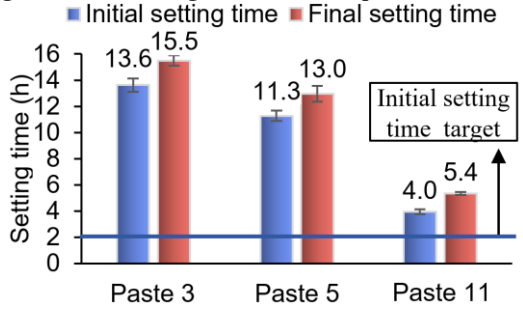

Source: elaborated by the author

All three pastes achieved the minimum initial setting time requirement (150 minutes or 2.5 h) with values similar to ASTM C94 (2014) and NBR 7,212 (2021). However, it is seen

that setting time may be longer than expected for classical cement pastes (classically around 2h-3h), but this may be necessary with AAB paste due to the possibility of unforeseen events during concrete casting, that could reduce the setting time of alkali-activated materials (NATH; SARKER, 2014; HADI; ZHANG; PARKINSON, 2019; XIE et al., 2020). Such events may be related to (i) the high temperature of components, due to high environmental temperature and sun incidence, (ii) calcium content in aggregate (iii) manufacturing process issues, etc. Pastes 3 and 5 had a longer initial result than Paste 11, with 13.6 h and 11.3 h, respectively.

Another concerning point is the calcium content influence, mainly for steel slag composition, which may interfere by reducing the initial setting time (NATH; SARKER, 2014; HADI; ZHANG; PARKINSON, 2019). As seen in Figure 3.10, paste 11 showed a large reduction in the initial and final setting times, with an initial setting time of 4 hours. This can be justified due to its precursor ratios of 50% FA to 50% SS, while pastes 3 and 5 presented ratios of 75% FA to 25% SS, as seen in Table 3.3. Moreover, pastes 3 and 5 showed high values of setting time, common to binders of FA (NATH; SARKER, 2014; HADI; ZHANG; PARKINSON, 2019) and the 25% addition of SS did not impact this parameter. This can be explained due to the SS's lower calcium content, compared to other precursors, such as blast furnace slag and metakaolin. At last, it is seen that all the setting-time periods (difference between final setting time and initial setting time) were very close, being reached within at least two hours after the first determination.

The results of the mini-slump test are presented in Figure 3.11. The spreading diameter was measured at 30, 90 and 300 seconds. All results are in a triplicate, at minimum. Paste 3 presented the highest spread, with an 11.0 cm initial diameter value, followed by Paste 5 and Paste 11, for the initial 30 seconds of spreading.

Figure 3.11 - Spreading diameter by the mini-slump method, for pastes 3, 5 and 11.

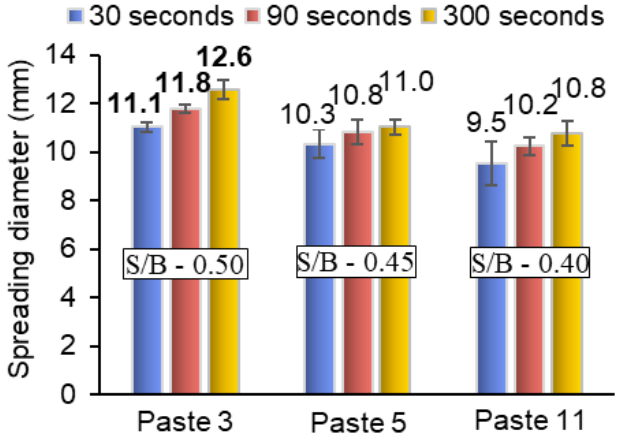

Source: elaborated by the author

Hadi et al. (2019) produced pastes based on FA and blast furnace slag with activator/precursor ratios of 0.5, obtaining average spread values of 16.6 cm (after 15 minutes). For the current research, the spreading diameter was measured for 5 minutes obtaining the highest value of 12.6 cm, for paste 3. According to the studies of Tan, Bernal and Provis (2021), the yield stress value of geopolymer pastes can be obtained from the mini-slump test. This is done using Equation 3.1, reproduced below.

$$\tau_0 = 225\rho g\Omega^2/128\,\pi^2 R^5 \quad (3.1)$$

Where, τ_0: yield stress; ρ: paste density; g: gravity acceleration (9.81 m/s^2); Ω: mini-slump volume; R: spread diameter.

Following the referred authors' recommendations and using Equation 3.1, the values found for yield stress were 17.1 Pa, 34.1 Pa and 37.2 Pa for Pastes 3, 5 and 11, respectively. Paste 3 was the one that presented the lowest values of yield stress. AAB pastes present values of about 0 to 75 Pa (TAN; BERNAL; PROVIS, 2021).

The results of paste compressive strength at early ages (7 days) are shown in Figure 3.12. Paste 5 presented the highest compressive strength at an early age, for ambient curing. This is attributed to the high content of soluble silica available in the activator solution, with a silica modulus of 1.25 (LEE et al., 2020).

Figure 3.12 - Compressive strength of AABs pastes 3, 5 e 11
(a)7 days, (b) 28 days

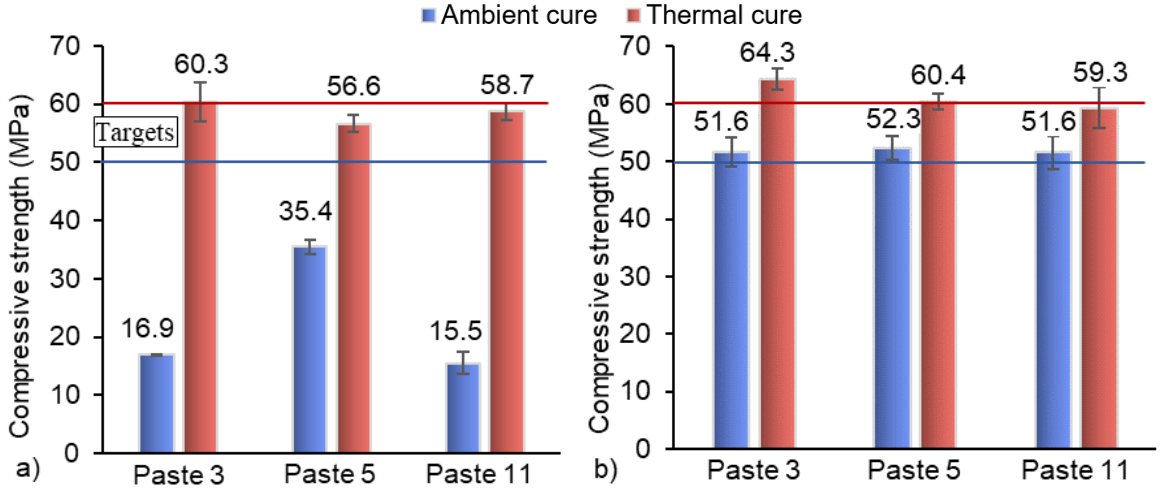

Source: elaborated by the author

The thermal curing results presented values with no significant increases from 7 days to 28 days, while ambient curing showed, at 7 days, around 33% of the strength at 28 days, except for Paste 5, which showed two-thirds of the strength at 28 days. Paste 3 with N/B of 10%, S/N of 0.75, and FA-SS equal to 75-25 demonstrated better performance on mini-slump, followed by a higher setting time. In such a manner, it was selected for application in concrete.

3.4.1.3 Additional analysis of the effect of the curing process for the AAB paste applied to concrete

In order to assess the strength increase with age and curing process influence (at 3, 7, 14, 28, 56, and 112 days), specimens of the chosen formulation (paste 3) were replicated. The results are presented in Figure 3.13.

Figure 3.13 - Compressive strength over time of AAB paste 3

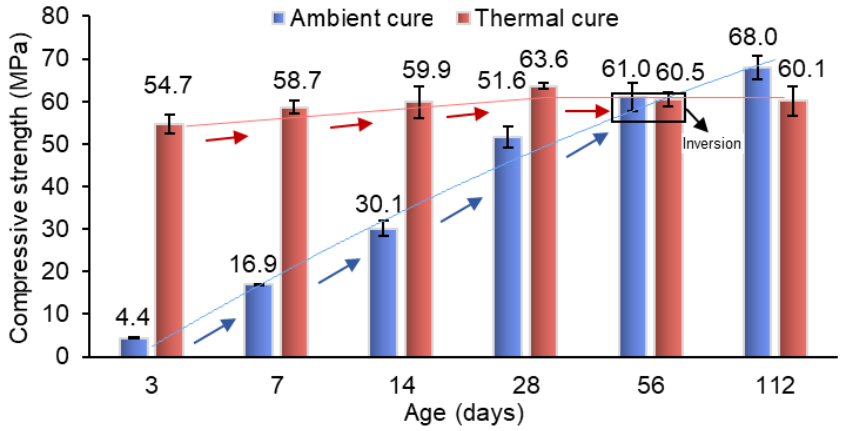

Source: elaborated by the author

Thermal curing provides high initial strength for AABs (PROVIS; VAN DEVENTER, 2013). Concerning thermal curing, it showed a huge increase for 1-day curing (86% of maximum strength) with some smaller, and not significant, strength increase in other ages, achieving compressive strength of 63.6 MPa at 28 days. After that, it was observed a decrease in the measured strength, with 60.1 MPa at 112 days. Such reduction may be associated with the gels' changes of amorphous characteristics in the microstructure of greater organization or in crystalline zeolitic structures, which causes microstructure change and internal tensions (MA et al., 2016) or they can be little strength variations attributed to the production process. Thermal curing provided less variation in strength values over time, providing stable results.

That analysis is recommended by the literature due to the sense that thermal curing imposes a higher strength for the composite in initial ages. However, ambient curing can favor an increasing strength (LEE et al., 2019) in the long term in such a way that, at higher ages, the strength of ambient-cured specimens can surpass those of thermal cured specimens (SOUTSOS et al., 2016). As seen in Figure 3.13, the ambient curing process presented a strength increase at early ages. However, after 56 days the ambient reading surpassed the thermal curing with 61 MPa, achieving 68 MPa at 112 days, opposing the results of the literature (XIE et al., 2020; YUSUF et al., 2014; ZHANG et al., 2020).

3.4.1.4 Microstructural analysis

Figure 3.14 shows the aspect in the AAB paste microstructure. The paste presented particles of ash and slag partially reacted. Moreover, the paste presented voids, associated with water released during the step of condensation of the gels, which is totally or partially removed during the curing process (LLOYD et al., 2009).

Figure 3.14 - SEM/EDS aspect of gels formed by AAB paste 3

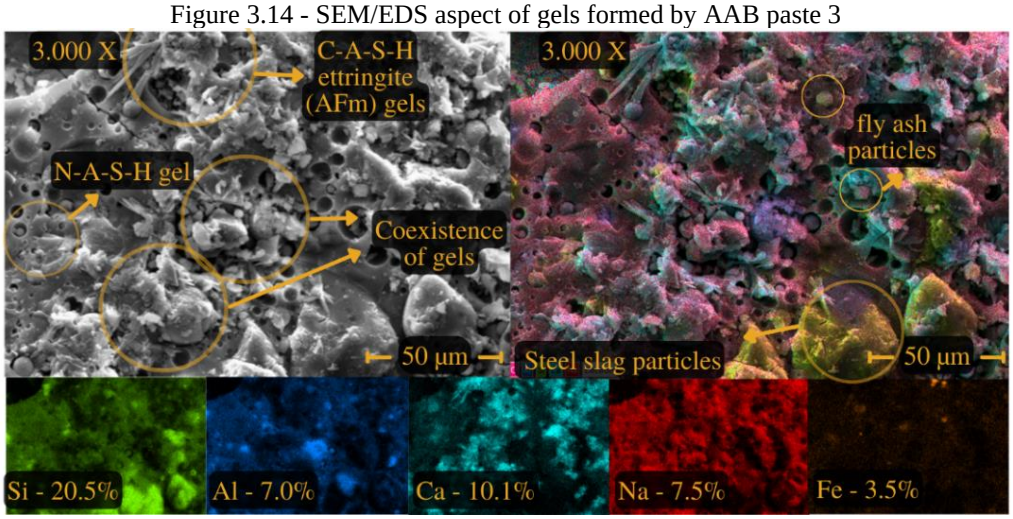

Source: elaborated by the author

Figure 3.14 showed areas with the higher calcium content. In addition, the structures formed showed a similar appearance to C-A-S-H type gels and ettringite (AFm) (GARCÍA-LODEIRO et al., 2011; ZHU et al., 2021). The areas with higher sodium content (in red) and lower calcium content, may indicate the formation of N-A-S-H type gels (PROVIS; VAN DEVENTER, 2013; NATH; SARKER, 2014), while the areas with high calcium and sodium content, may indicate the coexistence of C-A-S-H and N-A-S-H gels. Dense and homogeneous microstructure, provided by the appropriate coexistence of the products of alkali activation, presents higher resistance to chemical attack (ZHANG et al., 2017, BERNAL; PROVIS, 2014), high performance for compressive strength at high temperatures (ZHANG et al., 2020), and lower porosity (BERNAL; PROVIS, 2014; PROVIS; BERNAL 2014).

3.4.2 Alkali-activated concrete

3.4.2.1 Self-compacting results in the fresh state

The paste content of 38.2% (void content plus 20% of adjustment, considered necessary during the concrete mix design) exceeded the slump value of 270 mm and had its self-compacting properties measured in the fresh state. The slump flow results were 575 ± 17 mm and the T50 results were achieved with 13.8 ± 1.3 seconds. This would allow classifying

the material as VS2 and SF1 (EFNARC, 2005; NBR 15,823-1, 2017; NBR 15,823-1, 2017) if classical Portland cement self-compacting characterization were considered. In addition, the material showed Visual Stability Index values equal to zero, with no evidence of segregation or bleeding (ASTM 1,611, 2010). The absence of bleeding is associated with the high viscosity of the activators.

3.4.2.2 Compressive strength and Young´s modulus results

The design of AAB concrete adopted Paste 3, which presented adequate fresh and hardened states. The composed AAB concrete (AAC) presented results for physical characterization having an apparent density of 2,305.6 kg/m³ and porosity of 9.4% **(**NBR 9,778,2012; ASTM C642). The compressive strengths of the AAC are presented in Figure 3.15, for 7, 14, and 28 days, in both curing processes.

Figure 3.15 - Compressive strength of AAB concretes at 28 days

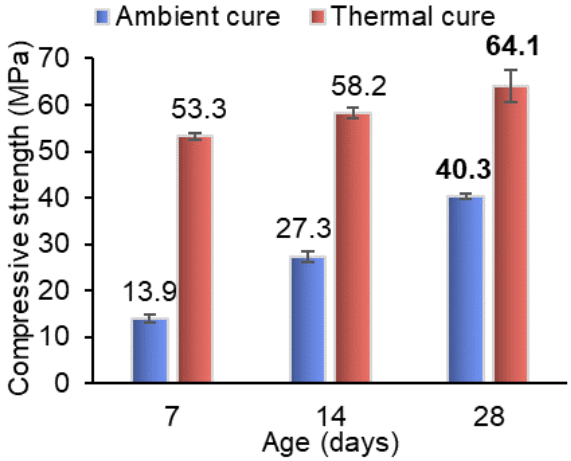

Source: elaborated by the author

As seen, the thermal cure kept the high strength behavior at early ages, with no significant increases over time, ranging from 53.3 MPa (7 days) to 64.1 MPa (28 days). For 28 days, the specimens under thermal curing showed strength values similar to the paste (Paste 3) under the same conditions. The same concrete with ambient curing showed a 10 MPa reduction in compressive strength when compared to the paste under the same curing condition, which is expected due possibly to interfacial transition zones (LUO et al., 2021; FAROOQ, 2021). This may be associated with a positive effect of thermal curing at the interface between the binder and the aggregates. The AAB concretes showed compressive strength values higher than the results presented by the literature on AAB self-compacting concretes, reporting values up to 48 MPa (SAINI; VATTIPALLI, 2020, HUSEIEN; SAM; ALYOUSEF, 2021).

The average values of Young´s modulus were 20.2 GPa under ambient curing and 26.2 GPa under thermal curing. Such results are considered lower than those compared to typical conventional Portland cement concretes, with similar aggregates and compressive strengths. This behavior is in accordance with the literature, which usually reports low Young's modulus results for AAB concretes, despite its high results for compressive strength (NATH; SARKER, 2017). Although the aggregate type affects the values of Young´s modulus, these values can also be impacted based on the types and proportions of gels formed during alkali activation, especially the N-A-S-H and C-A-S-H gels. In the literature, it is observed that low calcium AABs presented low Young´s modulus values, between 15 GPa and 18 GPa (NĚMEČEK, ŠMILAUER; KOPECKÝ, 2011). On the other hand, high calcium oxide AABs, based on precursors such as slags, tend to exhibit higher Young´s modulus values ranging from 12 GPa to 47 GPa, which is highly associated with C-A-S-H gels content, similar to those formed by Portland cement hydration (NĚMEČEK; ŠMILAUER; KOPECKÝ, 2011; DING; SHI; LI, 2018).

Waqas et al. (2021) found Young´s modulus results from 14.5 GPa to 31.2 GPa, for AAB based on fly ash and slag. The Young's Modulus values increased with the increment of the slag content, consequently, a high calcium oxide content. ABBs produced with higher calcium contents present similar gels to those produced in Portland cement binders, which have higher Young's modulus values. Ding et al. (2018) obtained results of 22.7 GPa and 27.4 GPa for AAB based on fly ash (50%) and slag (50%), results lower than those found for Portland cement binders of the same strength. The values found by the authors, using analogous materials, were similar to those of the present research. These results are attributed to the employed material and are characteristic of the coexistence of the alkali-activation gels obtained from precursors with different calcium oxide content.

3.5 Conclusions

In this paper, a mix design method for alkali-activated binders and concretes was proposed, based on the design of silica modulus, alkali content, binary precursors proportions, and curing process, being tested and applied in the production of pastes and concretes. The idea was to contribute to alkali-activated binder (AAB) pastes mix design methods considering the fresh state and the hardened state properties, aiming at concretes with adequate consistency, setting time and high workability, respecting a target mechanical strength. The method was proven to be efficient in achieving the expected strength, and obtaining an application in high

compressive strength (higher than 60 MPa) and high workability concrete (slump flow of 575 mm). The pastes were evaluated with respect to compressive strength, mini-slump and setting times, whereas one of them was chosen as ideal for concrete preparation. The concrete was evaluated with respect to compressive strength, Young's modulus and self-compacting concrete parameters (slump flow). Based on the results, the main conclusions were:

- The lower silica modulus (S/N) parameters values of the alkaline activators (0.75) and lower fly ash (FA) content (FA-SS of 75-25) performed better compressive strength results concerning the AABs pastes;
- Thermal curing tends to increase the compressive strength of the pastes at least initially, but this is not the case for all combinations, particularly for high S/N parameters (1.75);
- The AAB pastes' compressive strength produced under ambient curing can overcome the resistance of thermally cured binders over time, despite the increase in strength for early ages (lower than 28 days);
- The pastes mix design based on (i) the alkali content, (ii) silica modulus, and (iii) the precursor proportions presented good performances for the binders produced based on the desired compressive strength and the further fresh state analysis (the high fluidity desired);
- The binder content estimation, based on the aggregate packing analysis and its voids content was proven to be feasible for the AAB concretes application, obtaining the desired workability, concerning its fresh state properties, while keeping the high compressive strength;
- The thermal curing process proved to have a positive impact on concrete compressive strength results at the assessed age, 28 days, also being feasible to estimate a high strength behavior at early ages (1 day) based on the behavior of the chosen paste applied to the concrete;
- The AAB concretes presented a lower Young´s modulus than typically obtained for traditional Portland cement concretes with similar aggregates, as previous literature suggests.

It is expected that those contributions will add up to practical formulations for alkali-activated binders and concretes, as well as other similar composites, contributing to the production of feasible sustainable binders, to support future actions for the management of

industrial wastes (fly ash and steel slag) and their destination and gradual Portland cement replacement (the major GHG pollutant component of cementitious composites). The designed materials seem particularly applicable for precast concrete, due to its more controlled casting conditions (materials control, mix and curing methods) compared to conventional casting in situ.

4 RHEOLOGICAL EVALUATION OF HIGH-STRENGTH SELF-COMPACTING ALKALI-ACTIVATED MATERIALS PRODUCED WITH FLY ASH AND STEEL SLAG

Abstract

This study aims to evaluate the effect of the composition and mixing method of alkali-activated binder (AAB) pastes and concretes (produced with fly ash (FA) and steel slag (SS) activated by sodium silicate and sodium hydroxide) on their rheology. It also investigates the effect of the mixing method on the performance of AAB self-compacting concretes at the hardened state. For the AAB pastes, oscillatory and flow tests were performed to evaluate parameters of apparent viscosity, yield stress, G', G" and phase angle. For the AAB concretes, traditional parameters from self-compacting concrete classification, and also mixing energy, maximum torque, and apparent viscosity from a rheological evaluation were investigated. As result, it was observed that the pseudoplastic rheological model described the behavior of alkali-activated materials, both pastes and concretes. The evaluated pastes presented flow consistency index between 1.896-24.405 Pa.s^n, flow behavior index between 0.814 and 0.968 and G" values higher than G' for the measured range, behavior with a viscous tendency. From the rheological evaluation, it was observed that lower silica modulus, higher alkali contents and lower SS are adequate for the rheological performance, targeting the lowest apparent viscosities possible, which would be adequate for self-compacting concretes production. AAB concretes exhibit a high passing ability and high flow time, which was also influenced by the mixing process. Rheological analysis showed that AAB concretes presented higher mixing energy and apparent viscosity than expected for typical Portland cement concretes. As for the mechanical performance, AAB concretes presented compressive strength up to 77.1 MPa and thermal curing increased compressive strength by almost 60% at 28 days. The results showed that the composition parameters of precursors and activator influence the apparent viscosity of AAB pastes and that mixing procedures with more energy allows obtaining more resistant materials in the hardened state. These findings contribute towards an improved comprehension of the behavior of AAB materials, and consequently, hold the potential to facilitate their utilization in forthcoming applications.

Keywords: Alkali-activated materials, rheology, self-compacting concrete, fly ash, steel slag.

Highlights

- AAB pastes and concretes based on fly ash and steel slag could be well represented as pseudoplastic fluids in the fresh state.
- Composition parameters of precursors and activators highly influence the apparent viscosity of AAB pastes.
- AAB concretes exhibit higher mixing energy and apparent viscosity than conventional concretes.
- AAB concretes exhibit high passing ability and high flow time.
- The mixing methodology influences the flow time and the compressive strength of AAB concrete.
- Mixing procedures with more energy allowed to obtain more resistant materials in the hardened state, after a less fluid behavior in the fresh state.

4.1 Introduction

Civil construction is a sector with a high environmental impact, both in waste generation and in the consumption of energy and natural reserves (TRINDADE et al., 2020). Portland cement employed in conventional concretes is responsible for 5% to 7% of the world's CO_2 production (BENHELAL et al., 2012; SINGH; MIDDENDORF, 2019). In this scenario, studies have been developed to replace conventional concrete components partially or totally by products with lower environmental impact (SINGH; MIDDENDORF, 2019; PROVIS; VAN DEVENTER, 2019). Alkali-activated binders (AABs) emerge as an alternative to Portland cement production with the potential to reduce CO_2 emissions (SUMESH et al., 2017). AABs are materials obtained from the alkaline activation of an aluminosilicate precursor combined with a highly concentrated alkaline solution (PROVIS; VAN DEVENTER, 2019; ZERZOURI et al., 2021).

The precursors with more consolidated studies are fly ash (FA), ground granulated blast furnace slag (GGBFS) and metakaolin (PROVIS; VAN DEVENTER, 2019; XIE et al., 2020). However, there are still some precursors that are barely explored and with insufficient viable applications to facilitate better by-products management. Among them, steel slag (SS) can be underlined (NUNES; BORGES, 2021), which can be obtained by the Basic Oxygen Furnace (BOF) and Electric Arc Furnace (EAF) processes. The world production of crude steel is 1.95 billion tons (WSA, 2022). Each ton of this production generates approximately 600 kg of steel waste and co-products (HORII et al., 2015).

Besides lower CO_2 emissions, the use of AABs in concretes may outperform Portland cement concrete (PCC) in mechanical strength (SINGH; MIDDENDORF, 2019; XIE et al., 2020) and durability indications (BERNAL; PROVIS, 2014; LI; THOMAS; PEETHAMPARAN, 2019). Nevertheless, practical applications of AAB concretes in the construction industry are still limited (ALNAHHAL; KIM; HAJIMOHAMMADI, 2021). One of the main obstacles to the industrial use of these materials is not to achieve similar strengths to those of PCCs, but to maintain similar rheological characteristics avoiding impacts on the construction methods used (XIE; KAYALI, 2016; XIE et al., 2020). Recent studies have attempted to evaluate and control the rheological behavior of AAB concretes from mixing to setting, to improve performance in the fresh state and maintain mechanical properties (FAVIER et al., 2014).

Different shear rates are applied to the material during mixing, pumping and densification processes, which produce rheological responses affected by the chemical

composition of the precursor and alkali activator, dissolution kinetics of the precursor, amount of free water, specific surface area of the precursors and presence of calcium and magnesium in the precursors (PALACIOS; BANFILL; PUERTAS, 2008; MEHDIZADEH; KANI, 2018; PROVIS; VAN DEVENTER, 2019; FAVIER et al., 2013; ALNAHHAL; KIM, 2020). Therefore, understanding the flow and apparent viscosity parameters is highly important for correlating these properties with the workability/fluidity of the material (KIM; NOEMI; SHAH, 2012). In addition, the rheological study can contribute to the understanding of the effect of the alkali activation process on the rheological parameters (XIE; KAYALI, 2016; RIFAAI et al., 2019). Although some studies have evaluated the mechanical behavior of AABs (SOUTSOS et al., 2016; CRISTELO et al., 2019), only a few research works have attempted to relate this property to the rheological response of the material, especially for precursors such as SS (XIE; KAYALI, 2016; MA et al., 2022).

Materials can be classified according to their rheological response over time (SCHRAMM, 2006; IRGENS, 2014). Rheometers (Figure 4.1) are used to investigate the rheological behavior of alkali-activated materials based on the application of dynamic or oscillatory shear cycles (YUAN et al., 2017). Dynamic shear tests allow for determining a rheological model that better describes the material behavior, resulting in apparent viscosity and yield stress parameters (ROUSSEL 2011; ALNAHHAL; KIM; HAJIMOHAMMADI, 2021). The rheological models most used in the alkali-activated literature are Bingham and Hershel-Bulkley models (PUERTAS; VARGA; ALONSO, 2014; DAI et al., 2020; LU et al., 2021). On the other hand, small amplitude oscillatory tests allow an understanding of the rheological changes produced by the alkali-activation process (ALNAHHAL; KIM; HAJIMOHAMMADI, 2021). In this kind of test, where internal structure is less modified by flow due to limited strains, materials are usually considered viscoelastic. Then, storage modulus (G'), loss modulus (G") and phase angle ($\tan^{-1}$[G"/G’]) parameters are analyzed (YUAN et al., 2017; IRGENS, 2014).

Figure 4.1 - Rheology tests photographs on
(a) AAB pastes, (b) AAB concretes

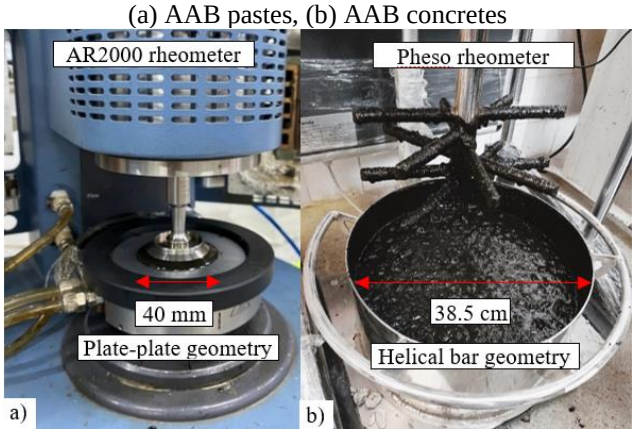

Source: elaborated by the author

Considering the aforementioned motivations, this study aims to evaluate the effect of different formulations of AAB pastes, with similar compressive strength (from 50 MPa for curing at 25 °C to 60 MPa for curing at 65 °C), based on coal fly ash and BOF-type steel slag activated by sodium silicate and sodium hydroxide, on their rheological classification. In addition, it aims to evaluate the effect of the mixing method on the rheological classification and performance of AAB self-compacting concretes. The effects of different compositions of precursors and activators on the apparent viscosity and yield stress observed in flow tests and mixing energy tests on AAB pastes were investigated. In addition, viscoelastic parameters including G', G" and phase angle observed in oscillatory tests were determined to evaluate how the alkali activation process affects the material's rheological behavior over time. The setting time and the microstructure were also evaluated. The best performing paste in terms of lowest apparent viscosities was applied to an AAB concrete, which had its rheological and mechanical behavior characterized and compared to a typical Portland cement concrete under different mixing processes (either free fall mixer or planetary mixer). In the rheological characterization in the fresh state, mixing energy, maximum torque and apparent viscosity parameters of the concretes were evaluated, and complementary tests of flow time, slump flow and J-ring were performed. In the hardened state, compressive strength was evaluated.

4.2 Materials and mix design

4.2.1. Materials

Two different precursors were used to produce the AAB pastes. The investigated fly ash (FA) was produced by a thermoelectric power plant and is categorized in Class F according to ASTM C618 (2019). The investigated steel slag (SS) was produced by a steel

company using the Basic Oxygen Furnace process. Table 4.1 summarizes the oxide chemical compositions of the constituent materials used in this study. The specific gravities of FA and SS are 2.34 and 3.13, respectively. The particle size distribution of the precursors is presented in Figure 4.2. The average particle sizes of FA and SS were 5.6 μm and 35.4 μm, respectively. The specific surface area values were 4790 cm²/g for FA and 3360 cm²/g for SS. Particle size distribution and specific surface area influence the water demand of the mixture and the kinetics of reactions (SOUTSOS et al., 2016), which can affect the rheological and mechanical performance of the material.

Table 4.1 - Chemical composition of the investigated steel slag (SS) and fly ash (FA)

Materials	**Al_2O_3**	**SiO_2**	P_2O_5	SO_3	Cl	K_2O	**CaO**	TiO_2	MnO	**Fe_2O_3**
Steel slag (%m.)	**1.94**	**5.64**	0.84	0.83	0.04	0.14	**53.14**	-	2.97	**34.40**
Fly ash (%m.)	**11.14**	**42.17**	0.53	1.08	0.06	3.97	**10.25**	2.74	0.27	**26.98**

Source: research data

Figure 4.2 - The particle size distribution of the investigated precursors

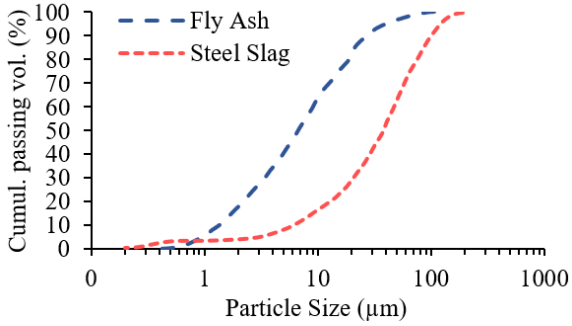

Source: elaborated by the author

A blend of solutions of sodium hydroxide (NaOH) and sodium silicate (Na_2SiO_3) was used. Those are the most studied activators in the literature on AABs (VAN DEVENTER, 2019; XIE et al., 2020). The 10 mol/L sodium hydroxide solution (YUSUF et al., 2014; RAFEET et al., 2017) was composed by a mass of 31.3% NaOH and 68.7% H_2O. The commercial sodium silicate solution was composed by a mass of 14.98% Na_2O, 31.83% SiO_2 and 53.19% H_2O.

Silica sand and granitic gravel were used as aggregate for the AAB concrete. The particle size distributions of the aggregates are presented in Figure 4.3. The fine aggregate used had a specific gravity of 2.573, a bulk density of 1470.5 kg/dm³ and a fineness modulus of 2.66. The coarse aggregates used presented specific gravity of 2.617 and 2.629 and bulk density of 1406.7 kg/dm³ and 1487.2 kg/dm³, for coarse aggregate 4.75-12.50 mm (1) and 9.5-25 mm (2), respectively.

Figure 4.3 - The particle size distribution of the investigated aggregates

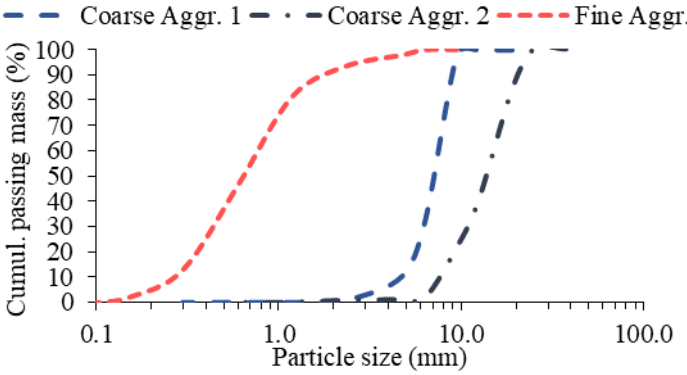

Source: elaborated by the author

4.2.2. Mix Design of Alkali-Activated Binder (AAB) pastes and concretes

According to the literature, the best compressive strengths of AAB pastes based on FA and SS were obtained with silica modulus (S/N) dosages between 0.5 and 2.5 (SOUTSMAOS et al., 2016, THOMAS; PEETHAMPARAN, 2017; DING; SHI; LI, 2018) and alkali content (N/B) between 4% and 15% (LI 2018; SOUTSOS et al., 2016). Based on this, Araujo (2023) developed a mix design procedure for AAB pastes based on FA and SS with two types of cure: ambient, also known as room, (25 °C to 30 °C) and thermal (65 °C) (YUSUF et al., 2014; SOUTSOS et al., 2016). For the mix design, the main aspect considered was the minimum compressive strength of 50 MPa under ambient curing and 60 MPa under thermal curing. 18 pastes were evaluated in the study by Araujo et al. (2023). 3 different formulations with no statistically consistent difference in compressive strength showed greater potential for application in concrete. They were selected for evaluating the impact of different formulations presented in Table 4.2, in the rheology of the material, evaluated by flow and oscillatory tests.

Table 4.2 - Mix proportions of AAB pastes

Paste ID	Mix parameters	NaOH Solution (kg/m³)	Na_2SiO_3 Solution (kg/m³)	Fly Ash (kg/m³)	Steel Slag (kg/m³)	Liq./bind.
M1	S/N 0.75; N/B 10.0; FA-SS (% mass) 75-25	353.4	312.1	993.5	331.2	0.5
M2	S/N 1.25; N/B 8.0; FA-SS (% mass) 75-25	192.8	445.9	1064.5	354.8	0.45
M3	S/N 0.75; N/B 8.0; FA-SS (% mass) 50-50	324.8	286.9	760.9	760.9	0.4

Source: research data

The AAB concrete formulation was produced from the AAB paste that presented the lowest apparent viscosity for application in concrete. The M1 paste was selected, composed by S/N of 0.75, N/B of 10% and precursors with 75% FA and 25% SS by mass.

For the AAB concrete, FA and SS were activated with the solution composed of 57.7% sodium hydroxide solution and 42,3% sodium silicate (by mass), associated with sand and gravel, as aggregates. The proportion of aggregates of different sources was determined using two methods to minimize voids content within aggregates: (i) experimental aggregate packing curves were obtained in the laboratory for different aggregate compositions; and (ii) theoretical packing curves were also obtained with the assistance of the software EMMA Mix Analyzer, version 3.5.2.11, which uses the modified Andreasen model, to perform the aggregate packing. Both methodologies indicated the same ideal material ratios for obtaining the least voids in the aggregate structure. A similar procedure was adopted by Bondar et al. (2019).

The final mass proportions were 35% sand to 65% coarse aggregate (26% coarse aggregate 1 and 39% coarse aggregate 2). After that, using that aggregate composition, different paste contents were tested to obtain self-compacting concrete. The ideal paste content found was 38.4%. This value is in the same order as those from studies by Bernal et al. (2011) (between 24.1% and 40.2%). The design of the produced AAB concrete is shown in Table 4.3.

Table 4.3 - Mix proportions of AAB concrete

NaOH Solution 10 mol/L	Na_2SiO_3 Solution 15.0% Na_2O, 31.8% SiO_2	Fly Ash	Steel Slag	Fine aggr.	Coarse aggr. 1	Coarse aggr. 2	Unit.
135.9	120.1	382.1	127.4	561.6	417.2	625.8	kg/m³
10.4	7.6	16.3	4.1	21.8	16.0	23.8	% vol.

Source: research data

To compare the rheological behavior of the AAB concrete with typical Portland cement concretes, materials with 30 MPa (PCC30) and 50 MPa (PCC50) of compressive strength were produced. The material consumption to produce concretes in kg/m^3 was 317: 779: 283: 728: 203.2 for PCC30 and 518: 586: 285: 734: 207.7 for PCC50 (cement: fine agg.: coarse agg. 1: coarse agg. 2: water), both with 1.3% (with respect to the mass of cement) of a Sikament®-370 RM superplasticizer.

4.2.3 Mixing procedure of AAB pastes and concretes

The AAB pastes were prepared as follows: (i) 1-minute of pre-homogenization; (ii) 1.5 minute of mixing at 62 ± 5 RPM (low speed); (iii) 1-minute pause to check homogeneity; (iv) 1.5 minute of mixing at 62 ± 5 RPM. They were prepared in a planetary mixer of 6 liters capacity.

The production methodology of the AAB concretes was performed either in the free-fall concrete mixer or in the Pheso rheometer, a planetary mixer. This was done to analyze the effect of the mixing energy on the empirical properties for the classification of self-

compacting concretes and compressive strength. The planetary mixer provides the highest shear and therefore the highest mixing efficiency, which affects the material's performance in the fresh and hardened state. The mixing procedure by the free fall mixer was performed as follows: (i) 1-minute mixing of coarse aggregates with 10% activator solution; (ii) addition of homogenized precursors and 80% activator solution and mixing for 4 minutes; (iii) addition of fine aggregates and mixing for 4 minutes; (iv) addition of the remaining 10% activator solution and mixing for 2 minutes. The mixing procedure in the planetary mixer is described in topic 3.2, because rheological testing is performed during the mixing procedure itself, which corresponds to planetary mixing. The referred procedure includes first homogenizing the mortar and then adding coarse aggregates to produce concrete. The same procedure is done both for AAB concretes and for PCCs. Three specimens of each concrete were molded in cylindrical PVC molds with 10 cm diameter and 20 cm height for mechanical evaluation using the two investigated curing processes: thermal and ambient (for AAB concrete). The thermal curing occurred for 24 hours, in an aerated oven, at a temperature of 65 °C. The ambient curing was performed at temperatures between 25 °C and 30 °C, and humidity of about 65% to 85%.

4.3 Experimental methods

4.3.1 Setting time

The setting time of AAB pastes was measured with the Vicat apparatus (ASTM C191, 2021; NBR 16,607, 2018) to assist in the discussion of viscoelastic parameters obtained afterward in the flow and oscillatory tests with a rheometer.

4.3.2 Rheological tests

Two of the main parameters for the rheological evaluation of fluid are apparent viscosity and yield stress (SCHRAMM, 2006; IRGENS, 2014) When the apparent viscosity does not change under different shear rates, and the yield stress is zero, the material is classified as Newtonian. However, when the material presents different apparent viscosities as a function of the shear rate and/or the applied shear stress, this material is classified as non-Newtonian (SCHRAMM, 2006; IRGENS, 2014). Previous results indicate that this is usually the case for AAB pastes (GÜLLÜ et al., 2019).

The two most common models to describe non-Newtonian cementitious materials are the Bingham model and the Herschel-Bulkley model. Bingham fluids behave like a solid

up to a yield stress (τ_0) and from there, they present proportionality between increments of shear stress and shear rate, according to Equation 4.1. The proportionality constant between the increments is called plastic viscosity ($n_p=d\tau/d\dot{\gamma}$). If this proportionality is not sufficient to represent material behavior, it is usual to adopt the Herschel-Bulkley model, represented by Equation 4.2, which simplifies to the pseudoplastic (n < 1) or the dilatant (n > 1) models, when $\tau_0 = 0$ (SCHRAMM, 2006).

$$\tau(\dot{\gamma}) = \tau_0 + n_p \dot{\gamma} \quad (4.1)$$

$$\tau(\dot{\gamma}) = \tau_0 + K\dot{\gamma}^n \quad (4.2)$$

Where, $\tau(\dot{\gamma})$: shear stress (Pa); τ_0: yield stress (Pa); n_p: plastic viscosity (Pa.s); $\dot{\gamma}$: shear rate (1/s); K: flow consistency index (Pa.s^n); n: flow behavior index (DN).

4.3.2.1 Alkali-activated binder (AAB) pastes

The rheological behavior of AAB pastes was characterized by flow tests and oscillatory tests, all performed at 25 °C using a TA Instruments AR2000 rheometer, with plate-plate geometry of 40 mm diameter and 1 mm gap. The applied gap was 5 times higher than the maximum diameter of the precursors (KISSA, 2017).

The flow test consisted of the following steps: (i) 100 s^{-1} pre-shearing for 2 minutes; and (ii) and 4 cycles of 2 minutes of acceleration and 2 minutes of deceleration, with the rate at each step from 0 s^{-1} to 100 s^{-1} (Figure 4.4), like the one adopted by Revathi and Jeyalakshmi (2021), for ABB pastes based on fly ash and steel slag. The test was performed after 10 minutes and after 60 minutes of the contact between activators and precursors. This was done to evaluate how the alkali-activation reactions interfere with the properties of yield stress, apparent viscosity, flow consistency index, flow behavior index, thixotropy and rheopexy.

Figure 4.4 - Schematical representation for the rheological tests procedure on AAB pastes

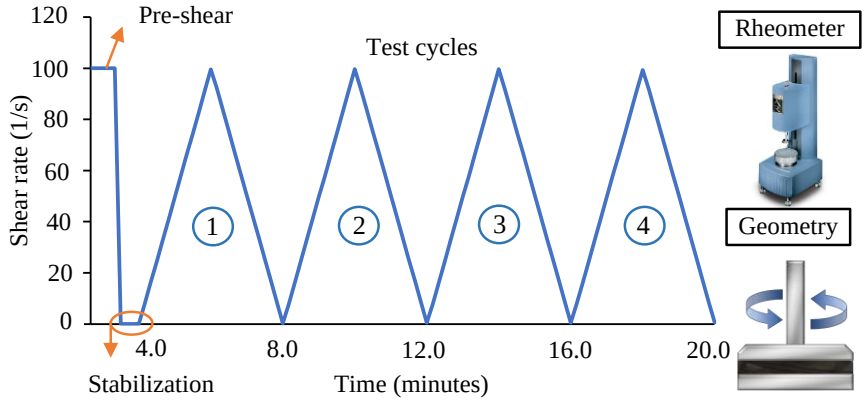

Source: elaborated by the author

Oscillatory tests are recommended to evaluate how the kinetics of alkali activation reactions influence the rheological behavior of the material over time without breaking its microstructure, by applying small deformations within a linear viscoelastic zone of the material (DAI et al., 2020; ALNAHHAL; KIM; HAJIMOHAMMADI, 2021). First, testing different deformations allows determine up to which deformation (corresponding to a critical strain) the material behaves linearly. Then, in that range, the test consists of the application of constant sinusoidal torsion deformation on a specimen inducing a sinusoidal torque response in a permanent regime called time sweep. The measurements are used to calculate stress and strain (calculated at the outer radius of the specimen) signals through time, which are both, in the linear viscoelastic range, sinusoidal. For each cycle, the phase angle (δ) obtained in this test measures the time offset (phase difference) between stress and strain signals. Also, the absolute value of complex modulus ($|G^*|$) corresponds to the ratio between stress and strain amplitudes. Then, it is possible to calculate the two components of the complex modulus (G^*): the storage modulus $(G)=|G^*|.\cos(\delta)$, and the loss modulus $(G")=|G^*|.\text{sen}(\delta)$ (IRGENS, 2014; YUAN et al., 2017). The curves plotted as functions of time (at a constant frequency) were the results of a moving average of 10 measurements. It is important to notice that δ is a measurement that relates to the viscoelastic behavior of a material in such a way that for perfectly elastic materials its value is 0^o, while for perfectly Newtonian fluids its value is 90^o. Results for viscoelastic materials are between these two values (BETIOLI, 2007; YUAN et al., 2017).

To assist in the analysis of the oscillatory test results, the classification into 4 stages as suggested by Alnahhal, Kim, and Hajimohammadi (2021) was adopted. By investigating the viscoelastic behavior over time, the authors proposed 4 stages: (I) characterized by the dominance of the viscous portion (liquid state behavior) of the paste above the elastic portion (solid state behavior); (II) characterized by the formation of a weak elastic network, with a moderate increase in complex modulus; (III) characterized by a partial dissipation of the stored energy and it is called the transient period, where the phase angle increases; (IV) characterized by hardening, resulting from the progressive process of alkali-activation (ALNAHHAL; KIM; HAJIMOHAMMADI, 2021). The determination of the critical strain, applied in the time sweep test, is performed using a strain sweep until a variation in the complex modulus measurement by 10% can be noticed (BETIOLI, 2007; RIFAAI et al., 2019). The strain sweep test was performed by varying the strain amplitude from 0.001% to 10% with a frequency of 1 Hz, like that adopted by Alnahhal, Kim and Hajimohammadi (2021). Based on the strain sweep results, the strain amplitude chosen for oscillatory tests was 0.5%. The duration chosen for the

oscillatory test was set to two hours, to avoid equipment damage, due to the setting time of the material. The procedures for the strain sweep and time sweep tests are shown in Figure 4.5.

Figure 4.5 - Procedure for the oscillatory rheological test of AAB pastes

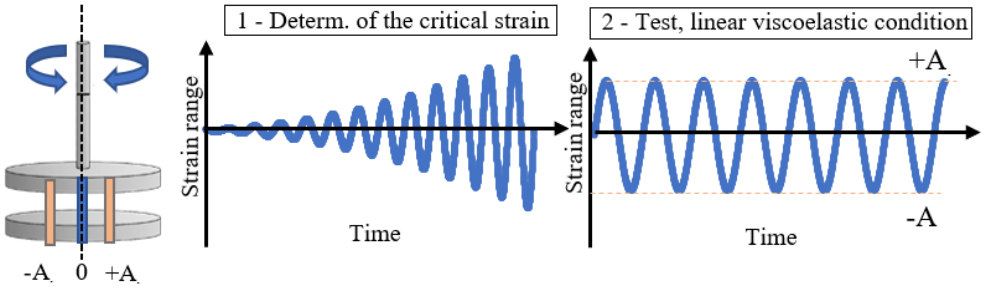

Source: elaborated by the author

4.3.2.2 AAB concrete

The rheological behavior of AAB concrete was characterized by multipoint tests composed of mixing and shear cycles performed with the Pheso planetary rheometer. The equipment is composed of a metallic bowl and a geometry of six double fins (16 mm diameter and 13 cm length) disposed of helical arrangement. The rheology tests performed are divided into two stages: the mortar stage, obtained by mixing activators, precursors and fine aggregates, and the concrete stage, where the coarse aggregates are added to the previously produced mortar. In these stages, alkali-activated mortars, and concretes, abbreviated as AAM and AAC, and Portland cement mortars and concretes, abbreviated as PCM and PCC, were analyzed.

The rheological multipoint test was performed with 14 L of material and was divided into two stages: (i) one for testing the mortar; and (ii) one for testing the concrete, after incorporating the coarse aggregate. The complete procedure is schematically represented in Figure 4.6. The mortar stage was composed by: (i) mixing of precursors and fine aggregates at 125 RPM for 4 minutes; (ii) addition of 90% of the activator solution and mixing cycle at 125 RPM for 8 minutes; (iii) pause for scraping the rheometer walls for 1 minute; (iv) mixing cycle of 125 RPM for 3.5 minutes; (v) shear cycle with gradual acceleration and deceleration between 6 RPM and 250 RPM during 2 minutes. The concrete stage was composed of: (i) addition of coarse aggregates and 10% of the activator solution; (ii) mixing at 125 RPM for 5.5 minutes; (iii) shear cycle with gradual acceleration and deceleration between 6 RPM and 190 RPM during 1.8 minute. From the measured results (torque and rotation speed through testing time), parameters related to maximum torque (value obtained during the mixing process which represents the turning point), stabilization torque (torque value obtained when the material is completely mixed), mixing energy (Torque vs. time graph area, until the stabilizing torque is

reached) and apparent viscosity (torque to rotation speed ratio) are determined. During the test run, 10 measurements are obtained per second. The results obtained were smoothed by a moving average of 100 measurements.

Figure 4.6 - Schematical representation for the rheological tests procedure on AAB concretes

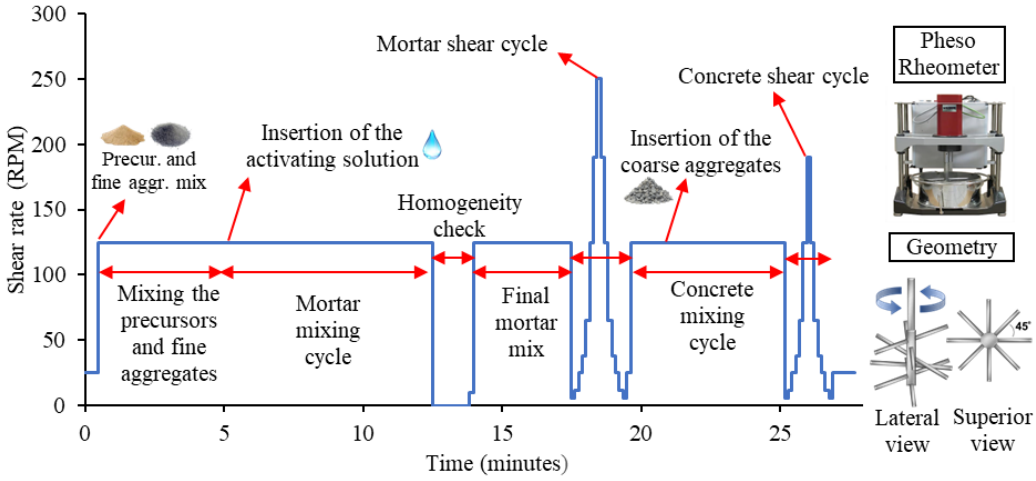

Source: elaborated by the author

4.3.3 Microstructure AAB pastes analysis

The Scanning Electron Microscopy (SEM) test was performed using the equipment Quanta 450 FEG – FEI. The AAB pastes M1, M2 and M3 had their microstructure analyzed under ambient and thermal curing, at 28 days.

4.3.4 Fresh and hardened states tests on AAB concretes

The rheology of mortars and concretes is more complex than the rheology of pastes due to the insertion of aggregates of different shapes and sizes and the heterogeneity of the mixture (HAFID et al., 2016; ALONSO et al., 2017). Moreover, the rheology of AAB concretes is even more complex than PCCs. This occurs due to the higher apparent viscosity and complex interaction between the materials that compose the AABs (ALONSO et al., 2017; LU et al., 2021). In addition, the literature presents few studies for rheological behavior comparison, being mainly focused on single-point tests that measure flow time and passing ability. Therefore, for comparative purposes, single-point tests on the concretes were also performed.

At the fresh state, tests were performed to evaluate the self-compacting behavior. The single-point tests were slump flow and $T_{50,}$ performed according to the ASTM C1,611 (2010) standard and the J-ring test, by the ASTM C1,621 (2017) standard. The results were classified according to the self-compacting criteria of the EFNARC (2005). At the hardened

state, according to the ASTM C39 (2020) standard, the compression test was conducted on a 1000 kN universal testing machine (EMIC PCE100C) after 28 days of cure. The loading rate was set to 0.45 (± 0.15) MPa/s.

4.4 Results and discussion

4.4.1 AAB pastes

4.4.1.1 Setting time

M1 and M2 AAB pastes presented longer initial setting times, 13.6 hours, and 11.3 hours, respectively. In contrast, M3 AAB paste presented an initial setting time of 4.0 hours. This is explained by the fact that this AAB paste has a higher amount of SS (Table 4.2) and thus a higher calcium content (SINGH; MIDDENDORF, 2019; XIE et al., 2020), which reduces the initial setting and increases the gel formation and precipitation, since SS has higher calcium content compared to FA (HADI; ZHANG; PARKINSON, 2019; ALNAHHAL; KIM; HAJIMOHAMMADI, 2021; LU et al., 2021). After the initial setting times, the AAB pastes required 1.4 to 1.9 hour to reach the end setting time.

4.4.1.2 Rheology

The flow tests performed are shown in Figure 4.7. In the M2 AAB paste, a thixotropic behavior was observed, denoted by the presence of hysteresis areas, which results from increasing curves higher than the decreasing curves. This is associated with the greater presence of sodium silicate as an activator in this AAB paste with S/N of 1.25 (Table 4.2) (PALACIOS; BANFILL; PUERTAS, 2008; PROVIS; VAN DEVENTER, 2019; LU et al., 2021). The increase in S/N rose the thixotropic behavior and the apparent viscosity (ALNAHHAL; KIM; HAJIMOHAMMADI, 2021). The higher amount of soluble silica present in sodium silicate promotes the formation of alkali activation gels, especially the quick formation of C-A-S-H (CaO-Al_2O_3-SiO_2-H_2O) type gels, which provides the increase of colloidal forces between the particles (ALNAHHAL; KIM; HAJIMOHAMMADI, 2021; PALACIOS et al., 2021).

Figure 4.7 - Results of the loading histories from the flow tests (a) 10 minutes, (b) 60 minutes

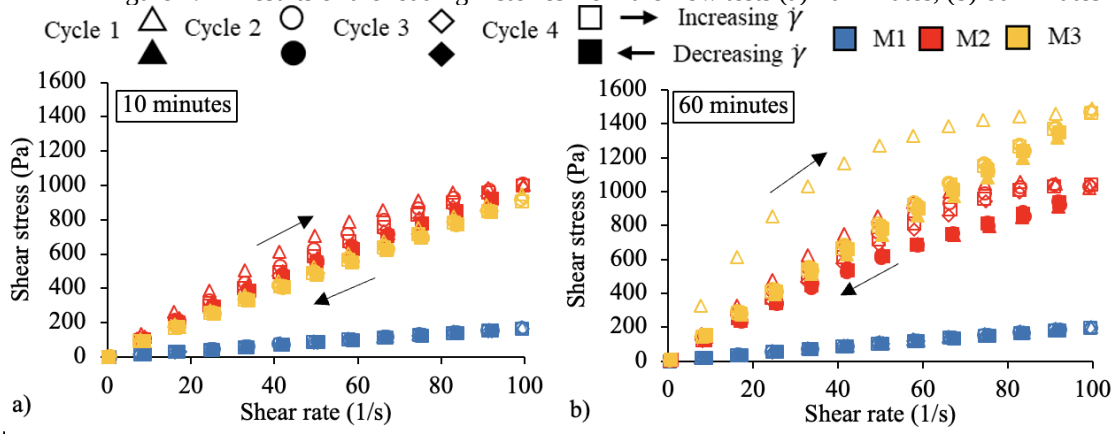

Source: elaborated by the author

The M3 AAB paste presented an increasing curve higher than the decreasing curve in the first loading cycle at 60 minutes after contact between activators and precursors. However, this behavior was not observed in the following cycles, indicating that the pre-shear cycle did not provide sufficient microstructure breakdown and the results should not be associated with thixotropy. Unlike M1 and M2 AAB pastes, M3 paste showed a significant difference between the shear stresses obtained for the same shear rates between 10 minutes and 60 minutes after contact between activators and precursors, with an increase in their values by approximately 50%. This is associated with the greater presence of calcium, which results in a reduction of the setting time (HADI; ZHANG; PARKINSON, 2019; ALNAHHAL; KIM; HAJIMOHAMMADI, 2021; LU et al., 2021). The M1 AAB paste did not show hysteresis areas, behavior associated with its low S/N and its high N/B (DAI et al., 2020; ALNAHHAL; KIM; HAJIMOHAMMADI, 2021).

To identify rheological parameters and to describe the material behavior with a rheological model, the AAB pastes had the fourth decreasing cycle plotted in Figure 4.7 and Figure 4.9. Figure 4.8 shows the approximation of the flow curve points by the Bingham model and the slopes of the initial and final 3 points. This model "forced" the creation of yield stress that was not measured experimentally, as verified in the model equations (Figure 4.8). This is more evident for AAB pastes M2 and M3. However, the reduction from the initial to the final slope is noticeable, which contrasts with the proportionality between shear stress increments and shear rate increments dictated by the Bingham model.

Figure 4.8 - Flow test results based on Bingham model approach: Shear stress *versus* Shear rate

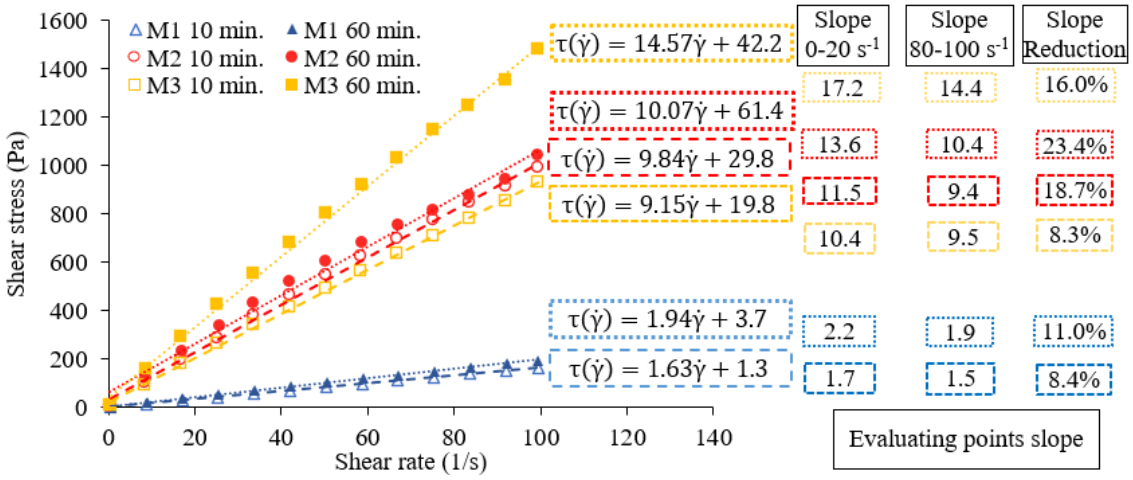

Source: elaborated by the author

In Figure 4.8, it can be seen by the equations that M1 AAB paste presented lower values of plastic viscosity and a slight increase between AAB pastes after 10 and after 60 minutes of contact between activators and precursors (1.63 Pa.s and 1.94 Pa.s). This behavior was also observed in M2. Meanwhile, M3 presented a greater variation in plastic viscosity measured at 10 minutes and 60 minutes. At 10 minutes, M3 presented a plastic viscosity value (9.15 Pa.s) lower than M2 (10 and 60 min). However, at 60 minutes it reached the highest plastic viscosity value (14.57 Pa.s) amongst the analyzed AAB pastes. This phenomenon is associated with the higher calcium content of this composition, associated with a higher amount of SS (ALNAHHAL; KIM; HAJIMOHAMMADI, 2021; LU et al., 2021).

The M1 AAB paste exhibited lower plastic viscosity values (1.9 Pa.s, at 10 minutes, to 2.65 Pa.s, at 60 minutes) compared to the literature. Alnahhal, Kim and Hajimohammadi (2021) obtained plastic viscosity values of 6.3 Pa.s for a mix of FA (75%) and GGBFS (25%) activated by a blend of sodium hydroxide and sodium silicate. The obtained values were close to those presented by Alnahhal et al. (2021), who obtained plastic viscosity values of 6.6 Pa.s (10 min.) and 13.2 Pa.s (40 min.) for a mix of FA (80%) and GGBFS (20%), activated by sodium silicate.

The second rheological model used to evaluate the behavior of AABs was the Hershel-Bulkley model. However, as the equations based on this model showed yield stresses very close to zero, the material had its behavior evaluated by the pseudoplastic model, shown in Figure 4.9. The right side of Figure 4.9 shows the slopes of the equations calculated with the pseudoplastic model at 10 $s^{-1}$and 90 s^{-1}.

Figure 4.9 - Flow test results based on pseudoplastic model approach: Shear stress vs. Shear rate

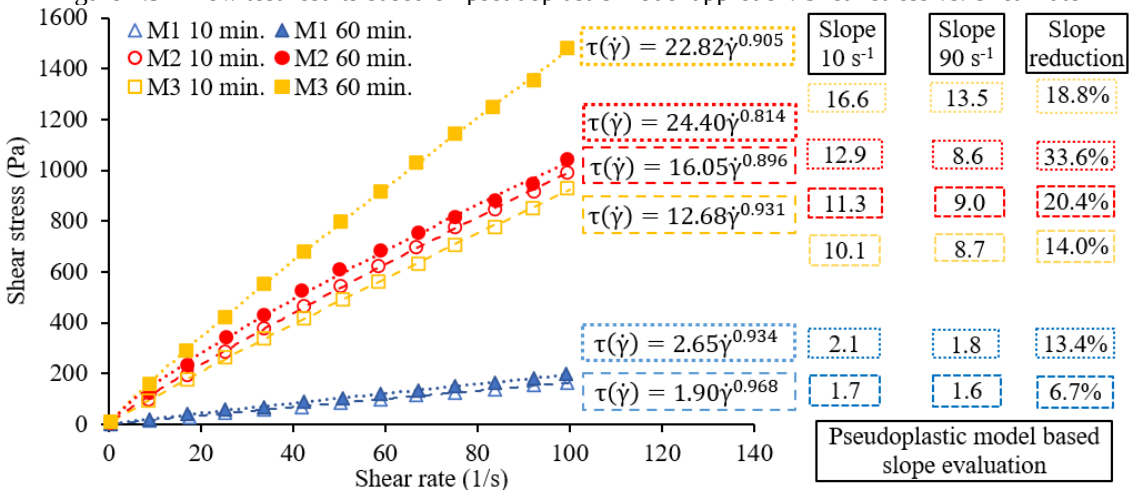

Source: elaborated by the author

The Pseudoplastic model efficiently describes the behavior of the AAB pastes, presenting similar slopes (Figure 4.9) to the readings of the 3 initial and final points of the flow curves as presented in Table 4.4. M1, M2 and M3 AAB pastes presented flow behavior index values (n) greater than 0.8. M1 AAB paste presented values of 0.968 (10 min.) and 0.934 (60 min.), indicating, although not exactly, similarity to the Newtonian model, but this time with proper zero yield stress as observed in experiments. Therefore, the two models (Bingham and pseudoplastic fluid models) described with good general adherence the behavior of the AAB pastes, but the pseudoplastic model was more accurate in terms of correctly capturing the zero-yield stress observed experimentally.

Table 4.4 - Slopes evaluation of AAB pastes

Paste ID	Flow curve slope			Pseudoplastic model-based slope			Bingham model-based slope
	0-20 s^{-1}	80-100 s^{-1}	Slope reduc.	10 s^{-1}	90 s^{-1}	Slope reduc.	
M1 10 min.	1.7	1.5	8.4%	1.7	1.6	6.7%	1.63
M1 60 min.	2.2	1.9	11.0%	2.1	1.8	13.4%	1.94
M2 10 min.	11.5	9.4	18.7%	11.3	9.0	20.4%	9.84
M2 60 min.	13.6	10.4	23.4%	12.9	8.6	33.6%	10.07
M3 10 min.	10.4	9.5	8.3%	10.1	8.7	14.0%	9.15
M3 60 min	17.2	14.4	16.0%	16.6	13.5	18.8%	14.57

Source: research data

Based on the results presented, increasing the liquid/binder (L/B) ratio did not decrease the apparent viscosity in any of the AAB pastes. This occurred because the flow curves of the M3 paste (10 min.), of L/B ratio 0.4, were lower than the M2 paste (10 min. and 60 min. after contact between activators and precursors) of L/B ratio 0.45. This is associated with the higher S/N of the M2 paste (1.25) compared to the M1 and M3 pastes (0.75), which leads this paste to a greater amount of sodium silicate solution, an activator with higher apparent viscosity than sodium hydroxide solutions (VANCE et al., 2014; ALNAHHAL; KIM;

HAJIMOHAMMADI, 2021). The M1 paste, with an L/B ratio of 0.5, presented the lowest values of the flow consistency index (1.896 at 10 min. and 2.647 at 60 min. after contact between activators and precursors).

Figure 4.10 shows the apparent viscosity values of the material at different shear rates. In all AAB pastes, it is perceptible the reduction of apparent viscosity with increasing shear rate, a characteristic behavior of pseudoplastic materials. This occurs because the particles tend to assume a preferential orientation in the direction of flow, minimizing their resistance to flow (IRGENS, 2014). This process should occur practically instantaneously, for the M1 and M3 pastes, since no thixotropy was observed. Therefore, higher L/B ratios provided lower reductions in apparent viscosity and AAB pastes with higher N/B and lower S/N can produce AAB pastes with behavior closer to that of a Newtonian fluid.

Figure 4.10 - Flow test results based on pseudoplastic model approach: Apparent viscosity *versus* Shear rate

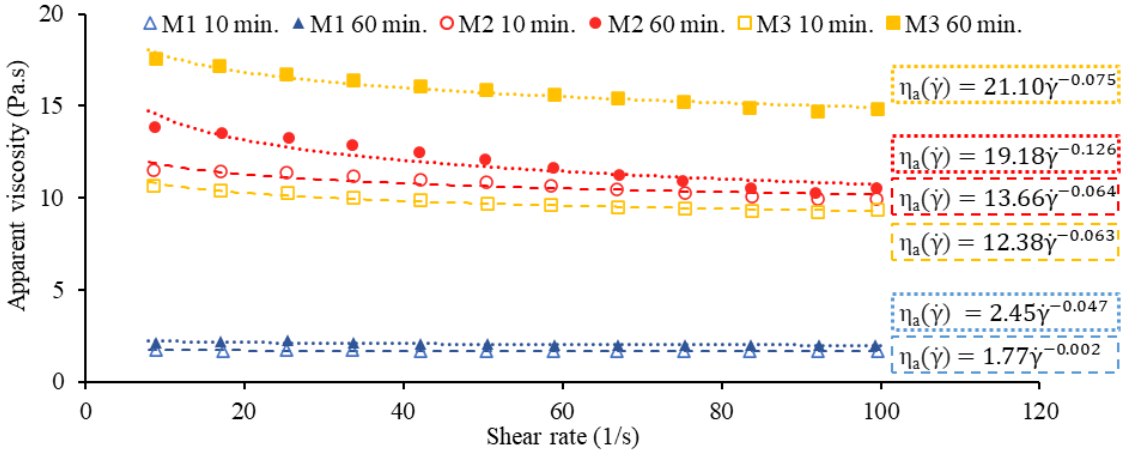

Source: elaborated by the author

Oscillatory test results are shown in Figure 4.11. Initially, the AAB pastes presented phase angle values close to 90º, characteristic of a Newtonian fluid. However, they were reduced to values up to 45º during the initial 15 minutes. This initial viscous behavior may be associated with the conditioning and pre-shearing before the oscillatory test (ROUYER; POULESQUEN, 2015). The values of G" were always higher than G', describing a behavior more viscous than elastic for the measured period. This behavior is characteristic of stages I and II (ALNAHHAL; KIM; HAJIMOHAMMADI, 2021).

Figure 4.11 - Results (storage modul., loss modul. and phase angle over time) from the oscillatory tests

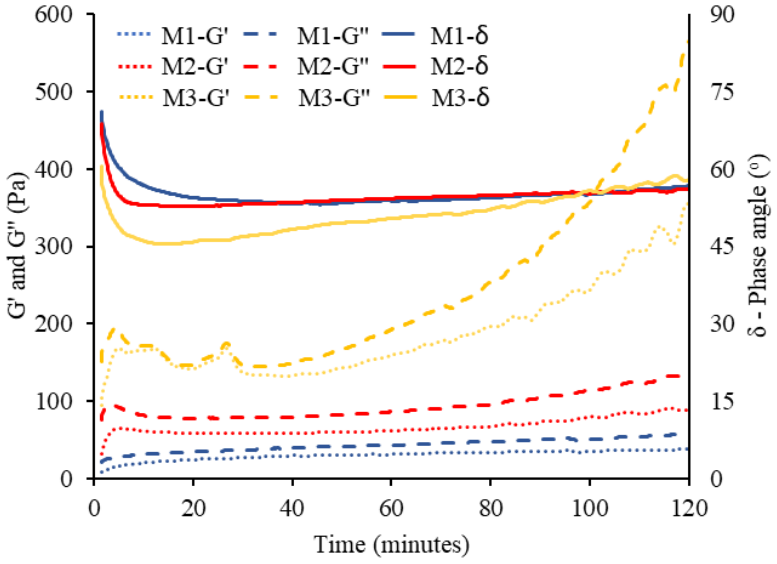

Source: elaborated by the author

Based on the results of the oscillatory test, the material was classified into 4 stages, as suggested by Alnahhal, Kim, and Hajimohammadi (2021). For M1 and M2 AAB pastes, only stages I and II were observed, which is justified by the initial setting time higher than 11 hours, presenting slow changes in its internal structure (KONDEPUDI; SUBRAMANIAM, 2019). For M3 AAB paste, stages I and II presented reduced time, which may be associated with the higher SS content (ALNAHHAL; KIM; HAJIMOHAMMADI, 2021). This occurs because the dissolution of calcium-rich precursors, such as steel slags, tends to be faster than in low calcium precursors (LU et al., 2021). That promotes the precipitation of C-A-S-H (CaO-Al_2O_3-SiO_2-H_2O), which works as nucleation points for structure formation (PALACIOS et al., 2021; LU et al., 2021) and provides the reduction of phase angle values (DAI et al., 2020). Stage III was also observed and was characterized by an increase in the phase angle throughout the rest of the test, from 45º to values close to 60º. Similar behavior was observed in the literature, which shows a more accentuated increase of G" compared to G' (DAI et al., 2020; ALNAHHAL; KIM; HAJIMOHAMMADI, 2021; ALNAHHAL et al., 2021). This may be associated with the polycondensation step of alkali activation, when occurs the release of water in the system (ROUYER; POULESQUEN, 2015; DAI et al., 2020; ALNAHHAL; KIM; HAJIMOHAMMADI, 2021).

4.4.1.3 Scanning Electron Microscopy (SEM)

Figure 4.12 and Figure 4.11 show the SEM images of the 3 evaluated AAB pastes (Table 4.2). Based on these, the M1 paste presented a higher amount of voids, due to its higher

activator/precursor ratio (0.5) (ZHANG; WANG, 2015; CUI et al., 2019). The voids are mostly associated with the structure created by the water released during the curing process (LLOYD et al., 2009; WANG; ALREGAE; DAI, 2019). As higher the amount of water present in the binder higher tends to be its porosity (ZHANG; WANG, 2015; CUI et al., 2019). The higher porosity of AABs is also associated with the lower calcium content, as observed in M1 and M2 pastes (ZHANG; WANG, 2015; SOUTSOS et al., 2016).

Figure 4.12 - SEM images of AAB under ambient cure for: a) M1; b) M2; c) M3

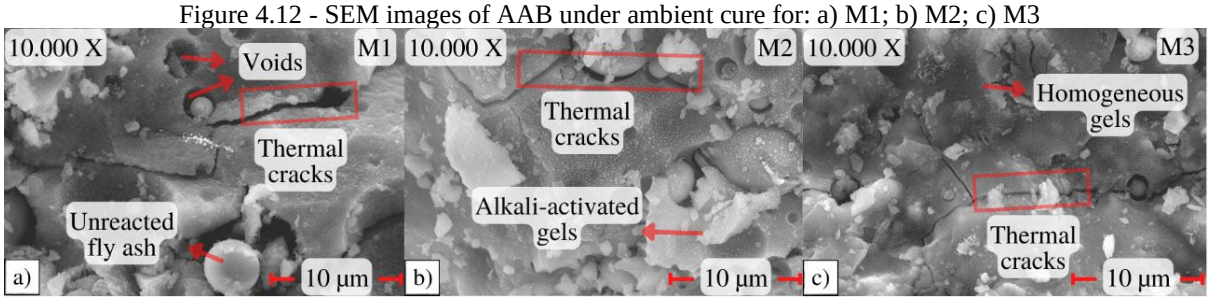

Source: elaborated by the author

Figure 4.13 - SEM images of AAB under thermal cure for: a) M1; b) M2; c) M3

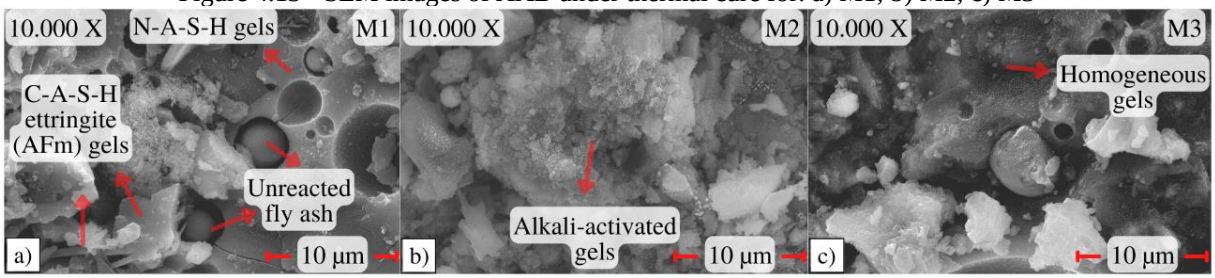

Source: elaborated by the author

AAB pastes after thermal curing (65 °C) presented thermal cracks, as can be seen in Figure 4.13. These cracks, when associated with a high porosity, can easily promote a pathway for harmful substances to the durability of the material (ZHANG; WANG, 2015; SOUTSOS et al., 2016). The chemical composition of the precursors influences the microstructural characteristics of AAB pastes directly (PROVIS; VAN DEVENTER, 2019). The M3 pastes presented a denser and more homogeneous appearance, which is associated with the higher calcium content of this AAB paste, the possible coexistence between C-A-S-H and N-A-S-H gels (Na_2O-Al_2O_3-SiO_2-H_2O), and the lower activator/precursor ratio (0.4) (NATH; SARKER, 2014; SOUTSOS et al., 2016). M1 and M2 pastes exhibited more spots with a “sugary” looking granular appearance, characteristic of N-A-S-H gels (SOUTSOS et al., 2016).

4.4.2 AAB concrete

M1 paste presented lower values of apparent viscosity and yield stress, which potentializes its application in the production of concretes with higher workability and self-compactability. Moreover, this AAB paste presented longer setting time, which provides more safety in preventing events that can reduce the setting time during concreting, such as increased ambient temperature, the quantity of calcium in the aggregate, and production processes (ASTM 1,611, 2010; LI; THOMAS; PEETHAMPARAN, 2019). For those reasons, the M1 paste was chosen to be applied to the concrete.

4.4.2.1 Rheology

Figure 4.14 shows the mixing curves of the mortars and concretes produced. Mixing parameters such as maximum and stabilization torque, which characterize the homogenization of the mixture, were represented in text boxes in the figure.

Figure 4.14 - Mixing test results of mortars and concretes: Torque *versus* Time
(a) mortars, (b) concretes

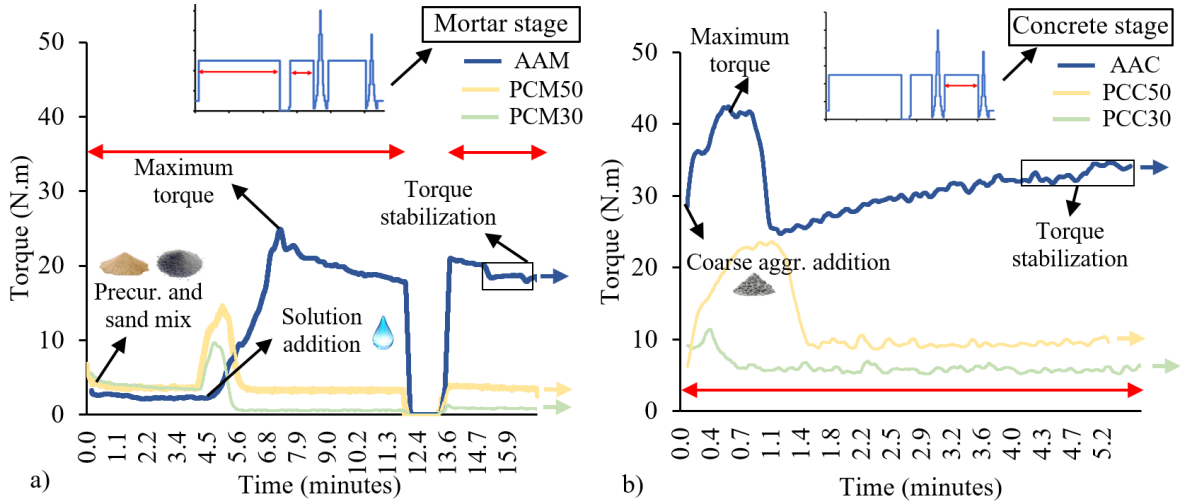

Source: elaborated by the author

The initial addition of the activator solution in the AAB mortar mixing cycle (Figure 4.14) increased the torque due to the formation of clusters by the interaction between the precursors and activators. The flow becomes affected until these clusters completely break down. During this process, a maximum torque (turning point) value is reached, which for AAB mortar was 26.10 N.m. Portland Cement Mortars of 50 MPa (PCM50) and 30 MPa (PCM30) of compressive strength presented lower maximum torque values than AAB mortar, as observed in Table 4.5. AAB mortar torque stabilization occurred at 18.49 N.m, a value much higher than that presented by PCM (Table 4.5). AAB mortar had a mixing energy of 11.59 kN.m.s, a value

22 times higher than the mixing energy of PCM30 and PCM50 mortars (Table 4.5). These behaviors should be associated with the higher apparent viscosity of alkali activator compared to water used in Portland cement mixes (ALNAHHAL; KIM; HAJIMOHAMMADI, 2021).

Table 4.5 - Mixing step results

Analyzed parameters	AAM	PCM30	PCM50	AAC	PCC30	PCC50
Mixing energy (kN.m.s)	11.59	0.55	0.47	9.48	3.60	1.86
Maximum torque (N.m)	26.10	14.60	10.10	43.67	24.31	12.42
Average stabilizing torque (N.m)	18.49	3.59	0.85	33.13	9.55	5.69

Source: research data

The mixing cycle of AAB concrete (Figure 4.14-b) presented an increase in maximum torque (43.67 N.m) and stabilization torque (33.13 N.m) compared to AAB mortar. This was expected due to the addition of coarse aggregates. In Table 4.4 it can also be observed that the mixing energy of AAB concrete was closer to those presented by PCCs, differently from what occurred in mortars. This denotes that the greatest difficulty for this material is associated with the mixing of AABs, a paste of higher apparent viscosity (ALNAHHAL; KIM; HAJIMOHAMMADI, 2021).

Figure 4.15 shows the shear cycles of the AAB mortar and concrete theological multipoint test. Both presented small hysteresis area, characteristic of low thixotropy, behavior intended for activities such as spreading and concrete compaction (ROUSSEL, 2011), expected from a self-compacting concrete. Moreover, the increase in shear rate resulted in a reduction in apparent viscosity, like the pseudoplastic model. Which is useful for operations such as pumping, which imposes high shear rates.

Figure 4.15 - Flow test results of mortars and concretes: Torque vs. Rotation speed vs. Apparent viscosity

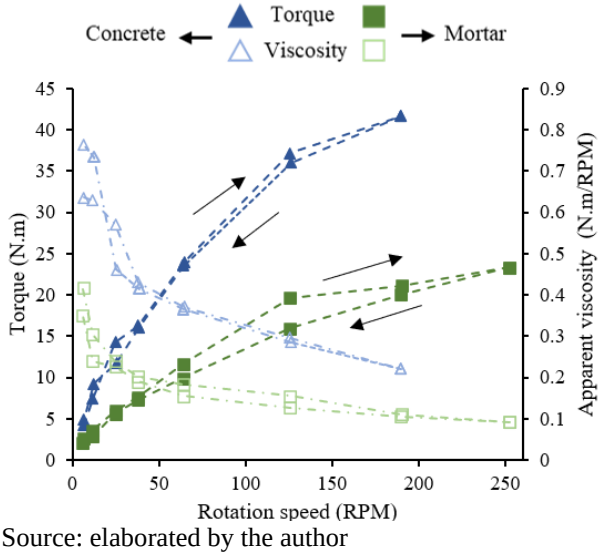

Source: elaborated by the author

Figure 4.16 shows the results of the multipoint flow test of concretes and mortars, which represents the rheological responses of the material, in terms of torque, to different imposed rotation speeds. The literature indicates the Bingham model as the one that best describes the behavior of alkali-activated concretes and mortars (ALONSO et al., 2017; PUERTAS et al., 2018; LU et al., 2021). However, in the present research, the pseudoplastic model more satisfactorily described the AAB mortars and concretes behavior (Figure 4.16). As such, the alkali-activated pastes, mortars, and concretes were all described by the same kind of rheological model. The flow behavior indexes for AAB mortar and concrete were close to 0.6, lower values than for the AAB paste (0.978), then associated with a more prominent pseudoplastic behavior, a phenomenon attributed to the insertion of aggregates. It is also observed that AAB mortars and concretes show higher torque values for the same rotation speed (associated with the rotation speed) than PCMs and PCCs, behavior intensified with the increase in rotation speed. Since the planetary rheometers used in the consulted literature presented different bowls and geometries (PUERTAS et al., 2018) from those used in the present research, it was not possible to compare the results obtained for AAB mortar and concrete.

Figure 4.16 - Concretes and mortars results based on pseudopl. model approach: Torque *versus* Rot. speed

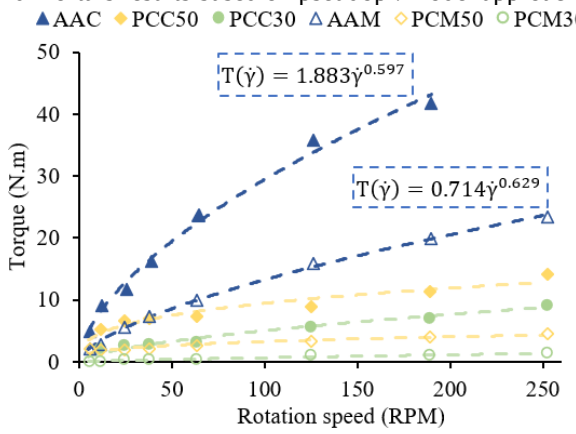

Source: elaborated by the author

4.4.2.2 Flow time and passing ability

The results of the self-compacting concrete evaluation tests are presented in Table 4.6. According to the T_{50} test, the AAB concretes were classified in the VS2 apparent viscosity class. However, the flow time for AAB concretes mixed with the free fall concrete mixer (13.8 s) and in the planetary rheometer (37.0 s) was much longer than 2 s (time considered for VS2 class). Such result indicates a slow flow, characteristic of the binder employed (ALONSO et al., 2017; LU et al., 2021; ALNAHHAL; KIM; HAJIMOHAMMADI, 2021). In the slump flow test, the AAB concretes achieved the minimum spread class, SF1. The AAB concrete showed

no evidence of segregation or bleeding. In the J-ring test, the material showed a difference between the spread measured by Slump Flow and J-Ring Flow in the range of 25 mm to 50 mm, which classifies the AAB concrete as minimal to noticeable blocking. The spreading and passing ability presented by the AAB concrete had no significant differences between the mixing procedures used, but the flow time suffered great variation.

Table 4.6 - Fresh state test results for alkali-activated concretes

Fresh state test	**Free fall mixer**	**Rheometer (Planetary mixer)**	**Classification based: EFNARK and ASTM C1,611-C1,621**	
T_{50} (s)	13.8	37	$T_{50} \leq 2$ – VS1	$T_{50} \geq 2$ – VS2
Slump Flow (mm)	575	615	550 to 650 – SF1	660 to 750 – SF2
J-ring (mm)	27	35	0 to 25 – no block.	25 to 50 – min. block

Source: research data

In previous works, Saini and Vattipalli (2020), for mixtures of GGBFS activated by sodium hydroxide and sodium silicate, found values of 4.5 s, 665 mm and 5 mm for T_{50}, slump flow and J-ring tests, respectively. Huseien, Sam and Alyousef (2021) found, for the same tests, values of 5.5 s, 630 mm and 10.5 mm, respectively, for mixes of FA (70%) and GGBFS (30%) activated by a blend of sodium hydroxide and sodium silicate. In the research presented in this paper, similar values were found for slump flow tests, and lower values for T_{50} and J-ring tests. The better performance of the AAB concrete evaluated in this paper may be associated with the use of superplasticizer additives and/or formulation of the activators employed (PRADHAN et al., 2022). According to the results obtained, the AAB concretes could be classified as a self-compacting concrete. However, the material presented a very slow flow, which may affect its ability to fill the forms when applied in the field, which should be an object of future works focusing on larger scales of application.

4.4.2.3 Compressive strength

The average values of AAB concrete' compressive strength at 28 days are reported in Figure 4.17. The AAB concrete mixed in the free fall mixer presented compressive strength under ambient and thermal curing of 40.3 MPa and 64.1 MPa, respectively. When mixed in the planetary mixer, it presented compressive strengths of 48.6 MPa and 77.1 MPa. The mixing energy employed by the planetary mixer provided an increase of over 20% of the concrete compressive strength compared to that produced in the concrete mixer. However, as discussed in section 5.2.2, it resulted in a loss of fluidity. It was noted that the mixing energy applied by the planetary mixer provided greater interaction between the constituents, affecting the properties of the fresh and hardened state of AAB concretes (HEMALATHA et al., 2015).

Figure 4.17 - Compressive strength of alkali-activated concretes

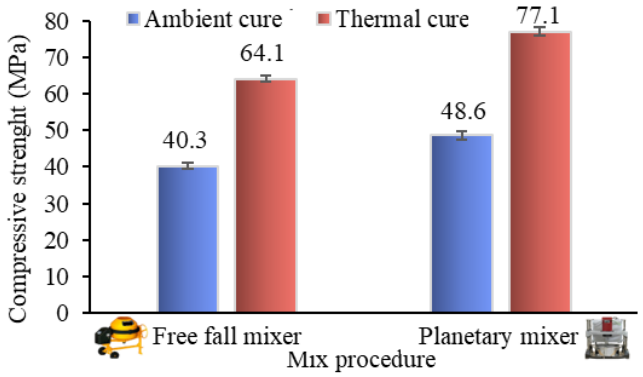

Source: elaborated by the author

For both mixing processes, thermal curing resulted in approximately 59 % higher compressive strength values than ambient curing. The literature reports several compressive strength values for AAB concretes. Noushini et al. (2020) obtained compressive strengths of 42.6 MPa at ambient curing and 62.5 MPa at thermal curing for mixes based on GGBFS and FA. Thomas and Peethamparan (2017) obtained compressive strengths of 55 MPa at ambient curing and 75 MPa at thermal curing for mixes based on GGBFS and FA. Compared to the results obtained by the studies of alkali-activated self-compacting concretes, the present research showed higher compressive strength values. Saini and Vattipalli (2020) found maximum values of 47.9 MPa for GGBFS mixes and Huseien, Sam and Alyousef (2021) reached values up to 47.3 MPa for FA and GGBFS mixes. Thus, the material offered high potential for application based on its mechanical properties.

4.5 Conclusions

In this study, rheological evaluations were performed on AAB pastes and concretes. The analysis of the AAB pastes resulted in discussions about the effects of different formulations of precursors (fly ash and steel slag) and activators (sodium hydroxide and sodium silicate) on the material rheological parameters and model. Although the different formulations of the AAB tested did not influence significantly the compressive strength of the tested materials, distinct rheological responses were observed. The tests performed on the alkali-activated self-compacting concretes resulted in discussions about the impact of the mixtures produced in a planetary mixer and in a free fall mixer on the rheological and mechanical behavior. The results allowed the classification of AAB concretes regarding their rheological and mechanical performance. Based on the analyses of the results, the following conclusions for alkali-activated pastes and concretes based on fly ash and steel slag can be highlighted:

- The pseudoplastic rheological model best described the behavior of alkali-activated pastes, mortars, and concretes.
- Lower S/N and higher N/B in AAB pastes reduced the values of yield stress and apparent viscosity. The increase of SS content led to an increase in apparent viscosity over time and presented lower setting times. The paste M3, with lower S/N (0.75) and lower content of replacement of FA by SS (75-25, % by mass), resulted in better rheological performance for application in self-compacting concrete.
- AAB pastes presented a more viscous than elastic behavior, denoted by G" values higher than G' for the measured interval (phase angle was greater than 45º).
- AAB concretes presented flow time and passing ability properties that match the self-compacting criteria, but their flow was slow, which may affect their application in this class, which requires future studies for larger scales.
- The mixing process influenced the flow and mechanical properties of AAB concretes. The concrete presented higher compressive strength at 28 days and longer flow time when mixed in the planetary mixer (more mixing energy) instead of the free fall mixer (less mixing energy). Mechanical performance was also impacted by the cure procedure. Thermal curing increased the compressive strength by almost 60% for both investigated mixing procedures. In other words, increasing mixing energy allowed obtaining more resistant materials in the hardened state, with less fluid materials in the fresh state.

This research contributed to the rheological characterization of AAB pastes and concretes based on fly ash and steel slag. The results provided information to better understand the behavior of this material and to support future applications, particularly with respect to rheology, as well as to produce technically viable materials that consume industrial waste products that are still poorly explored, such as steel slag.

5 HIGH-PERFORMANCE SELF-COMPACTING ALKALI-ACTIVATED CONCRETE, BASED ON FLY ASH AND STEEL SLAG, WITH CONVENTIONAL AND STEEL SLAG AGGREGATES

Abstract

There is a growing demand worldwide for more sustainable solutions in engineering, especially concerning the intense carbon footprint of structural composites. Alkali-activated binders (AAB) are described in the literature as materials with great potential to replace, at least partially, Portland cement. This paper aims to propose and to characterize an experimental concrete formulation, using AAB pastes based on fly ash and steel slag (basic oxygen furnace - BOF type) instead of Portland cement and steel slag (baosteel short slag flow - BSSF type), as aggregate, that meets requirements of a high-performance self-compacting concrete (HPSCC). This is done by characterizing mechanical behavior in the hardened state (compressive strength and Young´s modulus) and rheological behavior in the fresh state (J-ring, slump flow and T_{50}), as well as durability aspects (microstructure characterization, water penetration under pressure and chloride ion penetration) and interface transition zone (ITZ) aspects. The results show that HPSCC requirements were fulfilled (64 MPa compressive strength and spread diameter class from 550 mm to 650 mm), but with a material that flows slowly (flow time from 3.5 s to 13.8 s). The material showed conflicting durability indications, due to the high indicatives of chloride penetrability and low water penetration under pressure and porosity. This indicates that further research is necessary to create adapted procedures to characterize the durability of AAB concretes and standardize requirements from test results.

Keywords: Geopolymer concrete, durability, chloride penetration, fly ash, steel slag.

Highlights

- The AAB concretes demonstrated high passing ability and spread but also presented a slow flow;
- BSSF-type steel slag aggregate induced a negative impact on concretes' compressive strength and durability parameters;
- AAB concretes presented lower Young's modulus than expected for conventional concrete of same strength class;
- AAB concretes presented conflicting durability results: lower indicatives based on electrical measurements and higher indicatives based on pore structure, which suggests a need for specific standardization;
- The interface zone between the AAB/aggregates presented a homogeneous and reduced aspect than Portland cement concretes.

5.1 Introduction

Worldwide there is a growing demand for more sustainable solutions in engineering. Concerning civil construction materials, the production of ordinary Portland cement (OPC) has a major role in the carbon footprint for structural composites, corresponding to 5%-7% of greenhouse gas (GHG) emissions worldwide emissions (BENHELAL et al., 2012; HASANBEIGI; PRICE, 2012; SINGH; MIDDENDORF, 2019). It is responsible for releasing

0.73-0.99 tons of CO_2 per ton of produced OPC (BENHELAL et al., 2012; HASANBEIGI; PRICE, 2012). In this background, some alternative materials are highlighted with the capacity both to attend to their structural purpose and to mitigate some waste materials disposals, that could become supplementary cementitious materials (SCMs) (PROVIS; VAN DEVENTER, 2013; SINGH; MIDDENDORF, 2019).

SCMs have a large worldwide production and can be used to produce other kinds of binders, such as Alkali-Activated Binders (AABs), frequently named “geopolymers”, with no need for calcination or direct raw natural materials extraction, produced with only wastes as raw materials. Their application in alkali-activated concretes can imply a direct reduction of the binder carbon footprint from 55% up to 75% (YANG; SONG; SONG, 2012), attending similar strength, workability, and durability (SINGH; MIDDENDORF, 2019; LEE et al., 2019; SAINI; VATTIPALLI, 2022;) compared to normal strength concretes (NSC), high-strength concretes (HSC) and self-compacting concretes (SSC) made with ordinary Portland cement (OPC) concretes, depending on the formulation.

For the formulation of geopolymers, powder materials are frequently used as a source of aluminosilicates, named precursors, and an alkaline solution is used to activate reactions of such materials, by dissolving aluminum and silica. The literature highlights that, in the alkali activation process, the main product gels are C-A-S-H (CaO-Al_2O_3-SiO_2-H_2O) and N-A-S-H (Na_2O-Al_2O_3-SiO_2-H_2O), and that production of wither of them is related to the calcium content (PROVIS; VAN DEVENTER, 2013; PROVIS; VAN DEVENTER, 2019). The curing temperature and the chemical composition of activators and precursors directly affect the alkali activation products (PROVIS; VAN DEVENTER, 2013; PROVIS; VAN DEVENTER, 2019).

Steel slag (SS) has the potential for application in civil construction as aggregate for concrete and as an SCM for cement production, especially when used for alkali-activated binder (NUNES; BORGES, 2021). However, the use of steel slag as both precursor and aggregate are still under development, with few studies (PALANKAR; SHANKAR; MITHUN, 2017; GUO; PAN, 2018; CRISTELO et al., 2019; ZHU et al., 2021; TIAN et al., 2022). Concerning the steel slags themselves, in 2020 the world production of crude steel was 1.95 billion tons (WSA, 2021). which produces approximately 130 to 200 kg of steel slag per ton of steel. (YU; WANG, 2011) and presenting a valuable destination for only 36% of that total generated (NAIDU; SHERIDAN; VAN DYK; 2020; NUNES; BORGES, 2021). The incorporation of this material, in civil construction, can reduce the necessity for natural mineral

extraction, reducing another major aspect. For instance, the world consumes 48.3 billion metric tons of aggregates per year (MOHAMMED; NAJIM, 2020).

Steel slags can be combined with other precursors with established studies to produce high-performance binders (RASHAD; KHAFAGA; GHARIEB, 2021). Another frequent material in such kind of investigations is fly ash (FA), mainly derived from the combustion of fossil sources (coal, petroleum wastes) and rich in aluminum, iron, and calcium, usually with pozzolanic activity (SOUTSOS et al., 2015). It is to be observed that fly ash is already commonly used in OPC industry when added as a partial replacement for Portland cement. The FA already has several usages in civil construction, but there is potential for use in other materials, such as geopolymers (JUNAID et al., 2015; PAVITHRA et al., 2016).

Binders with intermediate calcium contents can be obtained through binary mixtures of low and high calcium precursors, such as fly ash and steel slag, respectively. Using this combination, it is possible to obtain the coexistence of C-A-S-H and N-A-S-H gels, characteristic of high and low calcium systems, respectively (PROVIS; VAN DEVENTER, 2013; PROVIS; VAN DEVENTER, 2019). This combination allows the creation of a binder with the advantages of each system, such as the high chemical resistance of N-A-S-H gels and the low porosity of C-A-S-H gels, producing binders with superior properties (PROVIS; VAN DEVENTER, 2013; PROVIS; VAN DEVENTER, 2019).

The use of AABs for application in structural composites is a developing area. The industrial production of concretes with adequate fresh-state properties and mechanical performance is still a challenge (ALONSO et al., 2017; SINGH; MIDDENDORF, 2019; XIE et al., 2020; PRADHAN et al., 2022). High-strength concretes can already be produced (XIE et al., 2020). However, due to the high viscosity of AABs, compared to OPC binders (ALONSO et al., 2017), AAB concretes still do not present consistencies compatible with those used by the construction industry. Therefore, it is necessary to produce High-Performance Concrete (HPC) with high strength (over 55 MPa), high durability and high workability, that are sustainable but that are also technically feasible, especially in the fresh state, like Self-Compacting Concretes (SFC).

Despite the positive environmental impact of the potential use of AAB, there is also important to produce material that has adequate strength and high durability in service. Microstructure and nanostructure levels seem to have a very significant influence on this outcome (PROVIS; VAN DEVENTER, 2013; ZHANG; WANG, 2015; TIBBETTS et al., 2020). It is essential to understand how the chemical composition of the precursors used, the

type of aggregate, and the curing process can affect its microstructure behavior and, consequently, the material durability (PROVIS; VAN DEVENTER, 2013; THOMAS; PEETHAMPARAN, 2017; LEE et al., 2019; ALDAWSARI et al., 2022).

The present paper aims to propose an HPSCC alkali-activated concrete and to investigate its fresh state properties, its mechanical properties in the hardened state, and its durability parameters, trying to fulfill similar requirements as those used for OPC conventional concretes and discussing when it is not possible. For the binder, an AAB is produced using steel slag BOF type and fly ash as powder precursors and sodium silicate and sodium hydroxide solution as activators. For the aggregates, either natural or steel slag BSSF-type aggregates are used. The produced concretes were cured by thermal curing (65 °C for 24 hours) and ambient curing (25 °C). The specimens were characterized for microstructural aspect (scanning electron microscopy (SEM) images, and interface transition zone (ITZ) and porosity), mechanical behavior (compressive strength and Young's modulus), and durability parameters (chloride and water percolation, and electrical resistivity).

5.2 Materials and methods

5.2.1 Constituent materials of the AAB concrete

FA from mineral coal combustion and steel slag (SS) from the basic oxygen furnace (BOF) process were used to produce AAB. The specific gravity of the precursors was 2.34 for FA and 3.13 for SS. The specific surface area of the precursors was 4,790 cm²/g (FA) and 3,360 cm²/g (BOF-SS). The particle size distribution (PSD) of the precursors was obtained with a Shimadzu SALD-2300, and the results are presented in Figure 5.1. The FA PSD had an average diameter of 5.6 µm and a maximum diameter of 106.9 µm, while the BOF-SS had an average of 35.4 µm and a maximum diameter of 141.0 µm.

Figure 5.1 - Precursors PSD

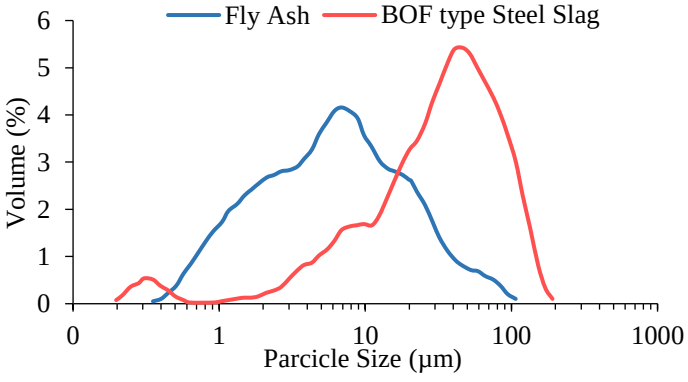

Source: elaborated by the author

Besides its application as a precursor, steel slag type also was used as aggregate, in fine and coarse granulometries. The SS used as aggregates were obtained by the baosteel short slag flow process (BSSF), a different method, mainly concerning cooling procedure using water (CAMPOS; RAFAEL; CABRAL, 2018; AMANCIO, 2019). The oxide composition of these materials was performed by X-ray Fluorescence (XRF) with a Rigaku ZSX Mini II is presented in Table 5.1.

By its chemical composition of precursors, the FA was classified as class F (ASTM C618, 2019), with pozzolanic properties. Both precursors presented high quantities of Al_2O_3, SiO_2, Cao and Fe_2O_3, mainly contributed by the alkali-activated products (PROVIS; VAN DEVENTER, 2019; XIE et al., 2020). The BOF-SS precursor presented a high calcium content (53.14% of CaO). The BSSF-SS aggregate presented an oxide composition similar to the BOF-SS precursor with lower calcium, aluminum and silicon content. This variation is possibly due to the cooling process of the aggregate with water (due to the partial lixiviation of calcium content), decreasing the expansibility, favoring its use as aggregates (CAMPOS; RAFAEL; CABRAL, 2018; AMANCIO, 2019).

Table 5.1 - Chemical composition of precursors by XRF.

Material	Al_2O_3	SiO_2	P_2O_5	SO_3	Cl	K_2O	CaO	TiO_2	MnO	Fe_2O_3
BOF Steel slag precursor (%m.)	1.94	5.64	0.84	0.83	0.04	0.14	53.14	-	2.97	34.40
BSSF Steel slag aggregate (%m.)	0.70	4.78	0.96	-	0.01	0.05	40.46	0.42	4.13	50.14
Fly ash (%m.)	11.14	42.17	0.53	1.08	0.06	3.97	10.25	2.74	0.27	26.98

Source: research data

A blend of 53.1% of sodium hydroxide (NaOH) and 46.9% of sodium silicate (Na_2SiO_3), by mass, was used as activators. Sodium hydroxide was used as a solution, with a concentration of 10 mol/L, composed of 31.3% NaOH and 68.7% H_2O in mass ratios (RAFEET *et al.*, 2017; NAGARAJ; VENKATESH BABU, 2018). The alkaline sodium silicate solution was composed of 14.98% Na_2O, 31.83% SiO_2 and 53.19% H_2O, by mass. These solutions presented a specific gravity of 1.31 and 1.58, respectively. The activator to precursor ratio adopted was 0.5, by mass.

The aggregates used to produce the AAB concretes were composed of natural aggregates and BSSF-SS aggregates, their specifications are presented in Table 5.2. The conventional fine aggregate used was natural sand with a specific gravity of 2.57 and a fineness modulus of 2.66. The BSSF-SS fine aggregate had a dry specific gravity of 3.58 and a fineness modulus of 2.58. The conventional coarse aggregates were composed of two granulometries of

granitic rocks from the same origin. The PSD of the aggregates used were 4.75-12.5 mm and 9.5-25 mm (Figure 5.2). These aggregates had a specific gravity of 2.62 and 2.63, open porosity of 1.5% and 1.6%, and bulk densities of 1,406 kg/m³ and 1,487 kg/m³, respectively. Those aggregates were named “coarse aggregates 1” and “coarse aggregates 2”, respectively. The BSSF-SS coarse aggregate had a PSD range of 9.5-25 mm (Figure 5.2), with a dry specific gravity of 3.60, open porosity of 6.0%, and bulk density of 1,835 kg/m³.

Table 5.2 - Aggregates physical properties

Parameters	Coarse Aggregate			Fine Aggregate	
	Granitic (conv.)		BSSF-SS	Quart sand (conv.)	BSSF-SS
PSD (mm)	4.75-12.5	9.5-25	9.5-25	-	-
Bulk density (kg/m³)	1,406	1,487	1,835	-	-
Open porosity (%)	1.5	1.6	6.0		
Specific gravity (-)	2.62	2.63	3.60	2.57	3.58
Fineness modulus (-)	-	-	-	2.66	2.58

Source: research data

Figure 5.2 - Aggregates PSD

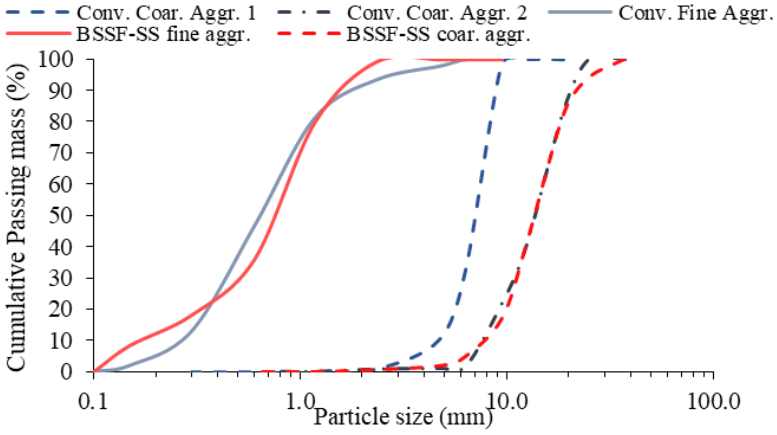

Source: elaborated by the author

5.2.2 AAB concretes mix proportions

The visual aspect of the AAB concretes is presented in Figure 5.3. In Figure 5.3-a the formulation with conventional aggregates is presented, while Figure 5.3-b does the same for the concrete with BSSF-SS aggregate.

Figure 5.3 - Aspect of sections of the produced AAB concretes
(a) Ground specimen with conventional granitic aggregate (b) Ground specimen with BSSF steel slag aggregate

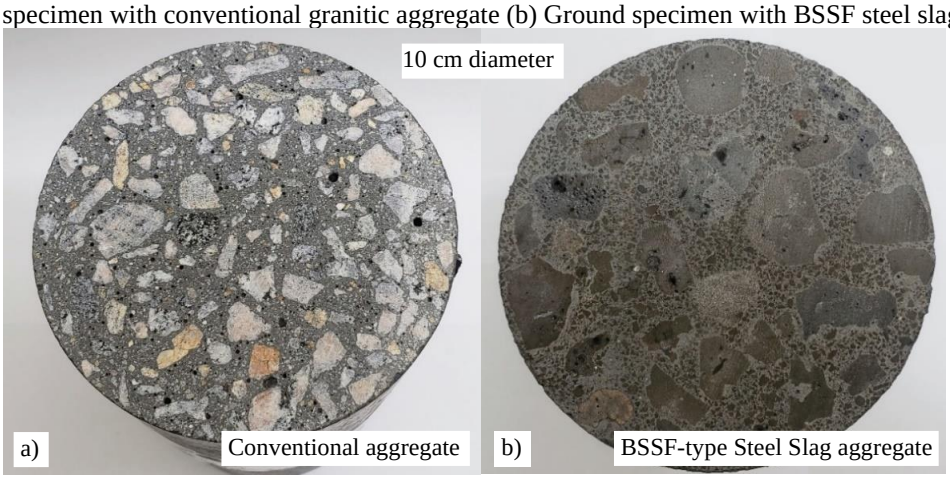

Source: elaborated by the author

This paste was selected due to its high compressive strength, with values of 65 MPa under thermal (65 °C during 24 hours in a laboratory oven) and 50 MPa under ambient curing (25-30 °C) with a good performance in the fresh state compared to other formulations. This AAB paste was produced using FA and BOF-SS, in the mass proportions of 75% FA and 25% BOF-SS, and a bland of 53.1% of sodium hydroxide (10mol/L) and 46.9% of sodium silicate (14.98% Na_2O, 31.83% SiO_2 and 53.19% H_2O_3), by mass, as activators. The alkali content (N/B, i.e. Na_2O/binder precursors, represented as a mass ratio) was 10% and the silica modulus (S/N, i.e. SiO_2/Na_2O activator, represented as a mass ratio) was 0.75.

For the production of alkali-activated concretes, combinations of coarse and fine aggregates composed of 100% natural or 100% steel slag aggregates were used. The aggregate void content was optimized using packing analysis, to determine the optimal proportion (RAFEET et al., 2017; BONDAR et al., 2019), as shown in Figure 5.4. The aggregates void content was calculated for the conventional and BSSF-SS aggregates, based on the combined materials bulk density and specific gravity. The aggregate ratios were chosen based on the combination that provided the lowest void content. The determined optimal proportion for natural aggregates was 40% of gravel 4.75-12.5 mm and 60% of gravel 9.5-25 mm, with a void content of 41.37%. Figure 5.4 presents the packing curve of the coarse aggregate (composed of 40% of 4.75-12.5 mm and 60% of 9.5-25 mm) and natural sand. The ratio of 35% fine aggregate to 65% coarse aggregate, with a voids ratio of 32.0%, was the chosen ratio for the conventional aggregates. These values were equal to those presented by Rafeet et al. (2017), who used 35% sand and 65% gravel. The same procedure was followed for BSSF-SS sand and gravel (Figure 5.4). The optimal BSSF-SS aggregate ratios were 60% BSSF-SS coarse aggregate 9.5-25 mm and 40% BSSF-SS fine aggregate, with a void ratio of 32.9%.

Figure 5.4 - Void content analysis (a) natural aggregate and (b) BSSF type steel slag aggregate

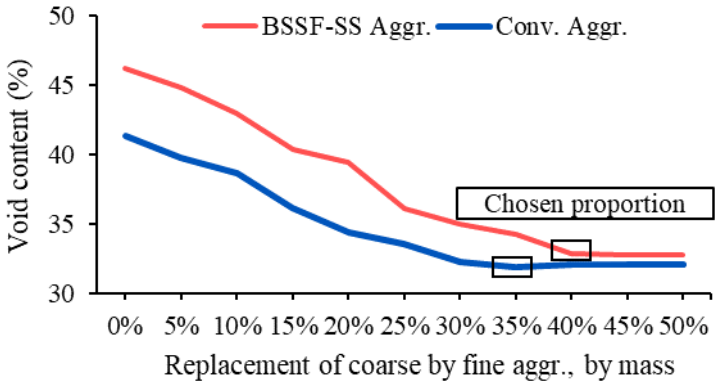

Source: elaborated by the author

A fixed paste content (P%, i.e. paste/concrete, represented as a volume ratio) was adopted to produce an AAB concrete with self-compacting concrete (SCC) properties. SCC requirement was fulfilled for a paste content, in volume, of 38.6%, an amount 20% higher than the initial voids content estimation of 32% in between the aggregate skeleton. This paste content is similar to values in literature such as Bondar et al. (BONDAR et al., 2019), with a range from 24% to 45%. The AAB concrete mixes composition produced during this research is presented in Table 5.3.

Table 5.3 - Mix parameters of AAB concretes

Materials	AAB concrete - Conv. aggr.		AAB concrete – BSSF-SS aggr.	
	(kg/m³)	% vol.	(kg/m³)	% vol.
Fly ash	382.1	16.3	382.1	16.3
BOF Steel slag prec.	127.4	4.1	127.4	4.1
NaOH (solution)	135.9	10.4	135.9	10.4
Na_2SiO_3 (solution)	120.1	7.6	120.1	7.6
Conv. fine aggr.	561.6	21.8	-	-
BSSF Steel slag fine aggr.	-	-	889.3	24.8
Conv. coarse aggr. 1	417.2	16.0	-	-
Conv. coarse aggr. 2	625.8	23.8	-	-
BSSF Steel slag coarse aggr.	-	-	1333.9	36.8

Source: research data

5.2.3 Mixing, fresh state properties and specimen fabrication

Regarding concrete mixing, the procedure consisted of: (i) inserting the coarse aggregate and 10% of the activator solution into the free fall mixer and mixing for 2 minutes; (ii) adding the homogenized precursors and 80% of the activator solution and mixing for 4 minutes; (iii) incorporating the fine aggregate and mixing for 4 minutes; and (iv) adding the remaining activator solution and mixing for 2 minutes.

Less than 1 minute after mixing, the AAB concretes were characterized in the fresh state using slump flow tests, T_{50} (time to reach a spread of 50 cm) (ASTM C1,611, 2010) and

J-ring (ASTM C1,621, 2014; NBR 15,823-3, 2017) and were classified according to the European Federation of National Associations Representing for Concrete (EFNARC) (2005). At last, the AAB concretes were cast into cylindrical plastic 10 cm diameter and 20 cm height molds. The AAB concrete specimens were submitted to either one of two types of cure processes: thermal curing at 65 °C for 24 hours in an aerated oven followed by ambient curing; or only ambient curing with average temperatures between 25 and 30 °C. These two conditions were chosen to evaluate the production of concrete under field conditions, at room temperature, and its maximum strength, obtained through thermal curing (PROVIS; VAN DEVENTER, 2013; JUNAID et al., 2015; XIE et al., 2020).

5.2.4 Mechanical Properties

The tests performed in the hardened state were performed to characterize the mechanical and durability performance of the AAB concretes. The AAB concretes had their compressive strength (ASTM C39, 2020) values determined with a universal testing machine EMIC model PCE100C with a load capacity of 1000 kN. The test was performed according to a loading incremental rate of 0.45 (± 0.15) MPa/s. The compressive strengths were evaluated for ages of 7, 14, and 28 days. Aimed strengths were above 60 MPa, for the production of AAB high-strength concretes (GJØRV, 2008). All the tests of the hardened state were performed on 3 specimens.

Three types of tests were performed to determine the value of Young´s modulus of concrete AABs. The first one was the determination of the static Young´s modulus (ASTM C469, 2022), the most widely used. The property was determined based on longitudinal strain measurements (measured with extensometers positioned in the mid portion of the specimen) making approximately 30% of the rupture load in four cycles. The other two were non-destructive tests, were based on the principle of wave propagation: (i) the resonance impact test (ASTM C215, 2019), using Equation 5.1 for modulus calculation; (ii) and the ultrasonic test (NBR 15,630, 2009; ASTM C597, 2016; NBR 8,802, 2019) with Equation 5.2. To differentiate the non-destructive tests, they will be called resonant Young´s and ultrasonic Young´s modulus.

$$E_{d,r} = DM(n')^2 \tag{5.1}$$

Where, $E_{d,r}$: dynamic Young´s modulus (resonant Young´s modulus), measured by impact resonance (MPa); D: equal to 5,093×(L/d^2), L is specimen length (m) and d is specimen

diameter (m); M: specimen mass (kg); n': longitudinal resonance frequency (Hz). The impact resonance test was performed using the equipment developed by Bezerra et al. (2022).

$$E_{d,u,p-wave} = C_p{}^2 \rho \frac{(1+\mu)(1-2\mu)}{(1-\mu)} \quad (5.2)$$

Where, $E_{d.u,p}$: dynamic Young´s modulus (ultrasonic Young´s modulus), measured by ultrasound (MPa); C_p: velocity of propagation of the ultrasonic P waves (mm/μs); μ: Poisson's ratio (dimensionless), adopted as 0.2 based on recommendations of ASTM C597 (2016) and based on AAB concretes literature (NGUYEN et al., 2015).

The ultrasonic Young´s modulus can be calculated with S-waves measurements, according to Equation 5.3 (MANDEL, 1996)**.** From Equations 5.2 and 5.3 it is possible to calculate the Poisson´s ratio of the material which avoids the utilization of inadequate values, such as 0.2, recommended by ASTM C597 (2016)**.** Both P-waves and S-waves are body waves, but differ in the propagation direction, longitudinal for P-waves and transversal for S-waves (MANDEL, 1996)**.**

$$E_{d,u,s-wave} = 2C_s{}^2(1+\mu)\rho \quad (5.3)$$

Where, $E_{d,u,s}$: dynamic Young´s modulus (ultrasonic Young´s modulus), measured by ultrasound (MPa); C_p: velocity of propagation of the ultrasonic S waves (mm/μs); μ: Poisson's ratio (dimensionless).

In the literature, there is no consensus regarding the measurement and determination of the flight time of the "S" wave. Following the recommendations of the study by Bezerra (2023), the hypothesis for determining the time of flight of the "S" wave was adopted as the instant at which the waves begin to show greater amplitude. This choice is justified, because the "S" waves are waves that have lower velocities, and they arrive after the "P" waves. For the "P" wave flight times, the measurements reported in the equipment, referring to the first deviation, were adopted.

5.2.5 Durability properties: chloride ion penetration; microstructure; porosity

The chloride ingress into concrete can occur by water movement as in the cases of capillarity, permeability and diffusion, or by migration through an electric field (MAZER et al., 2020). It is associated with the corrosive processes of the steel reinforcement, being prejudicial to concrete’s durability (MEHTA; MONTEIRO, 2014). Since concrete structures are usually reinforced by steel bars, this is an important factor to be considered. To directly evaluate the

electrochemical penetration of chlorides, short tests were performed according to ASTM C1,202 (2019), which tries to indicate the passage of chloride ions from the calculation of electrical charge passing through a concrete specimen under constant voltage during a certain time. Another method to estimate the durability of concrete is to measure the electrical resistivity of the concrete, which tries to indicate how easily ions can be transported through the pore structure material by the action of an electric field (ASTM C1,876, 2019). The AAB concretes also had their bulk electrical resistivity measured with the Resipod equipment from Proceq SA, according to ASTM C1,876 (2019) and NBR 9,204 (2012). The measured electrical resistivity values were used to estimate the chloride ion penetrability values and to compare them with the measured values in the chloride ion penetrability test. To get this estimation, Ohm's 1st and 2nd laws were utilized, the concrete was represented as an isotropic material and the power loss between the electrode and the electrolytes was considered negligible (HOPPE FILHO et al., 2013; TIBBETTS et al., 2020).

The electrical resistivity and the penetration of chloride ions are directly influenced by the pore structure and the presence of conductive ions (alkali) in the pore solution (NOUSHINI; CASTEL 2016; ASTM C1,876, 2019; MAZER et al., 2020). Therefore, it is important to evaluate the pore structure of the material, its diameter, tortuosity and interconnection (NOUSHINI; CASTEL 2016; LEE et al., 2019; ALDAWSARI, et al., 2022). To indirectly identify how connected those porous structures are, the test of water penetration under pressure was performed according to EN 12,390 (2019) and NBR 9,204 (2011). To evaluate the distribution of macro-pores and micropores, nitrogen pycnometry and ASTM C642 (2021) tests were performed in the AAB paste.

The microstructure of the interfacing zone (ITZ) between the alkali-activated binder and the aggregates represents the concrete area of higher fragility structure (DEMIE; NURUDDIN; SHAFIQ, 2013; KAI; DAI, 2021). For Portland cement-based concretes, the transition zone at the interface between the paste and the binder usually presents an extension of 20 µm to 100 µm, however, for AABs concretes this thickness is usually reduced to values lower than 4 µm (DEMIE; NURUDDIN; SHAFIQ, 2013). Thus, the binder and the interface between the alkali-activated binder were characterized with scanning electron microscopy (SEM) to evaluate the appearance of the formed gels and the magnitude of the transition zone. The evaluation of the binder's microstructure was also performed.

To complement the characterization of the AAB concretes, the determination of water absorption, void index and density were performed (NBR 9,778, 2009; ASTM C642,

2021). The durability evaluation was focused on the thermal curing AAB concretes, as they presented higher mechanical performance.

5.3 Results and discussions

The results of tests of self-compacting classification, compressive strength, Young's modulus, water penetration under pressure, chloride ion penetration, electrical resistivity and microstructural properties of the AAB concretes will be discussed in the next sections. Besides the characterization of these parameters, the impacts of the exchange of conventional aggregates for steel slag aggregates, as well as ambient and thermal curing on these properties were also evaluated.

AAB concretes with BSSF-SS aggregates presented higher values of apparent densities than those of AAB concretes with conventional aggregates, with 2,842 kg/m³ and 2,306 kg/m³, respectively (ASTM C642, 2021). This behavior was already expected, since BSSF-SS aggregates presented specific gravity values 40% higher than presented by conventional aggregates. The AAB concrete with BSSF-SS aggregates presented an apparent density value higher than 2,600 kg/m³, this concrete can be classified as heavy concrete (NBR 8,953, 2015; EN 206, 2021; NBR 12,655, 2022), a fact that expands its application possibilities, especially for radiation shielding. Palankar, Shankar and Mithun (2017), obtained concrete densities values of 2,528 kg/m³ for natural coarse aggregates and 2,730 kg/m³ for 100% of coarse aggregates, based on BOF-type steel slag. Similar values to the present research.

5.3.1 Self-compacting evaluation

The results of self-compacting concrete properties' evaluation are summarized in Table 5.4 and are based on flow time and passing ability.

Table 5.4 - Results of fresh state AAB concretes

Fresh state tests	AAB concr. Conv. aggr.	AAB concr. BSSF-SS aggr.	Classification based: EFNARK and ASTM C1,621		Slump flow and J-ring aspect
$T_{50\ cm}$ (s)	13.8	3.5	$T_{50} \leq 2s \rightarrow$ VS1	$T_{50} \geq 2s \rightarrow$ VS2	
Slump Flow (cm)	57.5	73.7	55-65 → SF1	66-75 → SF2	
J-ring (mm)	27	34	0-25 → No block	25-50 → Min. block	

Source: research data

The flow time presented by the concretes was higher than two seconds classifying both concrete AABs as VS2 (EFNARK, 2005; NBR 15,823-1, 2017). This behavior is associated with the higher viscosity presented by the binders employed (ALONSO et al., 2017).

The substitution of conventional aggregates for BSSF-SS aggregates resulted in a flow time decrease (13.8 to 3.5), which can be associated with the higher particle size and consequently a lower specific surface area of the aggregated BSSF-SS. The AAB concrete with conventional aggregate reached the slump flow class 1 (SF 1), slump diameter between 550 mm and 650 mm, with a slump flow of 575 mm. AAB concrete with BSSF-SS aggregate achieved slump flow spread class 2 (SF 2), slump diameter between 660 mm and 750 mm, with a slump flow value of 737 mm (EFNARK, 2005; NBR 15,823-1, 2017). The AAB concretes showed low blocking by the J-ring method, with a passing ability between 25 mm and 50 mm (ASTM C1,621, 2014; NBR 15,823-3, 2017). No evidence of segregation or exudation (cf. Table 5.4) was observed during the tests. The utilization of steel slag aggregates improved the fresh state properties of the AABs concretes.

Few research works evaluated the self-compacting of AAB concretes. Saini and Vattipalli (2020), Huseien, Sam and Alyousef (2021) and Mohammedameen (2022) evaluated the self-compacting properties of AAB concretes based on fly ash and ground granulated blast-furnace slag (GGBSF) activated with sodium hydroxide and sodium silicate. The authors obtained similar values for T_{50} (2.6 s - 5.5 s) and slump flow (630 mm - 721 mm) as in this research. Besides, the results of passing ability (5 mm - 10 mm) evaluated by the J-ring method suggested that the referred authors managed to obtain a concrete with better passing ability than that of this research. However, different from other research works, the concrete produced in this study did not use any extra water and/or superplasticizer additives, which may favor workability but negatively affect the mechanical performance (PRADHAN et al., 2022).

5.3.2 Mechanical evaluation

5.3.2.1 Compressive strength

The compressive strengths of AAB concretes at 7, 14 and 28 days are presented in Figure 5.5. The thermal curing process leaded to high initial strength, followed by small increases over time, going from 53.3 MPa (7 days) to 64.1 MPa (28 days), for the AAB concrete with conventional aggregate, and from 42.7 MPa (7 days) to 49.6 MPa (28 days), for the AAB concrete with BSSF-SS aggregates. The AAB concrete with conventional aggregate under thermal curing showed similar strength values to the binder, while the same concrete under ambient curing showed a reduction in its strength by 10 MPa, when compared to the binder under the same cure condition. This may be associated with a positive effect of thermal curing on the interface between the binder and aggregates, discussed in section 5.3.4.6.

Figure 5.5 - Compressive strength of AAB concretes with conventional and BSSF-SS aggregates, at 28 days

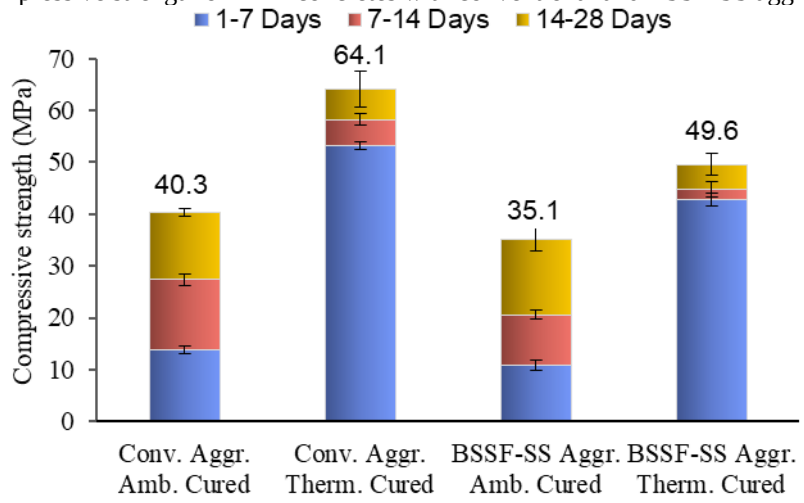

Source: elaborated by the author

A decrease in compressive strength of AAB concretes occurred with the exchange of conventional aggregates for SS aggregates, which dropped from 64.1 MPa to 49.6 MPa under thermal curing and from 40.3 MPa to 35.1 MPa under ambient curing, both at 28 days. Although the change in aggregates improved the passing ability and flow time properties, its effect on strength was negative. This may be associated with the consumption of a part of the alkalis available in the binder by the BSSF-SS aggregates, resulting from the alkaline activation reactions between them, which may have affected the development of binder strength and, consequently, of concrete. However, a uniform transition zone was obtained, and a reduction in binder strength also occurred, as will be discussed in section 3.4.6. Decreases in strength resulting from the exchange of aggregates were also observed in the literature (PRADHAN et al., 2022).

The AAB concretes with conventional aggregates presented a superior mechanical behavior when compared to other self-compacting AAB concretes, such as those presented in section 3.1. Mohammedameen (2022) found maximum strength values of 54.4 MPa; Saini and Vattipalli (2020) found maximum values of 47.9 MPa and Huseien, Sam and Alyousef (2021) reached values up to 47.3 MPa.

AAB concretes with BSSF-SS aggregates showed similar strength values to those presented in the literature related to the use of steel slag aggregates in AAB concretes. Palankar, Shankar and Mithun (2017) obtained strength values of 54.4 MPa and 51.2 MPa in alkali-activated concretes based on fly ash and ground granulated blast furnace slag (GGBFS) for 0% and 100% replacement of conventional coarse aggregate with steel slag, respectively. Palankar Shankar and Mithun (2015) obtained 55.9 MPa for 0% steel slag and 49.8 MPa for 100% steel

slag as aggregate, for mixtures of fly ash and blast furnace slag activated with hydroxide and sodium silicate.

5.3.2.2 Young´s modulus evaluation

The values obtained for Young´s modulus are shown in Figure 5.6. The presented values of resonant Young´s modulus were obtained through the longitudinal resonant frequency (n', cf. Equation 4.1) of AAB concretes. For the resonant Young´s modulus calculations, the measured average resonance frequencies were 8,924 Hz and 9,537 Hz for AAB concrete with conventional aggregates under ambient and thermal curing, respectively, and 8,485 Hz and 8,981 Hz for AAB concrete with BSSF-SS aggregates under ambient and thermal curing, respectively. For the ultrasonic Young´s modulus calculations, the measured average ultrasonic P wave speed (C_p, cf. Equation 4.2) were 4,135 m/s and 4,011 m/s for AAB concrete with conventional aggregates under ambient and thermal curing, respectively, and 4,854 m/s and 4,718 m/s for AAB concrete with BSSF-SS aggregates under ambient and thermal curing, respectively.

The results of static Young´s modulus, presented in Figure 5.6, were between 20.2 GPa and 31.1 GPa. HPC tends to present high strengths and Young's modulus, but although the AAB concretes presented high strengths, high Young's modulus values were not obtained. This is a common behavior for AAB concretes, which can often present about half the values of Young´s modulus of Portland cement concretes of the same order of compressive strength (FERNANDEZ-JIMENEZ; PALOMO; LOPEZ-HOMBRADOS, 2006).

Figure 5.6 - Comparison between the methods for determining Young´s modulus for AABs concretes, at 28 days

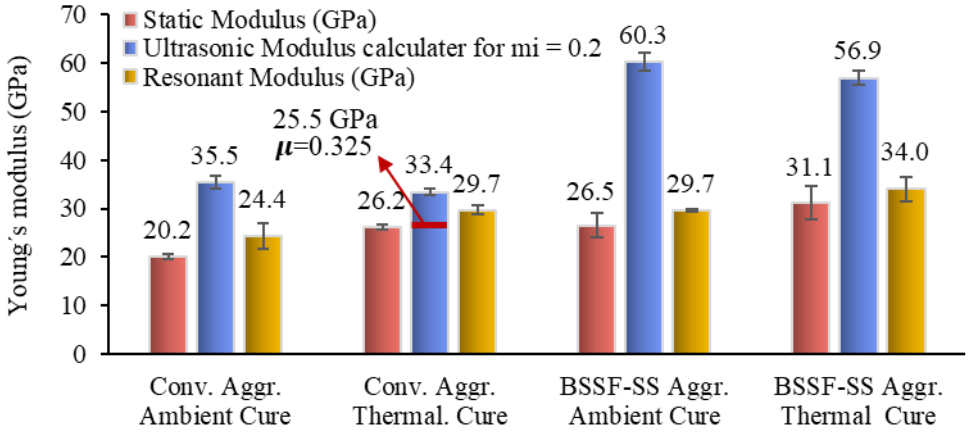

Source: elaborated by the author

Young´s modulus values are affected by the reaction products produced during alkali activation. AABs produced with precursors rich in calcium tend to present higher

modulus values when compared to those with low calcium content, being reported in the literature Young´s modulus values between 12 GPa and 47 GPa (NĚMEČEK; ŠMILAUER; KOPECKÝ, 2011; DING; DAI; SHI, 2016). Because the N-A-S-H gels present lower intrinsic Young´s modulus values than C-S-H gels and other calcium-based gels (NĚMEČEK; ŠMILAUER; KOPECKÝ, 2011; DING; DAI; SHI, 2016). Thus, the use of binary mixtures of precursors with different calcium contents presented intermediate values of Young´s modulus.

The thermal curing induced an increase in Young´s modulus for both aggregate types. Based on the static Young´s modulus results, AAB concretes with conventional aggregates showed an increase from 20.2 GPa to 26.2 MPa, while for AABs with BSSF-SS aggregates, there was an increase from 26.5 GPa to 31.1 GPa. This behavior was expected as thermal curing produced concretes with higher compressive strength at 28 days and this behavior is normally reflected in the modulus values as well (ALIABDO; ABD ELMOATY; SALEM, 2016).

The use of BSSF-SS aggregates increased the values of Young´s modulus, the opposite behavior of the compressive strength. Therefore, the insertion of BSSF aggregates tends to increase Young´s modulus values and can reduce the compressive strength in HPC, a behavior observed (BEUSHAUSEN; DITTMER, 2015). This is associated with the insertion of higher strength and stiffness aggregates, such as steel slag, which have a compressive strength of up to 300 MPa (BEUSHAUSEN; DITTMER, 2015; WANG, 2016). Palankar, Shankar and Mithun (2017), reported small decreases in Young´s modulus values upon the exchange of conventional aggregates for steel slag aggregates. These results were different from the present research.

5.3.2.2.1 Poisson’s ratio

The ultrasonic Young's modulus values were higher than those presented by the other methodologies, with values up to 2 times higher. The use of a Poisson ratio equal to 0.2 may be the cause of this behavior. The dynamic impact resonance methodology that had good accuracy in Young´s modulus values does not use this parameter, while the ultrasonic methodology that uses this parameter presents estimates above the expected. To test this hypothesis were used P-wave (compression waves) and "S" wave measurements (shear waves) on AAB concretes with conventional aggregates, under thermal curing, specimens to estimate this Poisson's ratio. Only this configuration was tested because this hypothesis was only raised after the experimental stage of the research was completed and there was not enough material to produce the 4 configurations analyzed.

The average values of flight time for the "S" waves were 91.1 μs while the average values of flight time for "P" waves were 46.1 μs. Based on these results the value found for Poisson´s ratio was 0.325. This value was much higher than the value used to determine the ultrasonic Young´s modulus presented in Figure 5.6. Therefore, the utilization of the Poisson´s ratio equal to 0.2 is incorrect, and this factor should always be determined to obtain accurate values of the ultrasonic Young´s modulus. With the new Poisson´s ratio, the value of the ultrasonic Young´s modulus for the specimen analyzed changed from 35.4 GPa to 25.5 GPa, presented in Figure 5.6. To evaluate the accuracy of the Poisson's ratio obtained, an inverse calculation was performed in order to find the Poisson's ratio values required to achieve the measured static and resonant modulus results. Table 5.5 presents the results of this analysis. As observed, there is a variability of Poisson's ratio values between 0.27 and 0.42, which confirms that the value adopted by ASTM C597 (2016) for Portland cement materials is not appropriate for AAB concretes.

Table 5.5 - Poisson's ratio value for equivalence between ultrasonic and the others Young´s modulus

Poisson´s ratio based on Young´s Modulus type	AAB concrete - Conv. aggr.		AAB concrete - BSSF-SS aggr.	
	Ambient cure	Thermal cure	Ambient cure	Thermal cure
Estatic modulus	0.387	0.317	0.419	0.393
Resonant modulus	0.351	0.270	0.407	0.379

Source: research data

5.3.3 Durability evaluation

5.3.3.1 Electrical resistivity

The bulk electrical resistivity of the investigated AAB concretes is presented in Figure 5.7. The results found were 1.91 kΩ.cm and 0.97 kΩ.cm for the AAB concrete with conventional aggregate and BSSF-SS aggregate, respectively, both under thermal curing. Those resistivity values classify the concrete as of very high probability of corrosion (AASTHO PP 84, 2020) of the steel rebars. The curing process did not present any significant impact on the resistivity values.

Figure 5.7 - Bulk electrical resistivity of AAB concretes, at 28 days

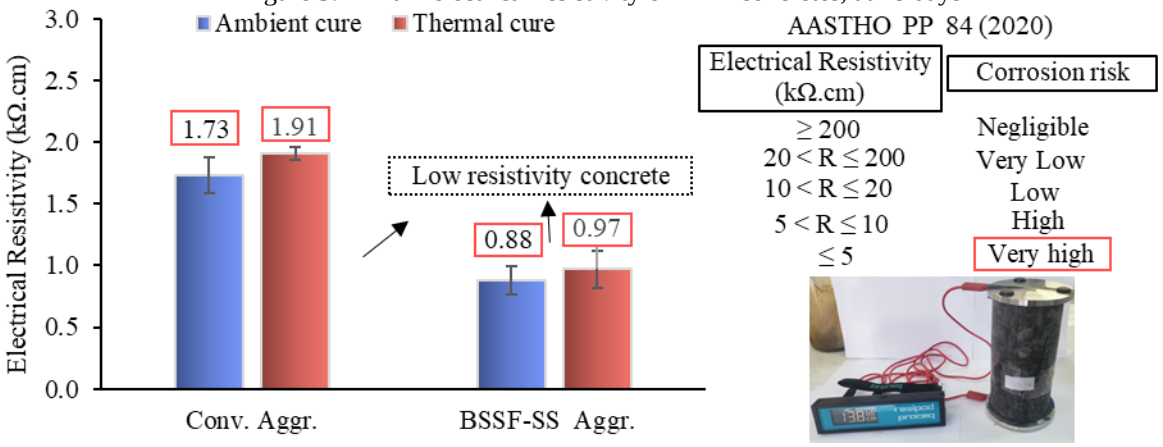

Source: elaborated by the author

The electrical resistivity values were similar to those presented by Noushini and Castel (2016) who found resistivity values of up to 1.19 KΩ.cm, for binary mixtures of fly ash, Kaolite and GGBFS activated with sodium hydroxide and sodium silicate, cured at 60 ºC for 24 hours. The low resistivity values may be associated with the large presence of metallic elements in the precursors or/and the high alkalinity in the pore solution due to the activators employed, such as Na^+ (NOUSHINI; CASTEL, 2016; ASTM C1,876, 2019; MAZER et al., 2020). The presence of very high iron contents in steel slags combined with a higher open porosity of the aggregates may justify the lower resistivity of AAB concretes with steel slag compared to AAB concretes with conventional aggregates, due to a higher conducting network and tunneling conduction (AHMED; KAMAL, 2022).

5.3.3.2 Chloride ion penetration

AAB concretes with conventional aggregate and BSSF-SS aggregate showed chloride ion penetrability results of 8,978 C and 17,332 C, respectively, seen in Figure 5.8. The observed values classify the concrete as high chloride ion penetrability (ASTM C1,202, 2019), a poor indication of durability, as illustrated in Figure 5.8. The specimens of AAB concretes with BSSF-SS aggregates showed indicative of corrosion of electrochemical origin on their surface. The high indications of chloride ion penetrability may be associated with the low electrical resistivity of the material and the porosity present in binders produced with low calcium precursors such as fly ash (PROVIS; VAN DEVENTER, 2013; NOUSHINI; CASTEL, 2016).

Figure 5.8 - Rapid chloride ion penetration test of AAB concretes, under thermal cure, at 28 days

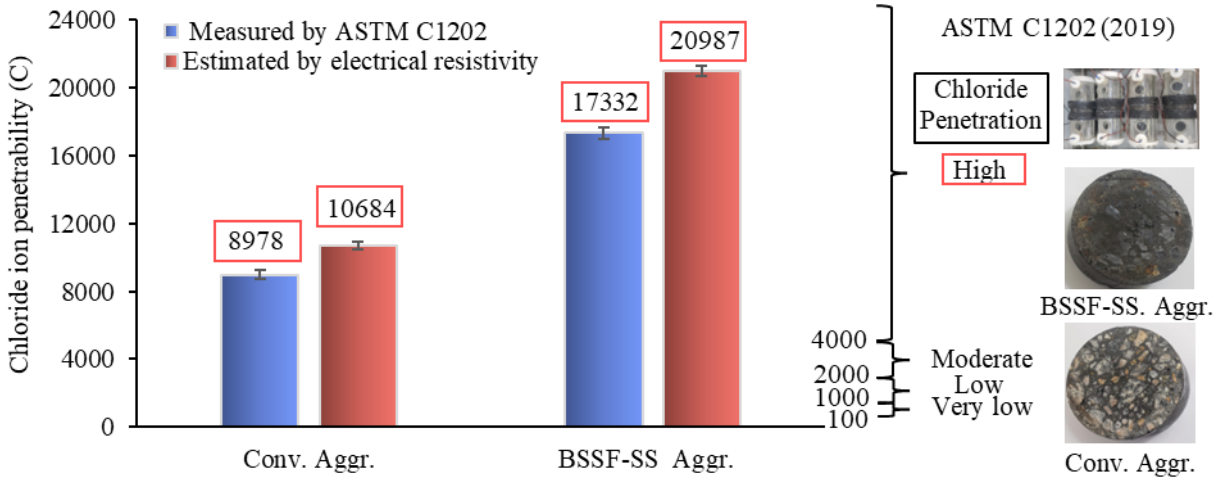

Source: elaborated by the author

Based on the 1st and the 2nd Ohm's laws, on the values of bulk resistivity test measured, on the dimensions of the tested specimen (5 cm height and 10 cm diameter), and on the parameters of test voltage (60 V) and total time (6 hours) of ASTM C1,202, the chloride ion penetrability was estimated. The values obtained were 10,684 C and 20,987 C for the AAB concretes of conventional aggregate and BSSF-SS aggregate, respectively, both under thermal curing, results presented in Figure 5.8. The estimated chloride penetrability values based on electrical resistivity were similar to those obtained using only the chloride ion penetrability test as a parameter, which were 8,978 C and 17,332 C for the same concretes, respectively (TIBBETTS et al., 2020). This indicates that the electrical properties of the material are the most relevant parameter in the chloride ion penetrability test and not the chloride penetration itself, and that electrical resistivity values can be used for the estimation of the currents and passed electrical charges.

Further discussions can also be made regarding the performance of AAB concretes regarding the penetration of chloride ions. Lee et al. (2019), in their studies involving AAB concrete based on fly ash and blast furnace slag, detected that the resistance to chloride ion penetration increases with time. Concretes that presented values of chloride ion penetration close to 4000 C at 28 days decayed to values below 1000 C at 270 days. The same author also detected an increase in strength over the curing days and a reduction and optimization of pore structure. Therefore, from observations from the literature, it is expected that the durability parameters of the AAB concretes produced in this research can improve over time.

5.3.3.3 Water penetration under pressure

The results of the water penetration under pressure test are presented in Figure 5.9. The AAB concretes with conventional aggregates showed an average penetration height of 3.5 cm and AABs concretes with BSSF-SS aggregates showed an average penetration of 17.3 cm, for 20-cm height specimens. This difference between the water penetration values can be attributed to the large porosity of BSSF-SS aggregates (6%), 4 times higher than conventional coarse aggregates (1.6%). The AAB concretes with BSSF-SS aggregate also presented higher porosity values than those presented by AAB concrete with conventional aggregates. The interaction between the binder and BSSF-SS aggregate could be created an interconnected structure, as discussed in section 3.4.6.

Figure 5.9 - Water penetration under pressure of AABs concretes under thermal cure, at 28 days
(a) Conventional Aggregate, (b) BSSF-type Steel Slag Aggregate

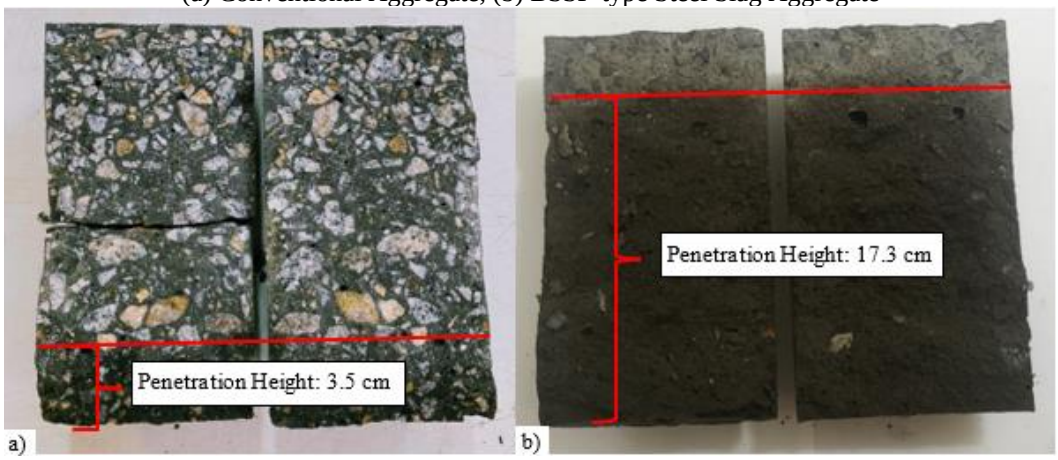

Source: elaborated by the author

The AAB concrete with conventional aggregates presented low values of water penetration under pressure. This concrete can be considered impermeable, since it presented penetration values of less than 5 cm (NEIVILLE; BROOKS, 1997). The literature on this type of test in alkali-activated binders is still incipient. Atabey et al. (2020) studied the penetration of water under pressure in alkali-activated mortars based on fly ash and found penetration values between 9 mm and 150 mm.

5.3.3.4 Microstructure and SEM images of paste

Figure 5.10 presents this research's AAB microstructure under ambient and thermal curing after 28 days of contact between precursors and activators. The paste presented some voids associated with "free" water or water released during the condensation step of the gels, which is totally or partially removed during the curing process (LLOYD et al., 2009; WANG; ALREGAE; DAI, 2019). AAB cured at 65 °C presented a few cracks of thermal origin that

may facilitate the penetration of products harmful to the durability of concrete (ZHANG; WANG, 2015; SOUTSOS et al., 2015).

Figure 5.10 - SEM images of AAB paste, at 28 days
(a) Ambient cure (b) Thermal cure

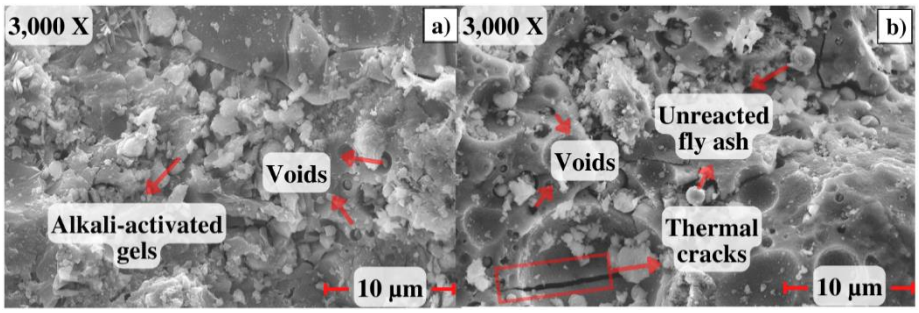

Source: elaborated by the author

AABs composed of precursors with low calcium content (such as fly ash comparatively to steel slag) tend to present a more porous structure, with a sugary-looking granular aspect, and worse performance regarding the penetration of chloride ions (SOUTSOS et al., 2015; ZHANG; WANG, 2015; ZHU et al., 2021). Meanwhile, precursors from binary mixtures or with higher calcium content present a more homogeneous and compact appearance, performing better regarding durability comparisons (NATH; SARKER, 2014; SOUTSOS et al., 2015). The microstructure of the binder applied to the concrete presented a predominantly homogeneous aspect, but with spots of "sugary" aspect. Moreover, the paste presented voids and cracks of thermal origin. This behavior may have been responsible for the low durability of some indicators presented by the concrete, as discussed in section 3.5.

5.3.3.5 Interface Transition Zones (ITZ)

Figure 5.11 presents micrographs of the interfacial transition zones (ITZs) between the conventional aggregates and the AAB for the material after 28 days of contact between precursors and activators. This zone is composed of dense and uniform alkali-activation products highly bound to the aggregate surface (FAN et al., 2020; LUO et al., 2021). The AAB concretes presents a reduced ITZ (up to 4 µm) (DEMIE; NURUDDIN; SHAFIQ, 2013) compared to other concretes, such as those based on Portland cement (from 15 µm to 50 µm) (LUO et al., 2021), is associated with the high strength of AABs concretes (DEMIE; NURUDDIN; SHAFIQ, 2013). The AAB concrete with conventional aggregates under thermal cure, in Figure 5.11-c-d, presented a smaller ITZ and more homogeneous gels, attributed to the thermal curing process. This explains the similar compressive strength values presented by the binder (64.4 MPa) and the AAB concrete with conventional aggregate (64.1 MPa), both under

thermal curing. This was only possible due to the proper interaction between the aggregates interface and the paste and the formation of a transition zone composed of high-strength gels. In other words, there seems not to exist a zone of fragility in the ITZ, since the strength of the binder was inherited directly by the concrete.

Figure 5.11 - Microstructure of the interface zone of AAB concretes with conventional aggregates, at 28 days (a-b) Ambient cure (c-d) Thermal cure

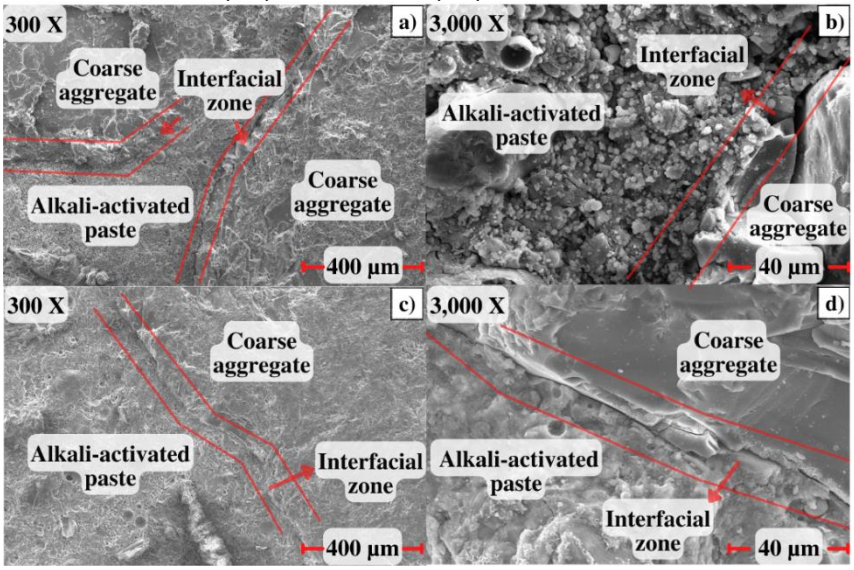

Source: elaborated by the author

It was not possible to identify the zones between the AAB paste and the BSSF-SS aggregate, since the material presented a very uniform appearance. The use of steel slag aggregates optimizes the interfacial zone between the aggregate and the binder (CRISTELO et al., 2019; NUNES; BORGES, 2022) and ITZ delimitations could not be visually detected in the micrographs. This may be associated with the reaction between de binder and SS aggregates, which has similar chemical composition (TIAN et al., 2022). This interfacial interaction occurs due to the formation of hydrated ion agglomerates from the interaction of water accumulated on the surface of the steel aggregate and the migration of metallic cations Ca^{2+} and Na^{+} to this region, forming a stabilized region (TIAN et al., 2022).

5.3.3.6 Porosity

The AAB paste, after thermal curing, presented an open porosity of 33.9%, while under ambient curing presented open porosity of 26.6%. The higher porosity (27% higher) exhibited by AAB pastes under thermal curing may be associated with the faster water exit during the curing process at 65 °C, the presence of thermal microcracks and the production of stronger and more compact alkali activation gels (LLOYD et al., 2009; ZHANG; WANG, 2015; WANG; ALREGAE; DAI, 2019). These results are between 20% and 45% recurrent in the

literature of AAB and OPC (MEHTA; MONTEIRO, 2014; ZHANG; WANG, 2015) that change according to the compositions and proportions of the materials used and the curing method (MEHTA; MONTEIRO, 2014; PROVIS; VAN DEVENTER, 2019). Hardened binder pastes with low calcium content such as fly ash show higher porosity because N-A-S-H gels, common in this type of precursor are less dense than C-A-S-H gels (PROVIS; VAN DEVENTER, 2013; NOUSHINI; CASTEL 2016). The AAB utilized to produce the concrete was composed of 75% of FA to 25% of BOF-SS, by mass, which resulted in the intermediate porosity values.

AAB concrete with conventional aggregate presented an open porosity of 9.4%, while AAB concrete with BSSF-SS aggregates presented values of 11.9%, both under thermal cure at 28 days. The values found were lower than those presented by the AAB concretes of Noushini and Castel (2016) with porosity between 13.7% to 15.4%, for binary mixtures of fly ash, Kaolite and GGBFS activated with sodium hydroxide and sodium silicate, with natural aggregates. The AAB concretes evaluated by those authors showed lower porosity values than the OPC reference concretes, however, the AAB concretes showed lower electrical resistivity, indicative of conflicting durability results.

It is observed that the durability indications found in this research were conflicting. The durability measurements based on electrical parameters presented indications of low durability, but the material presented regular porosity and low water penetration under pressure. Since the chloride ingress into concrete can occur by capillarity, permeability, diffusion, and migration through an electric field (MAZER et al., 2020), the lower porosity observed is not favorable to the ingress of harmful substances such as chlorides, but the lower resistivity can facilitate their electrochemical ingress. Also, the calculated electrical currents allowed demonstrates that the measured electrical current in chloride penetration tests are not necessarily due to chloride penetration, but to materials' low electrical resistivity. Therefore, further analysis should be carried out before classifying the material as low durability concrete. This area is a research gap for future studies.

5.4 Conclusions

In this research, self-compacting concrete parameters, mechanical performance and durability of alkali-activated concretes were evaluated. The alkali-activated binder is composed of a precursor that is a blend of steel slag and fly ash activated with a blend of sodium hydroxide and sodium silicate. The alkali-activated concrete is a mix of the obtained binder and

conventional or steel slag aggregates. Furthermore, two curing processes were evaluated: thermal curing (65°C) and ambient curing. In the fresh state, slump flow, T_{50} and J-ring tests were performed. The mechanical performance of the material was evaluated with compressive strength and Young's modulus tests of various kinds (P-wave ultrasonic testing, impact resonance testing and static modulus testing). The durability behavior was evaluated with chloride ions penetrability tests, electrical resistivity, water penetration under pressure and characterization of the porosity and microstructure. The main conclusions obtained from the results were:

- Obtained AAB concretes present high passing ability. However, they show high flow time in comparison with the OPC concretes.
- The thermal curing process increases up to 60% the values of compressive strength and up to 30% the values of Young's modulus at 28 days.
- The studied AAB concretes present Young´s modulus values lower than those presented by the OPC concretes of similar strength.
- Dynamic methodologies based on impact resonance and ultrasonic waves show satisfactory accuracy for Young's modulus estimation.
- The use of BSSF-type steel slag aggregates produces a decrease in the values of compressive strength and an increase in the values of Young´s modulus and flow time of AABs concretes.

The approaches used to evaluate the durability of OPC concretes provide conflicting durability results when applied to AAB concretes, especially when the durability evaluation is associated with electrical measurements. This should be further investigated and it seems reasonable to suppose that methods of durability investigation should be developed specifically for geopolymer concretes.

AAB concretes presented a reduced transition zone compared to Portland cement concretes. Moreover, the thermal curing process is beneficial for the transition zone properties and for the production of AAB concretes with high strength.

This research contributed to the characterization of AAB concretes based on steel slag and fly ash, with natural and steel slag aggregates. The results provided information regarding self-compacting concrete parameters, compressive strength, Young´s modulus, chloride penetrability, pore structure and interfacial transition zone. In addition, it has contributed to the necessary knowledge for the future utilization of industrial waste to produce technically feasible materials.

6 FINAL CONSIDERATIONS AND SUGGESTION FOR FUTURE RESEARCH

6.1 Final considerations

In Chapter 3, a mix design method for alkali-activated binders and concretes was proposed and apply in AAB based on fly ash and steel slag. This method had as mix design parameters based on the design of silica modulus, alkali content, binary precursors proportions and different curing regime. With the AAB characterization of the it was possible to identify that: lower S/N (0.75) parameters values of the alkaline activators and lower FA content performed better compressive strength results; thermal curing tends to increase compressive strength of the pastes at least initially, but for higher S/N (1.75) thermal curing is not so effective; binders cured at room temperature (25 ^{o}C) can overcome the thermal curing values over time; increasing the incorporation of SS leads to a reduction in the setting time; it is possible to produce high strength pastes with binary mixtures of steel slag and fly ash. The design of materials based on the aggregates packing principle and paste content proved to be effective to produce high compressive strength concretes (64 MPa) with the desired consistency (579 mm, SF1 class).

In Chapter 4, single-point and multipoint rheology tests were performed on alkali-activated pastes and concretes. The objective of the tests was to characterize and optimize the rheology of alkali-activated binders and concretes. Thus, the rheological performance of this material is one of the main obstacles to its commercial application. The multipoint rheological analyses of the AABs allowed the conclude that: AAB pastes adjusted according to Bingham and Pseudoplastic models; lower S/N and higher N/B presented reduction in yield stress and apparent viscosity values; the material presents viscous than elastic behavior; lower S/N (0.75) and lower levels of substitution of FA by SS (0.75/0.25, by mass) present better rheological performance. The rheological analyses of AAB concretes allowed the conclusion that: AAB concretes present consistency indexes close to those of conventional concretes; AAB concretes and mortars presented higher values of maximum torque, mixing energy and apparent viscosity when compared to conventional concretes; the type of mixer influences the flow and mechanical properties of the material; the Pseudoplastic rheological model satisfactorily describes their behavior. The single-point rheological results applied to the concretes indicated that: AAB concretes showed higher passing ability, however under slow flow.

In Chapter 5 the concretes were characterized based on compressive strength, Young's modulus, self-compacting and durability parameters. Furthermore, the influence of the

replacement of conventional aggregates by steel slag aggregates and the curing regime on these properties was evaluated. Based on the results, the main conclusions were: the utilization of steel aggregates showed a decrease in compressive strength, but improvement in self-compacting properties; AAB concretes presented high passing ability, but high flow time compared to OPCs concretes; AAB concretes presented lower modulus of elasticity values than those presented by OPC concretes of same strength; Dynamic methods presented good accuracy for Young´s modulus estimation; AAB concrete presented controversial indications of durability, once it showed low water penetration under pressure but high indications of chloride ion penetration, based on electrical measurements; alkali-activated concretes presented a reduced and dense transition zone when compared to OPC concretes.

Main contributions of this research can be summarized as follows:

- Contribution 1: the production of an effective and simplified design mix, as well as the valorization of steel slag as a precursor to produce AAB.
- Contribution 2: the determination of the rheological model that best describes the behavior of AAB pastes and concretes, besides the discussion of the mixer method's impact on the rheological and mechanical performance of AAB concretes.
- Contribution 3: evaluate the impact of replacing conventional aggregates by steel slag aggregates on the rheological and mechanical properties of the AAB concretes. in addition to the discussion about the accuracy of the current methodologies to assess the durability of alkali-activated concretes.

It is expected that those results will contribute for the development of alkali-activated binders and concretes, as well as other similar composites, contributing to the production of feasible sustainable binders, to support future actions for the management of industrial waste and its destination (fly ash and steel slag) and gradual Portland cement replacement (the major GHG pollutant component of cementitious composites). This kind of development is aligned with the necessity for a more sustainable activity of civil construction.

6.2 Future research suggestions

During this work, many ideas for further development appeared, but could not be implemented yet. Some of them are summarized below:

- Alkali-activated concretes with SS aggregates were classified as heavy concretes due to their high specific gravity and present potential for future studies in the area of radiation-shielding concretes. Investigating the radiation shielding of alkali-

activated materials to different kinds of radiations seems to be an interesting field for research.

- The alkali-activated concretes showed low electrical resistivity compared to conventional concretes. Due to this characteristic, studies involving auto-detection for structural monitoring have the potential to be developed with this material.
- The alkali-activated binders and concretes tested presented high apparent viscosity values, due to the high viscosity of the activators used, especially sodium silicate. This behavior led to concretes with a high flow time, which may jeopardize their commercial application. Thus, new binder formulations, with lower silica modulus and higher alkali contents, should be evaluated to produce lower viscosity binders. New studies in this area can mitigate the rheological problem presented by the material. Thus, studies in this area are recommended. Another approach for rheological optimization of alkali-activated binders and concretes is the testing/formulation of more effective plasticizer admixtures designed specifically to such new kind of concretes. It is known that such kind of admixtures is frequently designed for Portland cement and may not be so effective for AAB.
- The durability indications found in this research were conflicting. The durability measurements based on electrical parameters presented indications of low durability, but the material presented regular porosity and low water penetration under pressure. Therefore, further analysis should be carried out to evaluated the durability of alkali activated concretes.

REFERENCES

ABU-EISHAH, S. I.; EL-DIEB, A. S.; BEDIR, M. S. Performance of concrete mixtures made with electric arc furnace (EAF) steel slag aggregate. **Constr. Build. Mater.**, Amsterdam, v. 34, p. 249-256, 2012, doi.org/10.1016/j.conbuildmat.2012.02.012.

ALCANTARA, M. R. G. **Estudo da utilização de cinzas pesadas de termoelétricas para produção de blocos de concreto para pavimentos intertravados**. 2018. 99 f. Dissertation (Master in Transport Engineering) - Transportation Engineering Department. Federal University of Ceará, Fortaleza, 2018.

ALDAWSARI, S.; KAMPMANN, R.; HARNISCH, J.; ROHDE, C. Setting Time, Microstructure, and Durability Properties of Low Calcium Fly Ash/Slag Geopolymer: A Review. **Materials,** Amsterdam, v. 15, n. 3, p. 876, 2022. Available on: https://doi.org/10.3390/ma15030876. Accessed on: 25 april 2023.

ALIABDO, A. A.; ABD ELMOATY, M.; SALEM, H. A. Effect of cement addition, solution resting time and curing characteristics on fly ash based geopolymer concrete performance. **Constr. Build. Mater.**, Amsterdam, v. 123, p. 581-593, 2016, doi.org/10.1016/j.conbuildmat.2016.07.043.

ALMEIDA, G. M. **Utilização de escória produzida em alto-forno a carvão vegetal como agregado graúdo e miúdo para concreto**. 2014. 135 f. Master thesis (master's in civil engineering) - Institute of Technology, Federal University of Belem, Belém, 2014.

ALNAHHAL, M. F.; KIM, T.; HAJIMOHAMMADI, A. Distinctive rheological and temporal viscoelastic behaviour of alkali-activated fly ash/slag pastes: a comparative study with cement paste. **Cem. Concr. Res.**, Amsterdam, v. 144, p. 106441, 2021. Available on: https:// doi.org/10.1016/j.cemconres.2021.106441. Accessed on: 25 april 2022.

ALNAHHAL, M. F.; HAMDAN, A.; HAJIMOHAMMADI, A.; KIM, T. Effect of rice husk ash-derived activator on the structural build-up of alkali activated materials. **Cem. Concr. Res.**, Amsterdam, v. 150, p. 106590, 2021. Available on: https:// doi.org/10.1016/j.cemconres.2021.106590. Accessed on: 25 april 2022.

ALNAHHAL, M. F.; KIM, T.; HAJIMOHAMMADI, A. **Evolution of flow properties, plastic viscosity, and yield stress of alkali-activated fly ash/slag pastes**. RILEM Tech. Lett., v. 5, p. 141–149, 2020, doi.org/10.21809/rilemtechlett.2020.123.

ALONSO, M. M.; GISMERA, S.; BLANCO, M. T.; LANZÓN, M.; PUERTAS, F. Alkali-activated mortars: Workability and rheological behaviour. **Constr. Build. Mater.**, Amsterdam, v. 145, p. 576-587, 2017, doi.org/10.1016/j.conbuildmat.2017.04.020.

AMANCIO, F. A. **Estudo de propriedades no estado fresco de argamassas de revestimento com escória de aciaria BSSF**. 2019. 87 f. Master thesis (Masters in Civil Engineering) - Structures and Civil Construction Department, Federal University of Ceará, Fortaleza, 2019.

AMERICAN ASSOCIATION OF STATE HIGHWAY AND TRANSPORTATION OFFICIALS, **AASHTO PP 84:** Developing Performance Engineered Concrete Pavement Mixtures. Washington: AASHTO International, 2020.

AMERICAN SOCIETY FOR TESTING AND MATERIALS. **ASTM C39:** Standard Test Method for Compressive Strength of Cylindrical Concrete Specimens. Philadelphia: ASTM International, 2021.

_____**ASTM C94:** Standard Specification for Ready-Mixed Concrete. Philadelphia: ASTM International, 2014.

_____**ASTM C143:** Standard Test Method for Slump of Hydraulic-Cement Concrete. Philadelphia: ASTM International, 2015.

_____**ASTM C191:** Standard Test Methods for Time of Setting of Hydraulic Cement by Vicat Needle. Philadelphia: ASTM International, 2021.

_____**ASTM C215:** Standard Test Method for Fundamental Transverse, Longitudinal, and Torsional Resonant Frequencies of Concrete Specimens. Philadelphia: ASTM International, 2019.

_____**ASTM C348:** Standard Test Method for Flexural Strength of Hydraulic-Cement Mortars. Philadelphia: ASTM International, 2021.

_____**ASTM C349:** Standard Test Method for Compressive Strength of Hydraulic-Cement Mortars. Philadelphia: ASTM International, 2018.

_____**ASTM C469:** Standard Test Method for Static Modulus of Elasticity and Poisson's Ratio of Concrete in Compression. Philadelphia: ASTM International, 2022.

_____**ASTM C597:** Standard Test Method for Pulse Velocity Through Concrete. Philadelphia: ASTM International, 2016.

_____**ASTM C618:** Standard specification for coal fly ash and raw or calcined natural pozzolan for use as a mineral admixture in concrete. Philadelphia: ASTM International, 2019.

_____**ASTM C642:** Standard Test Method for Density, Absorption, and Voids in Hardened Concrete. Philadelphia: ASTM International, 2021.

_____**ASTM C1,202:** Standard Test Method for Electrical Indication of Concrete's Ability to Resist Chloride Ion Penetration. Philadelphia: ASTM International, 2019.

_____**ASTM C1,611:** Standard Test Method for Slump Flow of Self-Consolidating Concrete. Philadelphia: ASTM International, 2010.

_____**ASTM C1,621:** Standard Test Method for Passing Ability of Self-Consolidating Concrete by J-Ring. Philadelphia: ASTM International, 2014.

_____**ASTM C1,876:** Standard Test Method for Bulk Electrical Resistivity or Bulk Conductivity of Concrete1. Philadelphia: ASTM International, 2019.

ASSOCIAÇÃO BRASILEIRA DE NORMAS TÉCNICAS. **ABNT NBR 5,738:** Concreto - Procedimento para moldagem e cura de corpos de prova. Rio de Janeiro: ABNT, 2016.

_____**. ABNT NBR 5,739:** Concreto - Ensaio de compressão de corpos de prova cilíndricos. Rio de Janeiro: ABNT, 2018.

_____**. ABNT NBR 5,751:** Materiais pozolânicos - Determinação da atividade pozolânica com cal aos sete dias. Rio de Janeiro: ABNT, 2015.

_____**. ABNT NBR 7,211:** Agregados para concreto - Especificação. Rio de Janeiro: ABNT, 2019.

_____. **ABNT NBR 7,212:** Concreto dosado em central - Preparo, fornecimento e controle. Rio de Janeiro: ABNT, 2021.

_____. **ABNT NBR 8,522-1:** Concreto endurecido - Determinação dos módulos de elasticidade e de deformação Parte 1: Módulos estáticos à compressão. Rio de Janeiro: ABNT, 2021.

_____. **ABNT NBR 8,802:** Concreto endurecido - Determinação da velocidade de propagação de onda ultrassônica. Rio de Janeiro: ABNT, 2019.

_____. **ABNT NBR 8,953:** Concreto para fins estruturais - Classificação pela massa específica, por grupos de resistência e consistência. Rio de Janeiro: ABNT, 2015.

_____. **ABNT NBR 9,204:** concreto endurecido: determinação da resistividade elétrico-volumétrica: método de ensaio. Rio de Janeiro: ABNT, 2012.

_____. **ABNT NBR 9,778:** Argamassa e concreto endurecidos – Determinação da absorção de água, índice de vazios e massa específica. Rio de Janeiro: ABNT, 2009.

_____. **ABNT 10,787:** Concreto endurecido - Determinação da penetração de água sob pressão. Rio de Janeiro: ABNT, 2011.

_____. **ABNT NBR 12,653:** Materiais pozolânicos - Requisitos. Rio de Janeiro: ABNT, 2014.

_____. **ABNT NBR 12,655:** Concreto de cimento Portland - Preparo, controle, recebimento e aceitação - Procedimento. Rio de Janeiro: ABNT, 2022.

_____**ABNT NBR 13,279:** Argamassa para assentamento e revestimento de paredes e tetos - Determinação da resistência à flexão e à compressão. Rio de Janeiro: ABNT, 2005.

_____. **ABNT NBR 15,630:** Argamassa para assentamento e revestimento de paredes e tetos – Determinação do módulo de elasticidade dinâmico através da propagação de onda ultra-sônica. Rio de Janeiro: ABNT, 2009.

_____. **ABNT NBR 15,823-1:** Concreto autoadensável Parte 1: Classificação, controle e recebimento no estado fresco. Rio de Janeiro: ABNT, 2017.

_____. **ABNT NBR 15,823-2:** Concreto autoadensável Parte 2: Determinação do espalhamento, do tempo de escoamento e do índice de estabilidade visual - Método do cone de Abrams. Rio de Janeiro: ABNT, 2017.

_____. **ABNT NBR 15,823-3:** Concreto autoadensável Parte 3: Determinação da habilidade passante - Método do anel J. Rio de Janeiro: ABNT, 2017.

_____. **ABNT NBR 16,372:** Cimento Portland e outros materiais em pó - Determinação da finura pelo método de permeabilidade ao ar (método de Blaine). Rio de Janeiro: ABNT, 2015.

_____. **ABNT NBR 16,605:** Cimento Portland e outros materiais em pó - Determinação da massa específica. Rio de Janeiro: ABNT, 2017.

_____**. ABNT NBR 16,607:** Cimento Portland - Determinação dos tempos de pega. Rio de Janeiro: ABNT, 2018.

_____. **ABNT NBR 16,889:** Concreto - Determinação da consistência pelo abatimento do tronco de cone. Rio de Janeiro: ABNT, 2020

_____. **ABNT NBR 16,916:** Agregado miúdo - Determinação da densidade e da absorção de água. Rio de Janeiro: ABNT, 2021.

_____. **ABNT NBR 16,917:** Agregado graúdo - Determinação da densidade e da absorção de água. Rio de Janeiro: ABNT, 2021.

_____. **ABNT NBR 16,972:** Agregados - Determinação da massa unitária e do índice de vazios. Rio de Janeiro: ABNT, 2021.

ASSOCIAÇÃO BRASILEIRA DE NORMAS TÉCNICAS, NORMA MERCOSUL. **ABNT NBR NM 248: A**gregados - Determinação da composição granulométrica. Rio de Janeiro: ABNT, 2003.

ATABEY, İ. İ.; KARAHAN, O.; BILIM, C.; ATIŞ, C. D. The influence of activator type and quantity on the transport properties of class F fly ash geopolymer. **Constr. Build. Mater**., Amsterdam, v. 264, p. 120268, 2020. Available on: https://doi.org/10.1016/j.conbuildmat.2020.120268. Accessed on: 25 april 2023.

Average Temperatures - Fortaleza. **National Centers for Environmental Information - NCEI**. 2022: Available on: https://www.ncei.noaa.gov/. Accessed on: 20 jan. 2022.

AZEVEDO, A. G. S.; STRECKER, K. Brazilian fly ash based inorganic polymers production using different alkali activator solutions. **Ceramics International**, Amsterdam, v. 43, n. 12, p. 9012-9018, 2017, doi.org/10.1016/j.ceramint.2017.04.044.

BAIC, I. R.; KOZIOŁ, W.; MIROS, A. Dependence of extraction and production of construction aggregates on selected indicators of economic development in Poland. **Archives of Civil Engin.,** Amsterdam, v. 67, n. 3, p. 437-453, 2021, doi.10.24425/ace.2021.138064.

BENHELAL, E.; ZAHEDI, G.; SHAMSAEI, E.; BAHADORI, A. Global strategies and potentials to curb CO2 emissions in cement industry**. J. Clean. Prod**., Amsterdam, v. 51, p. 142-161, 2012, doi.org/10.1016/j.jclepro.2012.10.049.

BARROS, K. S. **Estudo de Cinzas Volantes de uma Termelétrica da Região Metropolitana de Fortaleza–CE para Aplicação em Camadas Granulares de Pavimentos.** 2015. 143 f. Master thesis (Master in Transport Engineering) - Transportation Engineering Department, Federal University of Ceará, Fortaleza, 2015.

BEUSHAUSEN, H; DITTMER, T. The influence of aggregate type on the strength and elastic modulus of high strength concrete. **Construction and Building Materials**, Amsterdam, v. 74, p. 132-139, 2015. doi.org/10.1016/j.conbuildmat.2014.08.055.

BERNAL, S. A.; DE GUTIÉRREZ, R. M.; PEDRAZA, A. L.; PROVIS, J. L.; RODRIGUEZ, E. D.; DELVASTO, S. Effect of binder content on the performance of alkali-activated slag concretes. **Cem. Concr. Res.**, Amsterdam, v. 41, n. 1, p. 1-8, 2011, doi.org/10.1016/j.cemconres.2010.08.017.

BERNAL, S. A.; PROVIS, J. L. Durability of alkali-activated materials: progress and perspectives. **Journal of the American Ceramic Society**, Amsterdam, v. 97, n. 4, p. 997-1008, 2014, doi.org/10.1111/jace.12831.

BETIOLI, A. M. **Influência dos polímeros MHEC e EVA na hidratação e comportamento reológico de pastas de cimento Portland**. 2007. 178 f. Doctoral

dissertation (Post-graduate program in civil engineering) - Civil Engineering Department, Federal University of Santa Catarina - UFSC. Florianópolis, 2007.

BEZERRA, A. K. L. **Development of a non-destructive test for viscoelastic characterization of asphalt mixtures.** 2023. 84 f. Master thesis (Master in Transport Engineering) - Transportation Engineering Department, Federal University of Ceará, Fortaleza, 2023.

BEZERRA, A. K. L.; MONTEIRO, N. C.; AMARAL, C. C.; COELHO, A. A. D. P; SILVEIRA, J. A. N.; BABADOPULOS, L. F. A. L; SOARES, J. B. Desenvolvimento de ensaio de ressonância por impacto para determinação de rigidez de diferentes materiais. **Transportes**, São Paulo, v. 30., n. 3, p. 2757-2767, 2023, doi.org/10.14295/transportes.v30i3.2757.

BEUSHAUSEN, H; DITTMER, T. The influence of aggregate type on the strength and elastic modulus of high strength concrete. **Construction and Building Materials**, Amsterdam, v. 74, p. 132-139, 2015, doi.org/10.1016/j.conbuildmat.2014.08.055.

BONDAR, D.; NANUKUTTAN, S.; PROVIS, J. L.; SOUTSOS, M. Efficient mix design of alkali activated slag concretes based on packing fraction of ingredients and paste thickness. **J. Clean. Prod**., Amsterdam, v. 218, p. 438-449, 2019, doi.org/10.1016/j.jclepro.2019.01.332.

BOVE, P.; CLAVEAU-MALLET, D.; BOUTET, É.; LIDA, F.; COMEAU, Y. Development and modelling of a steel slag filter effluent neutralization process with CO_2-enriched air from an upstream bioprocess. **Water research**, Amsterdam, v. 129, p. 11-19, 2018, doi.org/10.1016/j.watres.2017.11.005.

BRAZIL STEEL INSTITUTE. **Brasilian steel databook 2021,** Rio de Janeiro, 2021. Available on: https://acobrasil.org.br/site/wp-content/uploads/2021/07/Anuario_Completo_2021.pdf. Accessed on: 20 january 2022.

BRAZIL STEEL INSTITUTE. **Sustainability Report 2018**, 2018, Available on: http://www.acobrasil.org.br/sustentabilidade/. Accessed on: 20 january 2022.

BRIBIÁN, I. Z.; CAPILLA, A. V.; USÓN, A. Life cycle assessment of building materials: comparative analysis of energy and environmental impacts and evaluation of the eco-efficiency improvement potential. **Building And Environment**, Amsterdam, v. 46, n. 5, p. 1133-1140, 2011. Elsevier BV, doi.org/10.1016/j.buildenv.2010.12.002.

CAMPOS, S. A.; RAFAEL, M. F.C.; CABRAL, A. E. B. Evaluation of steel slag of Companhia Siderúrgica do Pecém replacing fine aggregate on mortars. **Procedia Structural Integrity,** Amsterdam, v. 11, p. 145-152, 2018, doi.org/10.1016/j.prostr.2018.11.020.

CHOI, S. C.; LEE, W. K. Effect of Fe_2O_3 on the physical property of geopolymer paste. *In:* Advanced materials research. **Trans Tech Publications Ltd**, Amsterdam, v. 586, p. 126-129, 2012, doi.org/10.4028/www.scientific.net/AMR.586.126.

CAETANO, P. H. C. **Análise do comportamento no estado fresco e endurecido de pastas álcali ativadas à base de cinzas de combustão de carvão mineral e de escória de aciaria**. 2021. 73 f. Undergraduate thesis (Graduation in Civil Engineering), Campus de Crateús, Federal University of Ceará, Crateús, 2021.

CAMPOS, S. A.; RAFAEL, M. F. C.; CABRAL, A. E. B. Evaluation of steel slag of Companhia Siderúrgica do Pecém replacing fine aggregate on mortars. **Procedia Structural Integrity,** Amsterdam, v. 11, p. 145-152, 2018, doi.org/10.1016/j.prostr.2018.11.020.

COSTA. H. N. **Cimentos álcali-ativados à base de cinzas do carvão mineral e de escórias siderúrgicas.** 2022. 217 f. Doctoral dissertation (Engineering and Materials Science Program) - Metallurgical Engineering Department, Federal University of Ceará, Fortaleza, 2022.

CRISTELO, N.; COELHO, J.; MIRANDA, T.; PALOMO, Á; FERNÁNDEZ-JIMÉNEZ, A. Alkali activated composites–An innovative concept using iron and steel slag as both precursor and aggregate. **Cem. Concr. Comp.**, Amsterdam, v. 103, p. 11-21, 2019, doi.org/10.1016/j.cemconcomp.2019.04.024.

CUI, Y.; WANG, D.; **WANG**, Y.; SUN, R.; RUI, Y. Effects of the n (H2O: Na2Oeq) ratio on the geopolymerization process and microstructures of fly ash-based geopolymers**. J. of Non-Crystalline Solids**, Amsterdam, v. 511, p. 19-28, 2019, doi.org/10.1016/j.jnoncrysol.2018.12.033.

DAI, X.; AYDIN, S.; YARDIMCI, M. Y.; LESAGE, K.; SCHUTTER, G., Effects of activator properties and GGBFS/FA ratio on the structural build-up and rheology of AAC. **Cem. Concr. Res.**, Amsterdam, v. 138, p. 106253, 2020. Available on: https://doi.org/10.1016/j.cemconres.2020.106253. Accessed on: 25 april 2023.

DAVIDOVITS, J. Properties of geopolymer cements. *In:* FIRST INTERNATIONAL CONFERENCE ON ALKALINE CEMENTS AND CONCRETES, 1994, Kiev. **Congress proceedings.** Kiev: Kiev State Technical University, 1994. p. 131-147.

DAVIDOVITS, J. **Geopolymer chemistry and applications**. 1 ed. Canberra: Geopolymer Institute, 2008. ISBN: 9782954453118.

DELGADO, J. M. D.; OYEDELE, L.; AJAYI, A.; AKANBI, L.; AKINADE, O.; Bilal, M.; Owolabi, H. Robotics and automated systems in construction: understanding industry-specific challenges for adoption. **J. Build. Eng.**, Amsterdam, v. 26, p. 100868, 2019. Available on: https://doi.org/10.1016/j.jobe.2019.100868. Accessed on: 25 april 2023.

DEMIE, S.; NURUDDIN, M. F.; SHAFIQ, N. Effects of micro-structure characteristics of interfacial transition zone on the compressive strength of self-compacting geopolymer concrete. **Constr. Build. Mater.,** Amsterdam, v. 41, p. 91-98, 2013, doi.org/10.1016/j.conbuildmat.2012.11.067.

DHOBLE, Y. N.; AHMED, S. Review on the innovative uses of steel slag for waste minimization. **Journal of Material Cycles and Waste Management**, Amsterdam, v. 20, n. 3, p. 1373-1382, 2018. doi.10.1007/s10163-018-0711-z.

DIAS, A. R. O. **Avaliação técnica do aproveitamento da escória de aciaria baosteel slag short flow como agregado miúdo na produção de concreto.** 2019. 98 f. Master thesis (Master in Civil Engineering) - Structures and Civil Construction Department, Federal University of Ceará, Fortaleza, 2019.

DING, Y.; DAI, J.-G. SHI, C.-J. Mechanical properties of alkali-activated concrete: A state-of-the-art review. **Constr. Build. Mater.**, Amsterdam, v. 127, p. 68-79, 2016, doi.org/10.1016/j.conbuildmat.2016.09.121.

DING, Y.; SHI, C-J.; LI, N. Fracture properties of slag/fly ash-based geopolymer concrete cured in ambient temperature. **Constr. Build. Mater.**, Amsterdam, v. 190, p. 787-795, 2018, doi.org/10.1016/j.conbuildmat.2018.09.138.

DONATELLO, S.; FERNÁNDEZ-JIMENEZ, A.; PALOMO, A. Very high volume fly ash cements. Early age hydration study using Na_2SO_4 as an activator. **Journal of the American Ceramic Society**, Amsterdam, v. 96, n. 3, p. 900-906, 2013, doi.org/10.1111/jace.12178.

EL HAFID, K.; HAJJAJI, M.; EL HAFID, H. Influence of NaOH concentration on microstructure and properties of cured alkali-activated calcined clay. **Journal of Building Engineering**, Amsterdam, v. 11, p. 158-165, 2017, doi.org/10.1016/j.jobe.2017.04.012.

ELAHI, M. M. A.; HOSSAIN, M. M.; KARIM, M. R.; ZAIN, M. F. M.; SHEARER, C. A review on alkali-activated binders: Materials composition and fresh properties of concrete. **Constr. Build. Mater**., Amsterdam, v. 260, p. 119788, 2020. Available on: https://doi.org/10.1016/j.conbuildmat.2020.119788. Accessed on: 25 april 2023.

ENEVA. **Nossos negócios - Geração de Energia,** 2021. Available on: https://www.eneva.com.br/nossos-negocios/geracao-de-energia/pecem-ii/. Accessed on: 20 jan. 2022.

EUROPEAN FEDERATION OF NATIONAL ASSOCIATIONS REPRESENTING FOR CO NCRETE, EFNARC. **The European Guidelines for Self-Compacting Concrete:** Specification, Production and Use. The European Project Group, Poland, 2005.

EUROPEAN STANDARD. **EN 206:2:** Concrete - Specification, performance, production and conformity. Brussels: EN International, 2021.

EUROPEAN STANDARD. **EN 12390-8:** Testing hardened concrete Depth of penetration of water under pressure. Brussels: EN International, 2019.

FAN, J.; ZHU, H.; SHI, J.; LI, Z.; YANG, S. Influence of slag content on the bond strength, chloride penetration resistance, and interface phase evolution of concrete repaired with alkali activated slag/fly ash. C. **Constr. Build. Mater.**, Amsterdam, v. 263, p. 120639, 2020. Available on: https://doi.org/10.1016/j.conbuildmat.2020.120639. Accessed on: 25 april 2023.

FAROOQ, F.; JIN, X.; JAVED, M. F.; AKBAR, A.; SHAH, M. I.; ASLAM, F.; ALYOUSEF, R. Geopolymer concrete as sustainable material: A state of the art review. **Construction and Building Materials**, Amsterdam, v. 306, p. 124762, 2021. Available on: https://doi.org/10.1016/j.conbuildmat.2021.124762. Accessed on: 25 april 2023.

FAVIER A.; HABERT G.; D'ESPINOSE DE LACAILLERIE, J. B.; ROUSSEL, N., Mechanical properties and compositional heterogeneities of fresh geopolymer pastes. **Cem. Concr. Res.**, Amsterdam, v. 48, p. 9-16, 2013, doi.org/10.1016/j.cemconres.2013.02.001.

FAVIER A.; HOT J.; HABERT G.; ROUSSEL, N.; D'ESPINOSE DE LACAILLERIE, J. B.; Flow properties of MK-based geopolymer pastes. A comparative study with standard Portland cement pastes, **Soft Matter**, Amsterdam, v. 10, p. 1134–1141, 2014, doi.org/10.1039/C3SM51889B.

FERNANDEZ-JIMENEZ, A. M.; PALOMO, A.; LOPEZ, C. H. Engineering properties of alkali-activated fly ash concrete. **ACI Mater. Journal,** Amsterdam, v. 103, n. 2, p. 106-126, 2006.

FERRARIS, C.; MARTYS, N. De la pâte de ciment au béton: modélisation et mesures expérimentales des propriétés rhéologiques. **Proc. Rhéologie Génie Civil et Environment**, Paris, v. 36, p. 10-12, 2001.

GARCÍA-LODEIRO, I.; PALOMO, A.; FERNÁNDEZ-JIMÉNEZ, A.; MACPHEE, D. E. Compatibility studies between NASH and CASH gels. Study in the ternary diagram Na_2O–CaO–Al_2O_3–SiO_2–H_2O. **Cem. Concr. Res.**, Amsterdam, v. 41, n. 9, p. 923-931, 2011, doi.org/10.1016/j.cemconres.2011.05.006.

GEOPOLYMER INSTITUTE. **Geopolymer cement and Geopolymer Concrete.** Austrália, 2015. Available on: https://www.geopolymer.org/applications/geopolymer-cement/. Accessed on: 20 jan. 2022.

GJØRV, O. E. High-strength concrete. *In:* Developments in the Formulation and Reinforcement of Concrete. **Woodhead Publishing,** Sawston, v. 1, p. 153-170, 2008, doi.org/10.1016/B978-0-08-102616-8.00007-1.

GOMES, P. C. C.; BARROS, A. R. **Métodos de dosagem de concreto autoadensável**. São Paulo: Pini, 2009.

GUIMARÃES, R. S. **Análise de Requisitos Técnicos e Econômicos de Pavers de Concreto Geopolimérico.** 2022. 57 f. Undergraduate thesis (Graduation in Civil Engineering) - Civil Engineering Department, Federal University of Ceará, Fortaleza, 2022.

GÜLLÜ, H.; CEVIK, A.; AL-EZZI, K. M.; GÜLSAN, M. E. On the rheology of using geopolymer for grouting: A comparative study with cement-based grout included fly ash and cold bonded fly ash. **Construction and Building Materials**, Amsterdam, v. 196, p. 594-610, 2019, doi.org/10.1016/j.conbuidmat.2018.11.140.

GUO, X.; PAN, X. Mechanical properties and mechanisms of fiber reinforced fly ash–steel slag based geopolymer mortar. **Constr. Build. Mater.,** Amsterdam, v. 179, p. 633-641, 2018, doi.org/10.1016/j.conbuildmat.2018.05.198.

HADI, M. N. S.; ZHANG, H.; PARKINSON, S. Optimum mix design of geopolymer pastes and concretes cured in ambient condition based on compressive strength, setting time and workability. **J. Build. Eng.**, Amsterdam, v. 23, p. 301-313, 2019, doi.org/10.1016/j.jobe.2019.02.006.

HAFID, H.; OVARLEZ, G.; TOUSSAINT, F.; JEZEQUEL, P. H.; ROUSSEL, N. Effect of particle morphological parameters on sand grains packing properties and rheology of model mortars. **Cem. Concr. Res.,** Amsterdam, v. 80, p. 44-51, 2016, doi.org/10.1016/j.cemconres.2015.11.002.

HASANBEIGI, A.; PRICE, L.; LIN, E. Emerging energy-efficiency and CO2 emission-reduction technologies for cement and concrete production: A technical review. **Renewable and Sustainable Energy Reviews,** Amsterdam, v. 16, n. 8, p. 6220-6238, 2012, doi.org/10.1016/j.rser.2012.07.019.

HEMALATHA T.; RAM SUNDAR, K. R.; RAMACHANDRA M. A.; IYER N. R. Influence of mixing protocol on fresh and hardened properties of self-compacting concrete. **Constr. Build. Mater**., Amsterdam, v. 98, p. 119-127, 2015, doi.org/10.1016/j.conbuildmat.2015.08.072.

HOPPE FILHO, J.; MEDEIROS, M. D.; PEREIRA, E.; HELENE, P.; ISAIA, G. C. High-volume fly ash concrete with and without hydrated lime: chloride diffusion coefficient from accelerated test**. J. Mater. in Civil Eng.,** Amsterdam, v. 25, n. 3, p. 411-418, 2013, doi.10.1061/(ASCE)MT.1943-5533.0000596.

HORII, K.; KATO, T.; SUGAHARA, K.; TSUTSUMI, N.; KITANO, Y. Overview of iron/steel slag application and development of new utilization technologies. **Nippon Steel & Sumitomo Technical Report,** Toquio, v. 109, p. 5-11, 2015.

HUSEIEN, G. F.; SAM, A. R. M.; ALYOUSEF, R. Texture, morphology and strength performance of self-compacting alkali-activated concrete: Role of fly ash as GBFS replacement. **Constr. Build. Mater.**, Amsterdam, v. 270, p. 121368, 2021. Available on: https://doi.org/10.1016/j.conbuildmat.2020.121368. Accessed on: 25 april 2023.

IRGENS, F. **Rheology and non-Newtonian fluids**. 4 ed. New York: Springer International Publishing, 2014. ISBN 9783319010533.

ISMAIL, I.; BERNAL, S. A.; PROVIS, J. L.; SAN NICOLAS, R.; HAMDAN, S.; VAN DEVENTER, J. S. Modification of phase evolution in alkali-activated blast furnace slag by the incorporation of fly ash. **Cement and Concrete Composites**, Amsterdam, v. 45, p. 125-135, 2014, doi.org/10.1016/j.cemconcomp.2013.09.006.

JIN, S.; ZHAO, Z.; JIANG, S.; SUN, J.; PAN, H.; JIANG, L. Comparison and summary of relevant standards for comprehensive utilization of fly ash at home and abroad. *In:* IOP Conference Series: Earth and Environmental Science. **IOP Publishing**, v. 1, p. 12006, 2021. Available on: https://doi.10.1088/1755-1315/621/1/012006. Accessed on: 25 april 2023.

JUNAID, M. T.; KAYALI, O.; KHENNANE, A.; BLACK, J. A mix design procedure for low calcium alkali activated fly ash-based concretes. **Constr. Build. Mater**., Amsterdam, v. 79, p. 301-310, 2015, doi.org/10.1016/j.conbuildmat.2015.01.048.

KAI, M.-F.; DAI, J.-G. Understanding geopolymer binder-aggregate interfacial characteristics at molecular level**. Cem. Concr. Res.** Amsterdam, v. 149, p. 106582, 2021. Available on: https://doi.org/10.1016/j.cemconres.2021.106582. Accessed on: 25 april 2023.

KIM. J. H.; NOEMI N.; SHAH S. P. Effect of powder materials on the rheology and formwork pressure of self-consolidating concrete. **Cem. Concr. Comp.,** Amsterdam, v. 34, p. 746-753, 2012, doi.org/10.1016/j.cemconcomp.2012.02.016.

KISSA, E. **Dispersions: characterization, testing, and measurement.** 1. ed. New York: Routledge, 2017. ISBN 9781315141381. Available on: https://www.routledge.com/Dispersions-Characterization-Testing-and-Measurement/Kissa/p/book/9780824719944. Accessed on: 2 april 2023

KNIESS, C. T.; COSTA, P. R.; QUONIAM, L.; SANTOS, A. M. Utilização do resíduo resultante da combustão de carvão mineral em usinas termelétricas na produção de novos materiais: uma análise a partir de artigos científicos e de patentes. **Revista de Gestão Social e Ambiental**, São Paulo, v. 13, n. 1, p. 76-93, 2019, doi.org/10.24857/rgsa.v13i1.1786.

KONDEPUDI, K.; SUBRAMANIAM, K. VL., Rheological characterization of low-calcium fly ash suspensions in alkaline silicate colloidal solutions for geopolymer concrete production. **J. Cleaner Production**, v. 234, p. 690-701, 2019, doi.org/10.1016/j.jclepro.2019.06.124.

KUEHL, H. **Slag cement and process of making the same**. Depositor: Atlas Portland Cement Company U.S. Patent n. 900,939, Deposited on: 03 july 1907. Granted on: 13 out. 1908

LEE, W. H.; CHENG, T. W.; LIN, K. Y.; LIN, K. L.; WU, C. C.; TSAI, C. T. Geopolymer technologies for stabilization of basic oxygen furnace slags and sustainable application as

construction materials. **Sustainability**, Amsterdam, v. 12, n. 12, p. 5002, 2020. Available on: https://doi.org/10.3390/su12125002. Accessed on: 25 april 2023.

LEE, N. K.; LEE, HK. Setting and mechanical properties of alkali-activated fly ash/slag concrete manufactured at room temperature. **Constr. Build. Mater**., Amsterdam, v. 47, p. 1201-1209, 2013, doi.org/10.1016/j.conbuildmat.2013.05.107.

LEE, W. H.; WANG, J. H.; DING, Y. C.; CHENG, T. W. A study on the characteristics and microstructures of GGBS/FA based geopolymer paste and concrete. **Constr. Build. Mater.**, Amsterdam, v. 211, p. 807-813, 2019, doi.org/10.1016/j.conbuildmat.2019.03.291.

LI, N.; SHI, C.; ZHANG, Z.; WANG, H.; LIU, Y. A review on mixture design methods for geopolymer concrete. **Comp, Part B**: **Eng.**, Amsterdam, v. 178, p. 107490, 2019. Available on: https://doi.org/10.1016/j.compositesb.2019.107490. Accessed on: 25 april 2023.

LI, N.; SHI, C.; ZHANG, Z.; ZHU, D.; HWANG, H. J.; ZHU, Y.; SUN, T. A mixture proportioning method for the development of performance-based alkali-activated slag-based concrete. **Cem. Concr. Comp**., Amsterdam, v. 93, p. 163-174, 2018, doi.org/10.1016/j.cemconcomp.2018.07.009.

LI, Z.; THOMAS, R. J.; PEETHAMPARAN S. Alkali-silica reactivity of alkali-activated concrete subjected to ASTM C 1293 and 1567 alkali-silica reactivity tests. **Cem. Concr. Res.**, Amsterdam, v. 123, p. 105796, 2019. Available on: https://doi.org/10.1016/j.cemconres.2019.105796. Accessed on: 25 april 2023.

LIU, W.; LI, H.; ZHU, H.; XU, P. The interfacial adhesion performance and mechanism of a modified asphalt–steel slag aggregate. **Materials**, Amsterdam, v. 13, n. 5, p. 1180, 2020. Available on: https://doi.org/10.3390/ma13051180. Accessed on: 25 april 2023.

LLOYD, R. R.; PROVIS, J. L.; SMEATON, K. J.; VAN DEVENTER, J. S. Spatial distribution of pores in fly ash-based inorganic polymer gels visualised by Wood's metal intrusion. **Microporous and Mesoporous Materials**, Amsterdam, v. 126, n. 2, p. 32-39, 2009, doi.org/10.1016/j.micromeso.2009.05.016.

LU, C.; ZHANG, Z.; SHI, C.; LI, N.; JIAO, D.; YUAN, Q. Rheology of alkali-activated materials: A review. **Cem. Concr. Comp**., Amsterdam, v. 121, p. 104061, 2021. Available on: https://doi.org/10.1016/j.cemconcomp.2021.104061. Accessed on: 25 april 2023.

LUO, Z.; LI, W.; WANG, K.; CASTEL, A.; SHAH, S. P. Comparison on the properties of ITZs in fly ash-based geopolymer and Portland cement concretes with equivalent flowability. **Cem. Concr. Res.**, Amsterdam, v. 143, p. 106392, 2021. Available on: https://doi.org/10.1016/j.cemconres.2021.106392. Accessed on: 25 april 2023.

MA, X.; ZHANG, Z.; WANG, A. The transition of fly ash-based geopolymer gels into ordered structures and the effect on the compressive strength. **Constr. and Build. Mater.**, Amsterdam, v. 104, p. 25-33, 2016, doi.org/10.1016/j.conbuildmat.2015.12.049.

MA, G.; YAN, Y.; ZHANG, M.; SANJAYAN, J. Effect of Steel Slag on 3d Concrete Printing of Geopolymer with Quaternary Binders. **Ceramics International,** Amsterdam, v. 48, n. 18, p. 26233-26247, 2016, doi.org/10.1016/j.ceramint.2022.05.305.

MANDEL J. **Cours de Mécanique des Milieux Continus, Tome II:** Mécanique des Solides. Paris: Gauthier-Villars Editeur, 1966.

MANSO, J. M.; ORTEGA-LÓPEZ, V.; POLANCO, J. A.; SETIÉN, J. The use of ladle furnace slag in soil stabilization. **Construction and Building Materials**, Amsterdam, v. 40, p. 126-134, 2013, doi.10.1016/j.conbuildmat.2012.09.079.

MARVILA, M. T.; AZEVEDO, A. R. G.; VIEIRA, C. M. F. Reaction mechanisms of alkali-activated materials. **Revista IBRACON de Estruturas e Materiais**, São Paulo, v. 14, p. 1-14, 2021, doi.org/10.1590/S1983-41952021000300009.

MAZER, W.; LIMA, M. G.; MEDEIROS-JUNIOR, R. A. MEDEIROS-JUNIOR, L. F. S. Chloride ingress into concrete under different conditions of temperature and marine zones. **Magazine of Concrete Research,** Amsterdam, v. 73, n. 22, p. 1180-1188, 2020, doi.org/10.1680/jmacr.19.00451.

MEHDIZADEH H.; KANI E. N. Rheology and apparent activation energy of alkali activated phosphorous slag. **Constr. Build. Mater.**, Amsterdam, v. 171, p.197–204, 2018, doi.org/10.1016/j.conbuildmat.2018.03.130.

MEHTA, P. Kumar; MONTEIRO, Paulo JM. Concrete: **Microstructure, properties, and materials.** 4. ed. São Paulo: McGraw-Hill Education, 2014. ISBN 978-0-07-179788-7.

MEHTA, A.; SIDDIQUE, R.; OZBAKKALOGLU, T.; SHAIKH, F. U. A.; BELARBI, R. Fly ash and ground granulated blast furnace slag-based alkali-activated concrete: Mechanical, transport and microstructural properties. **Constr. Build. Mater.**, Amsterdam, v. 257, p. 119548, 2020. Available on: https://doi.org/10.1016/j.conbuildmat.2020.119548. Accessed on: 25 april 2023.

METWALLY, K. A.; FARIED, A. S.; TAWFIK, T. A.; Significance of blast furnace as coarse aggregate in concrete. **Life Science Journal,** Amsterdam, v. 14, n.9, p. 1-6, 2017, doi.10.7537/marslsj140917.01.

MOREIRA, M. A. M. **Avaliação da trabalhabilidade de pastas cimentícias álcali-ativadas com uso de aditivos tensoativos** 2022. 61 f. Undergraduate thesis, (Graduation in Civil Engineering) - Civil Engineering Department, Federal University of Ceará, Crateús, 2022.

MOHAMMEDAMEEN, A. Performance of Alkali-Activated Self-Compacting Concrete with Incorporation of Nanosilica and Metakaolin. **Sustainability**, Amsterdam, v. 14, n. 11, p. 6572, 2022. Available on: https://doi.org/10.3390/su14116572. Accessed on: 25 april 2023.

MOHAMMED, S. I.; NAJIM, K. B. Mechanical strength, flexural behavior and fracture energy of Recycled Concrete Aggregate self-compacting concrete. **Structures**, Amsterdam, v. 23, p. 34-43, 2020, doi.org/10.1016/j.istruc.2019.09.010.

MYERS, R. J.; BERNAL, S. A.; SAN NICOLAS, R.; PROVIS, J. L. Generalized structural description of calcium–sodium aluminosilicate hydrate gels: the cross-linked substituted tobermorite model. **Langmuir**, Amsterdam, v. 29, n. 17, p. 5294-5306, 2013.

NAGARAJ, V. K.; VENKATESH BABU, D. L. Assessing the performance of molarity and alkaline activator ratio on engineering properties of self-compacting alkaline activated concrete at ambient temperature. **J. Build. Eng**., Amsterdam, v. 20, p. 137-155, 2018, doi.org/10.1016/j.jobe.2018.07.005,

NAIDU, T. S.; SHERIDAN, C. M.; VAN DYK, L. D. Basic oxygen furnace slag: Review of current and potential uses. **Minerals Engineering,** Amsterdam, v. 149, p. 106234, 2020. Available on: https://doi.org/10.1016/j.mineng.2020.106234. Accessed on: 25 april 2023.

NATH, P.; SARKER, P. K. Effect of GGBFS on setting, workability and early strength properties of fly ash geopolymer concrete cured in ambient condition. **Constr. Build. Mater.**, Amsterdam, v. 66, p. 163-171, 2014, doi.org/10.1016/j.conbuildmat.2014.05.080.

NATH, P.; SARKER, P. K. Flexural strength and elastic modulus of ambient-cured blended low-calcium fly ash geopolymer concrete. **Constr. Build. Mater.**, Amsterdam, v. 130, p. 22-31, 2017, doi.org/10.1016/j.conbuildmat.2016.11.034.

NATIONAL ASSOCIATION OF AGGREGATE PRODUCERS FOR CONSTRUCTION. Perspectives for the aggregates sector. **Revista Areia e Arita**. São Paulo, v.69, p. 1-44, 2016. Available on: https://www.anepac.org.br/index.php. Accessed on: 20 jan. 2022.

NĚMEČEK, J.; ŠMILAUER, V.; KOPECKÝ, L. Nanoindentation characteristics of alkali-activated aluminosilicate materials. **Cem. Concr. Comp.**, Amsterdam, v. 33, n. 2, p. 163-170, 2011, doi.org/10.1016/j.cemconcomp.2010.10.005.

NEIVILLE, A. M.; BROOKS J. J. **Concrete technology: update**. 2. ed. Singapura: Pearson, 1997. ISBN 0-582-98859-4.

NGUYEN, K. T.; AHN, N.; LE, T. A.; LEE, K. Theoretical and experimental study on mechanical properties and flexural strength of fly ash-geopolymer concrete. **Constr. Build. Mater.**, Amsterdam, v. 106, p. 65-77, 2016, doi.org/10.1016/j.conbuildmat.2015.12.033.

NOUSHINI A.; CASTEL, A.; ALDRED, J.; RAWAL A. Chloride diffusion resistance and chloride binding capacity of fly ash-based geopolymer concrete. **Cem. Concr. Comp.**, Amsterdam, v. 105, p. 103290, 2020. Available on: https://doi.org/10.1016/j.cemconcomp.2019.04.006. Accessed on: 25 april 2023.

NOUSHINI, A.; CASTEL, A. The effect of heat-curing on transport properties of low-calcium fly ash-based geopolymer concrete. **Constr. Build. Mater.**, Amsterdam, v. 112, p. 464-477, 2016, doi.org/10.1016/j.conbuildmat.2016.02.210.

NUNES, V. A.; BORGES, P. H. R. Recent advances in the reuse of steel slags and future perspectives as binder and aggregate for alkali-activated materials. **Constr. Build. Mater.**, Amsterdam, v. 281, p. 122605, 2021. Available on: https://doi.org/10.1016/j.conbuildmat.2021.122605. Accessed on: 25 april 2023.

NATIONAL UNION OF THE CEMENT INDUSTRY. Numbers of the industry: national production of cement by regions and states, 2020. Available o: https//www.snic.org.br/numeros-industria.php. Accessed on: 10 jan. 2022.

O'REILLY, D.V. **Método de Dosagem de Concreto de Elevado Desempenho**, 1. ed. São Paulo: PINI, 1998.

PALACIOS M.; BANFILL P.F.; PUERTAS F. Rheology and setting of alkali-activated slag pastes and mortars: effect of organic admixture, **ACI Mater. J.**, Amsterdam, v. 105, n. 2, p. 140-148, 2008, MS No. M-2006-442.R3.

PALACIOS, M.; GISMERA, S.; ALONSO, M. D. M.; DE LACAILLERIE, J. D. E.; LOTHENBACH, B.; FAVIER, A.; PUERTAS, F. Early reactivity of sodium silicate-activated slag pastes and its impact on rheological properties. **Cem. Concr. Res.**, Amsterdam, v. 140, p. 106302, 2021. Available on: https://doi.org/10.1016/j.cemconres.2020.106302. Accessed on: 25 april 2023.

PALANKAR, N.; SHANKAR, A. U.; MITHUN, B. M. Investigations on Alkali-Activated Slag/Fly Ash Concrete with steel slag coarse aggregate for pavement structures. **Inter. J. Pav. Eng.**, Amsterdam, v. 18, p. 500-512, 2017, doi.org/10.1080/10298436.2015.1095902.

PALANKAR, N.; SHANKAR, A. U. R.; MITHUN, B. M. Studies on eco-friendly concrete incorporating industrial waste as aggregates. **Inter. J. Sust. Built. Env.**, Amsterdam, v. 4, n. 2, p. 378-390, 2015, doi.org/10.1016/j.ijsbe.2015.05.002.

PAVITHRA, P. E.; REDDY, M. S.; DINAKAR, P.; RAO, B. H.; SATPATHY, B. K.; MOHANTY, A. N. A mix design procedure for geopolymer concrete with fly ash. **J. Clean. Prod.**, Amsterdam, v. 133, p. 117-125, 2016, doi.org/10.1016/j.jclepro.2016.05.041.

PRADHAN, P.; PANDA, S.; PARHI, S. K.; PANIGRAHI, S. K. Factors affecting production and properties of self-compacting geopolymer concrete - A review. **Constr. Build. Mater.**, Amsterdam, v. 344, p. 128174, 2022. Available on: https://doi.org/10.1016/j.conbuildmat.2022.128174. Accessed on: 25 april 2023.

PROVIS, J. L.; BERNAL, S. A. Geopolymers and related alkali-activated materials. **Annual Review of Materials Research,** Amsterdam, v. 44, p. 299-327, 2014, doi.org/10.1146/annurev-matsci-070813-113515.

PROVIS, J. L.; VAN DEVENTER, J. S. **Alkali activated materials:** state-of-the-art report, RILEM TC 224-AAM. Berlin: Springer Science & Business Media, 2013.

PROVIS, J. L.; VAN DEVENTER, J. S. Geopolymers and other alkali-activated materials. *In:* Lea's Chemistry of Cement and Concrete. **Elsevier,** Netherlands, v. 5, p. 779–805, 2019, doi.org/10.1016/B978-0-08-100773-0.00016-2

PROVIS, J. L. Geopolymers and other alkali activated materials: why, how, and what?. **Materials and structures**, Amsterdam, v. 47, n. 1, p. 11-25, 2014, doi.org/10.1617/s11527-013-0211-5.

PUERTAS, F.; VARGA, C.; ALONSO, M. M. Rheology of alkali-activated slag pastes. Effect of the nature and concentration of the activating solution. **Cem. Concr. Res.**, Amsterdam, v. 53, p. 279-288, 2014, doi.org/10.1016/j.cemconcomp.2014.07.012.

PUERTAS, F.; GONZÁLEZ-FONTEBOA, B.; GONZÁLEZ-TABOADA, I.; ALONSO, M. M.; TORRES-CARRASCO, M.; ROJO, G.; MARTÍNEZ-ABELLA F. Alkali-activated slag concrete: Fresh and hardened behaviour. **Cem. Concr. Comp.**, Amsterdam, v. 85, p. 22-31, 2018, doi.org/10.1016/j.cemconcomp.2017.10.003.

RAFEET, A.; VINAI, R.; SOUTSOS, M.; SHA, W. Guidelines for mix proportioning of fly ash/GGBS based alkali activated concretes. **Constr. Build. Mater.**, Amsterdam, v. 147, p. 130-142, 2017, doi.org/10.1016/j.conbuildmat.2017.04.036.

RAMANATHAN, P.; BASKAR, I.; MUTHUPRIYA, P.; VENKATASUBRAMANI, R. Performance of self-compacting concrete containing different mineral admixtures. **KSCE journal of Civil Engineering**, Amsterdam, v. 17, p. 465-472, 2013, doi.org/10.1007/s12205-013-1882-8.

RASHAD, A. M.; KHAFAGA, S. A.; GHARIEB, M. Valorization of fly ash as an additive for electric arc furnace slag geopolymer cement. **Constr. Build. Mater.** Amsterdam, v. 294, p. 123570, 2021. Available on: https://doi.org/10.1016/j.conbuildmat.2021.123570. Accessed on: 25 april 2023.

REVATHI, T.; JEYALAKSHMI, R., Fly ash–GGBS geopolymer in boron environment: A study on rheology and microstructure by ATR FT-IR and MAS NMR. **Constr. Build. Mater.**, Amsterdam, v. 267, p. 120965, 2021. Available on: https://doi.org/10.1016/j.conbuildmat.2020.120965. Accessed on: 25 april 2023.

RIFAAI, Y.; YAHIA, A.; MOSTAFA, A.; AGGOUN, S.; KADRI, E. H. Rheology of fly ash-based geopolymer: Effect of NaOH concentration. **Constr. Build. Mater.**, Amsterdam, v. 223, p. 583-594, 2019, doi.org/10.1016/j.conbuildmat.2019.07.028.

ROHDE, G. M.; MACHADO, C. S. Quantificação das cinzas de carvão fóssil produzidas no Brasil. **Boletim Técnico**, São Paulo, v. 36, p. 1-57, 2016.

ROUSSEL, N. **Understading the Rheology of Concrete**. 1. ed. Sawston: Woodhead Publishing Limited, 2011. ISBN 9780857095282.

ROUYER, J.; POULESQUEN, A. Evidence of a fractal percolating network during geopolymerization. **Journal of the American Ceramic Society**, Amsterdam, v. 98, p. 1580-1587, 2015, doi.org/10.1111/jace.13480.

SAINI, G.; VATTIPALLI, U. Assessing properties of alkali activated GGBS based self-compacting geopolymer concrete using nano-silica. **Case Studies in Constr. Mater.**, Amsterdam, v. 12, p. 00352, 2020. Available on: https://doi.org/10.1016/j.cscm.2020.e00352. Accessed on: 25 april 2023.

SANTOS, S.; SILVA, P. R.; BRITO, J. (2019). Self-compacting concrete with recycled aggregates–a literature review**. J. Build. Eng.**, Amsterdam, v. 22, p. 349-371, doi.org/10.1016/j.jobe.2019.01.001.

SCHRAMM, G. **Reologia e reometria: fundamentos teóricos e práticos.** São Paulo: Artliber Editora, 2006. ISBN 13 9788588098343.

SHI, C. Corrosion resistance of alkali-activated slag cement**. Adv Cem Res.,** Amsterdam, 2003. https://doi.org/10.1680/adcr.2003.15.2.77. Accessed on: 25 april 2023.

SILVA, W. K. D. **Caracterização de escórias de aciaria e avaliação do seu uso na produção de argamassa de revestimento.** 2018. 72 f. Undergraduate thesis, (Graduation in Civil Engineering) - Civil Engineering Department, Federal University of Ceará, Fortaleza, 2018.

SINGH, N. B.; MIDDENDORF, B. Geopolymers as an alternative to Portland cement: An overview. **Constr. Build. Mater.**, Amsterdam, v. 237, p. 117455, 2019. Available on: https://doi.org/10.1016/j.conbuildmat.2019.117455. Accessed on: 25 april 2023.

SINGH, J.; SINGH, S. P. Geopolymerization of solid waste of non-ferrous metallurgy–A review. **Journal of environmental management**, Amsterdam, v. 251, p. 109571, 2019. Available on: https://doi.org/10.1016/j.jenvman.2019.109571. Accessed on: 25 april 2023.

SONG, W.; ZHU, Z.; PENG, Y.; WAN, Y.; XU, X.; PU, S.; SONG, S.; WEI, Y. Effect of steel slag on fresh, hardened and microstructural properties of high-calcium fly ash based geopolymers at standard curing condition. **Constr. Build. Mater.**, Amsterdam, v. 229, p. 116933, 2019. Available on: https://doi.org/10.1016/j.conbuildmat.2019.116933. Accessed on: 25 april 2023.

SOUZA, T. V. P. **Caracterização de escória de conversor a oxigênio obtida no processo BSSF antes e após tratamento hidrometalúrgico**. 2016. 62 f. Master thesis (Master in

Science of Materials) - Structures and Civil Construction Department, Federal University of Ceará, Fortaleza, 2016.

SUMESH, M.; ALENGARAM, U. J.; JUMAAT, M. Z.; MO, K. H.; ALNAHHAL, M. F. Incorporation of nano-materials in cement composite and geopolymer based paste and mortar–A review. **Constr. Build. Mater.**, Amsterdam, v. 148, p. 62-84, 2017, doi.org/10.1016/j.conbuildmat.2017.

SOUTSOS, M.; BOYLE, A. P.; VINAI, R.; HADJIERAKLEOUS, A.; BARNETT, S. J. Factors influencing the compressive strength of fly ash based geopolymers. **Constr. Build. Mater.**, Amsterdam, v. 110, p. 355-368, 2016, doi.org/10.1016/j.conbuildmat.2015.11.045.

TAN, Z.; BERNAL, S. A.; PROVIS, J. L. Reproducible mini-slump test procedure for measuring the yield stress of cementitious pastes. **Mater. and Struct.**, Amsterdam, v. 50, n. 6, p. 1-12, 2017, doi:10.1617/s11527-017-1103-x.

THE ZEOBOND GROUP. **Projects: e-crete pre-mixed concrete.** 2022. Available on: https://www.zeobond.com/projects-rd-e-crete.html. Accessed on: 10 jan. 2022.

THOMAS, R. J.; PEETHAMPARAN, S. Stepwise regression modeling for compressive strength of alkali-activated concrete. **Constr. Build. Mater.**, Amsterdam, v. 141, p. 315-324, 2017, doi.org/10.1016/j.conbuildmat.2017.03.006.

TIAN, Z.; ZHANG, Z.; LIU, H.; ZHENG, W.; TANG, X.; GUI, Z. Interfacial characteristics and mechanical behaviors of geopolymer binder with steel slag aggregate. **J. Clean. Prod.**, Amsterdam, v. 27, p. 132385, 2022. Available on: https://doi.org/10.1016/j.jclepro.2022.132385. Accessed on: 25 april 2023.

TRINDADE, E. L.; LIMA, L. R.; ALENCAR, L. H.; ALENCAR, M. H. Identification of obstacles to implementing sustainability in the civil construction industry using bow-tie tool. **Building**, Amsterdam, v. 10, n. 9, p. 165-175, 2020, doi.org/10.3390/buildings1009016.

TIBBETTS, C. M.; PARIS, J. M.; FERRARO, C. C.; RIDING, K. A.; TOWNSEND, T. G. Relating water permeability to electrical resistivity and chloride penetrability of concrete containing different supplementary cementitious materials. **Cem. and Concr. Comp.**, Amsterdam, v. 107, p. 103491, 2020. Available on: https://doi.org/10.1016/j.cemconcomp.2019.103491. Accessed on: 25 april 2023

VANCE, K.; DAKHANE, A.; SANT, G.; NEITHALATH, N. Observations on the rheological response of alkali activated fly ash suspensions: the role of activator type and concentration. **Rheologica Acta**, Amsterdam, v. 53, p. 843-855, 2014, doi.org/10.1007/s00397-014-0793-z.

XIE, J.; KAYALI, O. Effect of superplasticiser on workability enhancement of Class F and Class C fly ash-based geopolymers. **Constr. Build. Mater.**, Amsterdam, v. 122, p. 36-42, 2016, doi.org/10.1016/j.conbuildmat.2016.06.067.

XIE, T.; VISINTIN, P.; ZHAO, X.; GRAVINA, R. Mix design and mechanical properties of geopolymer and alkali activated concrete: Review of the state-of-the-art and the development of a new unified approach. **Constr. Build. Mater.**, Amsterdam, v. 256, p. 119380, 2020. Available on: https://doi.org/10.1016/j.conbuildmat.2020.119380. Accessed on: 25 april 2023

YANG, K. H.; SONG, J. K.; SONG, K. I. Assessment of CO2 reduction of alkali-activated concrete. **J. Clean. Prod.**, Amsterdam, v. 39, p. 265-272, 2012, doi.org/10.1016/j.jclepro.2012.08.001.

YI, H.; XU, G.; CHENG, H.; WANG, J.; WAN, Y.; CHEN, H. An overview of utilization of steel slag. **Procedia Environmental Sciences**, Amsterdam, v. 16, p. 791-801, 2012, doi.org/10.1016/j.proenv.2012.10.108.

YUAN, Q.; LU, X.; KHAYAT, K. H.; FEYS, D.; SHI, C. Small amplitude oscillatory shear technique to evaluate structural build-up of cement paste, **Mater. Struct.**, Amsterdam, v. 50, p. 1-12, 2017, doi.org/10.1617/s11527-016-0978-2.

YUSUF, M. O.; JOHARI, M. A. M.; AHMAD, Z. A.; MASLEHUDDIN, M. Evolution of alkaline activated ground blast furnace slag–ultrafine palm oil fuel ash based concrete. **Materials & Design**, Amsterdam, v. 55, p. 387-393, 2014, doi.org/10.1016/j.matdes.2013.09.047.

WALKLEY, B.; SAN NICOAS, R.; SANI, M. A.; REES, G. J.; HANNA, J. V.; VAN DEVENTER, J. S.; PROVIS, J. L. Phase evolution of C-(N)-ASH/NASH gel blends investigated via alkali-activation of synthetic calcium aluminosilicate precursors. **Cem. Concr. Res.,** Amsterdam, v. 89, p. 120-135, 2016, doi.org/10.1016/j.cemconres.2016.08.010.

WAQAS, R. M.; BUTT, F.; ZHU, X.; JIANG, T.; TUFAIL, R. F. A Comprehensive Study on the Factors Affecting the Workability and Mechanical Properties of Ambient Cured Fly Ash and Slag Based Geopolymer Concrete. **Applied Sciences,** Amsterdam, v. 11, n. 18, p. 8722, 2021. Available on: https://doi.org/10.3390/app11188722. Accessed on: 25 april 2023.

WALKLEY, B.; REES, G. J.; SAN NICOLAS, R.; VAN DEVENTER, J. S.; HANNA, J. V.; PROVIS, J. L. New structural model of hydrous sodium aluminosilicate gels and the role of charge-balancing extra-framework Al. **The Journal of Physical Chemistry C**, Amsterdam, v. 122, n. 10, p. 5673-5685, 2018, doi.org/10.1021/acs.jpcc.8b00259.

WANG, G. C. Ferrous metal production and ferrous slags. *In:* The utilization of slag in civil infrastructure construction. **Woodhead Publishing Cambridge**, Sawston, 2016, doi.org/10.1016/B978-0-08-100381-7.00002-1

WANG, Y. S.; ALREFAEI, Y.; DAI, J. G. Silico-aluminophosphate and alkali-aluminosilicate geopolymers: A comparative review. **Frontiers in Materials**, Amsterdam, v. 6, p. 106, 2019. Available on: https://doi.org/10.3389/fmats.2019.00106. Accessed on: 25 april 2023.

WIMMER, G.; WULFERT, H.; FLEISCHANDERL, A.; WERNER, A.; FENZL, T. BOF converter slag valorization. **AISTech iron steel tech. conf. exhibit**. Ohio, p. 297-303, 2014.

WONGPA, J.; KIATTIKOMOL, K.; JATURAPITAKKUL, C.; CHINDAPRASIRT, P. Compressive strength, modulus of elasticity, and water permeability of inorganic polymer concrete. **Materials & Design**, Amsterdam, v. 31, n. 10, p. 4748-4754, 2010, doi.org/10.1016/j.matdes.2010.05.012.

WORLD STEEL ASSOCIATION. **2021 global crude steel production**, 2021. Available on: https://worldsteel.org/media-centre/press-releases/2022/december-2021-crude-steel-production-and-2021-global-totals. Accessed on: 20 jan. 2022.

ZERZOURI, M.; BOUCHENAFA, O.; HAMZAOUI, R.; ZIYANI, L.; ALEHYEN, S. Physico-chemical and mechanical properties of fly ash based-geopolymer pastes produced from pre-geopolymer powders obtained by mechanosynthesis. **Constr. Build. Mater.**, Amsterdam, v. 288, p. 123-135, 2021. Available on: https://doi.org/10.1016/j.conbuildmat.2021.123135. Accessed on: 25 april 2023.

ZHANG, L.; AHMARI, S.; ZHANG, J. Synthesis and characterization of fly ash modified mine tailings-based geopolymers. **Constr. Build. Mater.**, Amsterdam, v. 25, p. 3773–3781, 2011, doi.org/10.1016/j.conbuildmat.2011.04.005.

ZHANG, Z.; WANG, H. Analysing the relation between pore structure and permeability of alkali-activated concrete binders. **Handbook of Alkali-Activated Cements, Mortars and Concretes,** Sawston, p. 235-264, 2015, doi.org/10.1533/9781782422884.2.235.

ZHANG, J.; SHI, C.; ZHANG, Z.; OU, Z. Durability of alkali-activated materials in aggressive environments: a review on recent studies. **Constr. Build. Mater**., Amsterdam, v. 152, p. 598-613. 2017, doi.org/10.1016/j.conbuildmat.2017.07.027.

ZHANG, P.; WANG, K.; LI, Q.; WANG, J.; LING, Y. Fabrication and engineering properties of concretes based on geopolymers/alkali-activated binders-A review. **J. Clean. Prod.**, Amsterdam, v. 258, p. 120896, 2020. Available on: https://doi.org/10.1016/j.jclepro.2020.120896. Accessed on: 25 april 2023.

ZHANG, P.; ZHENG, Y.; WANG, K.; ZHANG, J. A review on properties of fresh and hardened geopolymer mortar. **Composites Part B: Engineering**, Amsterdam, v. 152, p. 79-95, 2018, doi.org/10.1016/j.compositesb.2018.06.031.

ZHU, X.; LI, W.; DU, Z.; ZHOU, S.; ZHANG, Y.; LI, F. Recycling and utilization assessment of steel slag in metakaolin based geopolymer from steel slag by-product to green geopolymer. **Constr. Build. Mater.**, Amsterdam, v. 305, p. 124654, 2021. Available on: https://doi.org/10.1016/j.conbuildmat.2021.124654. Accessed on: 25 april 2023.

APPENDIX A - RESULTS OF THE ALKALI-ACTIVATED MIXTURES

Table A.1 - Complete results of AABs compressive strengths at 28 days, ambient curing

ID	Silica Modulus (adim.)	Alkali Content (%)	Compr. strength (MPa)	FA-SS mass ratio (%)	ID	Silica Modulus (adim.)	Alkali Content (%)	Compr. strength (MPa)	FA-SS mass ratio (%)
1	0.75	6	73.03		37	0.75	6	71.73	
2	0.75	6	67.77		38	0.75	6	71.93	
3	0.75	6	67.67		39	0.75	6	69.26	
4	0.75	6	75.34		40	0.75	6	69.06	
5	0.75	8	61.74		41	0.75	8	50.08	
6	0.75	8	64.84		42	0.75	8	53.22	
7	0.75	8	63.64		43	0.75	8	54.72	
8	0.75	8	67.91		44	0.75	8	48.18	
9	0.75	10	54.94		45	0.75	10	34.25	
10	0.75	10	50.03		46	0.75	10	34.66	
11	0.75	10	52.21		47	0.75	10	36.96	
12	0.75	10	49.39		48	0.75	10	42.22	
13	1.25	6	52.51		49	1.25	6	55.90	
14	1.25	6	59.04		50	1.25	6	54.87	
15	1.25	6	53.27		51	1.25	6	56.98	
16	1.25	6	54.18		52	1.25	6	56.70	
17	1.25	8	54.11		53	1.25	8	49.93	
18	1.25	8	51.31	75-25	54	1.25	8	43.50	50-50
19	1.25	8	49.88		55	1.25	8	49.71	
20	1.25	8	54.06		56	1.25	8	46.82	
21	1.25	10	36.04		57	1.25	10	38.07	
22	1.25	10	38.27		58	1.25	10	39.71	
23	1.25	10	44.05		59	1.25	10	38.07	
24	1.25	10	-		60	1.25	10	39.71	
25	1.75	6	63.49		61	1.75	6	51.17	
26	1.75	6	**56.26**		62	1.75	6	51.12	
27	1.75	6	66.21		63	1.75	6	45.43	
28	1.75	6	69.32		64	1.75	6	50.23	
29	1.75	8	39.51		65	1.75	8	32.62	
30	1.75	8	33.48		66	1.75	8	37.76	
31	1.75	8	40.42		67	1.75	8	33.04	
32	1.75	8	38.74		68	1.75	8	36.41	
33	1.75	10	49.13		69	1.75	10	35.90	
34	1.75	10	41.08		70	1.75	10	37.12	
35	1.75	10	41.59		71	1.75	10	33.95	
36	1.75	10	50.32		72	1.75	10	40.28	

Table A.2 - Complete results of AABs compressive strengths at 28 days, thermal curing

ID	Silica Modulus (adim.)	Alkali Content (%)	Compr. strength (MPa)	FA-SS mass ratio (%)	ID	Silica Modulus (adim.)	Alkali Content (%)	Compr. strength (MPa)	FA-SS mass ratio (%)
73	0.75	6	77.85		100	0.75	6	61.41	
74	0.75	6	76.62		101	0.75	6	67.46	
75	0.75	6	**85.95**		102	0.75	6	66.83	
76	0.75	8	77.64		103	0.75	8	55.22	
77	0.75	8	76.42		104	0.75	8	60.92	
78	0.75	8	74.95		105	0.75	8	61.84	
79	0.75	10	63.36		106	0.75	10	41.12	
80	0.75	10	63.10		107	0.75	10	45.33	
81	0.75	10	66.35		108	0.75	10	48.29	
82	1.25	6	53.00		109	1.25	6	58.07	
83	1.25	6	57.18		110	1.25	6	65.95	
84	1.25	6	60.72		111	1.25	6	61.95	
85	1.25	8	58.78		112	1.25	8	47.65	
86	1.25	8	60.76	75-25	113	1.25	8	54.72	50-50
87	1.25	8	61.63		114	1.25	8	49.73	
88	1.25	10	52.92		115	1.25	10	54.43	
89	1.25	10	61.76		116	1.25	10	53.45	
90	1.25	10	55.74		117	1.25	10	48.55	
91	1.75	6	54.97		118	1.75	6	54.79	
92	1.75	6	57.16		119	1.75	6	52.44	
93	1.75	6	51.22		120	1.75	6	50.34	
94	1.75	8	39.24		121	1.75	8	26.21	
95	1.75	8	35.78		122	1.75	8	26.63	
96	1.75	8	34.95		123	1.75	8	31.54	
97	1.75	10	44.10		124	1.75	10	29.10	
98	1.75	10	45.35		125	1.75	10	26.38	
99	1.75	10	41.42		126	1.75	10	30.89	

Table A.3 - Complete result of the flexural strength at 28 of the AABs, ambient curing

ID	Silica Modulus (adim.)	Alkali Content (%)	Compr. strength (MPa)	FA-SS mass ratio (%)	ID	Silica (adim.)	Alkali Content (%)	Compr. strength (MPa)	FA-SS mass ratio (%)
1	0.75	6	5.2		19	0.75	6	4.4	
2	0.75	6	5.4		20	0.75	6	4.8	
3	0.75	8	4.7		21	0.75	8	2.4	
4	0.75	8	4.5		22	0.75	8	2.9	
5	0.75	10	3.9		23	0.75	10	3.7	
6	0.75	10	3.5		24	0.75	10	3.6	
7	1.25	6	5		25	1.25	6	3.8	
8	1.25	6	5.1		26	1.25	6	3.9	
9	1.25	8	3.7	75-25	27	1.25	8	3.7	50-50
10	1.25	8	4.4		28	1.25	8	4.8	
11	1.25	10	2.7		29	1.25	10	3.4	
12	1.25	10	2.7		30	1.25	10	4.1	
13	1.75	6	4.3		31	1.75	6	5.1	
14	1.75	6	4.6		32	1.75	6	5.0	
15	1.75	8	3.7		33	1.75	8	4.9	
16	1.75	8	4.4		34	1.75	8	4.6	
17	1.75	10	1.8		35	1.75	10	3.9	
18	1.75	10	2.5		36	1.75	10	3.3	

Table A.4 - Abbreviations used for statistical analysis

Parameter name	Abbreviation	Corresponding Value
Silica modulus (adm.)	S/N 1	0.75
Silica modulus (adm.)	S/N 2	1.25
Silica modulus (adm.)	S/N 3	1.75
Alkali Content (%)	N% 1	6
Alkali Content (%)	N% 2	8
Alkali Content (%)	N% 3	10
FA-SS proportions	CV-BOF 1	FA-SS ratio 75-25
FA-SS proportions	CV-BOF 2	FA-SS ratio 50-50
Cure Method	Cura 1	Ambient
Cure Method	Cura 2	Thermal

Figure A.1 - Standardized residuals presented by the compressive strength tested specimens

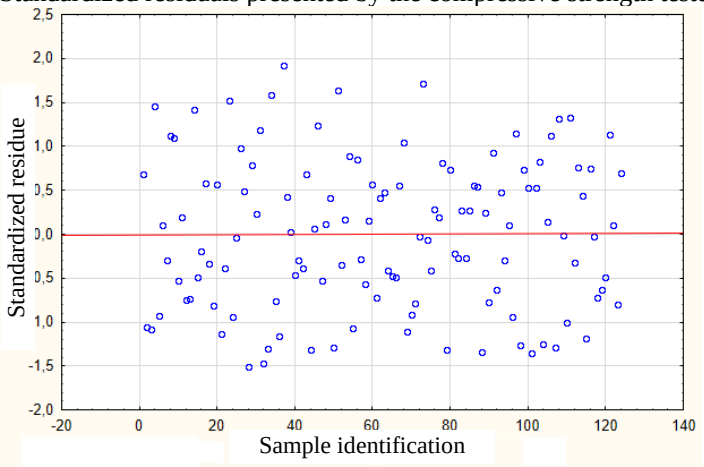

Figure A.2 - Duncan test for alkali-activated binders

Combinações	Módulo de Sílica (Adm.)	Teor de Álcali (%)	Tipo de Cura	Proporção CV-BOF	1	2	3	4	5	6	7	8	9	10	11	12	13	14	15	16	17	18	19	20	21	22	23	24	25	26	27	28	29	30	31	32	33	34	35	36
					70,9	70,5	80,1	65,2	64,5	51,5	76,3	59,3	51,6	37,0	64,3	44,9	54,7	56,1	57,0	62,0	52,3	47,5	60,4	50,7	39,4	38,9	56,8	52,1	66,3	49,5	54,4	52,5	38,0	35,0	36,7	28,1	45,5	36,8	43,6	28,8
1	MS 1	N% 1	Cura 1	CV-BOF 1		0,84	0,00	0,03	0,01	0,00	0,02	0,00	0,00	0,00	0,01	0,00	0,00	0,00	0,00	0,00	0,00	0,00	0,00	0,00	0,00	0,00	0,00	0,00	0,06	0,00	0,00	0,00	0,00	0,00	0,00	0,00	0,00	0,00	0,00	0,00
2	MS 1	N% 1	Cura 1	CV-BOF 2	0,84		0,00	0,03	0,02	0,00	0,02	0,00	0,00	0,00	0,02	0,00	0,00	0,00	0,00	0,00	0,00	0,00	0,00	0,00	0,00	0,00	0,00	0,00	0,08	0,00	0,00	0,00	0,00	0,00	0,00	0,00	0,00	0,00	0,00	0,00
3	MS 1	N% 1	Cura 2	CV-BOF 1	0,00	0,00		0,00	0,00	0,00	0,11	0,00	0,00	0,00	0,00	0,00	0,00	0,00	0,00	0,00	0,00	0,00	0,00	0,00	0,00	0,00	0,00	0,00	0,00	0,00	0,00	0,00	0,00	0,00	0,00	0,00	0,00	0,00	0,00
4	MS 1	N% 1	Cura 2	CV-BOF 2	0,03	0,03	0,00		0,76	0,00	0,00	0,03	0,00	0,00	0,70	0,00	0,00	0,00	0,00	0,21	0,00	0,00	0,07	0,00	0,00	0,00	0,00	0,00	0,64	0,00	0,00	0,00	0,00	0,00	0,00	0,00	0,00	0,00	0,00	0,00
5	MS 1	N% 2	Cura 1	CV-BOF 1	0,01	0,02	0,00	0,76		0,00	0,00	0,05	0,00	0,00	0,91	0,00	0,00	0,00	0,00	0,31	0,00	0,00	0,11	0,00	0,00	0,00	0,00	0,00	0,47	0,00	0,00	0,00	0,00	0,00	0,00	0,00	0,00	0,00	0,00	0,00
6	MS 1	N% 2	Cura 1	CV-BOF 2	0,00	0,00	0,00	0,00	0,00		0,00	0,00	0,97	0,00	0,00	0,01	0,24	0,10	0,05	0,00	0,76	0,12	0,00	0,72	0,00	0,00	0,06	0,81	0,00	0,41	0,29	0,72	0,00	0,00	0,00	0,00	0,02	0,00	0,00	0,00
7	MS 1	N% 2	Cura 2	CV-BOF 1	0,02	0,02	0,11	0,00	0,00	0,00		0,00	0,00	0,00	0,00	0,00	0,00	0,00	0,00	0,00	0,00	0,00	0,00	0,00	0,00	0,00	0,00	0,00	0,00	0,00	0,00	0,00	0,00	0,00	0,00	0,00	0,00	0,00	0,00	0,00
8	MS 1	N% 2	Cura 2	CV-BOF 2	0,00	0,00	0,00	0,03	0,05	0,00	0,00		0,00	0,00	0,05	0,00	0,08	0,21	0,31	0,29	0,01	0,00	0,65	0,00	0,00	0,00	0,31	0,01	0,01	0,00	0,07	0,01	0,00	0,00	0,00	0,00	0,00	0,00	0,00	0,00
9	MS 1	N% 3	Cura 1	CV-BOF 1	0,00	0,00	0,00	0,00	0,00	0,97	0,00	0,00		0,00	0,00	0,01	0,25	0,10	0,05	0,00	0,78	0,12	0,00	0,71	0,00	0,00	0,06	0,83	0,00	0,41	0,29	0,74	0,00	0,00	0,00	0,00	0,02	0,00	0,00	0,00
10	MS 1	N% 3	Cura 1	CV-BOF 2	0,00	0,00	0,00	0,00	0,00	0,00	0,00	0,00	0,00		0,00	0,00	0,00	0,00	0,00	0,00	0,00	0,00	0,00	0,00	0,35	0,45	0,00	0,00	0,00	0,00	0,00	0,00	0,66	0,43	0,88	0,00	0,00	0,93	0,01	0,00
11	MS 1	N% 3	Cura 2	CV-BOF 1	0,01	0,02	0,00	0,70	0,91	0,00	0,00	0,05	0,00	0,00		0,00	0,00	0,00	0,00	0,33	0,00	0,00	0,12	0,00	0,00	0,00	0,00	0,00	0,43	0,00	0,00	0,00	0,00	0,00	0,00	0,00	0,00	0,00	0,00	0,00
12	MS 1	N% 3	Cura 2	CV-BOF 2	0,00	0,00	0,00	0,00	0,00	0,01	0,00	0,00	0,01	0,00	0,00		0,00	0,00	0,00	0,00	0,01	0,30	0,00	0,03	0,03	0,02	0,00	0,01	0,00	0,08	0,00	0,01	0,01	0,00	0,00	0,00	0,79	0,00	0,58	0,00
13	MS 2	N% 1	Cura 1	CV-BOF 1	0,00	0,00	0,00	0,00	0,00	0,24	0,00	0,08	0,25	0,00	0,00	0,00		0,56	0,39	0,01	0,35	0,01	0,03	0,14	0,00	0,00	0,41	0,33	0,00	0,06	0,90	0,37	0,00	0,00	0,00	0,00	0,00	0,00	0,00	0,00
14	MS 2	N% 1	Cura 1	CV-BOF 2	0,00	0,00	0,00	0,00	0,00	0,10	0,00	0,21	0,10	0,00	0,00	0,00	0,56		0,73	0,03	0,15	0,00	0,11	0,05	0,00	0,00	0,77	0,14	0,00	0,02	0,51	0,16	0,00	0,00	0,00	0,00	0,00	0,00	0,00	0,00
15	MS 2	N% 1	Cura 2	CV-BOF 1	0,00	0,00	0,00	0,00	0,00	0,05	0,00	0,31	0,05	0,00	0,00	0,00	0,39	0,73		0,05	0,09	0,00	0,17	0,02	0,00	0,00	0,95	0,08	0,00	0,01	0,35	0,10	0,00	0,00	0,00	0,00	0,00	0,00	0,00	0,00
16	MS 2	N% 1	Cura 2	CV-BOF 2	0,00	0,00	0,00	0,21	0,31	0,00	0,00	0,29	0,00	0,00	0,33	0,00	0,01	0,03	0,05		0,00	0,00	0,49	0,00	0,00	0,00	0,05	0,00	0,10	0,00	0,01	0,00	0,00	0,00	0,00	0,00	0,00	0,00	0,00	0,00
17	MS 2	N% 2	Cura 1	CV-BOF 1	0,00	0,00	0,00	0,00	0,00	0,76	0,00	0,01	0,78	0,00	0,00	0,01	0,35	0,15	0,09	0,00		0,07	0,00	0,54	0,00	0,00	0,10	0,93	0,00	0,29	0,40	0,94	0,00	0,00	0,00	0,00	0,01	0,00	0,00	0,00
18	MS 2	N% 2	Cura 1	CV-BOF 2	0,00	0,00	0,00	0,00	0,00	0,12	0,00	0,00	0,12	0,00	0,00	0,30	0,01	0,00	0,00	0,00	0,07		0,00	0,20	0,00	0,00	0,00	0,08	0,00	0,39	0,01	0,07	0,00	0,00	0,00	0,00	0,40	0,00	0,13	0,00
19	MS 2	N% 2	Cura 2	CV-BOF 1	0,00	0,00	0,00	0,07	0,11	0,00	0,00	0,65	0,00	0,00	0,12	0,00	0,03	0,11	0,17	0,49	0,00	0,00		0,00	0,00	0,00	0,17	0,00	0,03	0,00	0,03	0,00	0,00	0,00	0,00	0,00	0,00	0,00	0,00	0,00
20	MS 2	N% 2	Cura 2	CV-BOF 2	0,00	0,00	0,00	0,00	0,00	0,72	0,00	0,00	0,71	0,00	0,00	0,03	0,14	0,05	0,02	0,00	0,54	0,20	0,00		0,00	0,00	0,03	0,58	0,00	0,60	0,17	0,50	0,00	0,00	0,00	0,00	0,04	0,00	0,01	0,00
21	MS 2	N% 3	Cura 1	CV-BOF 1	0,00	0,00	0,00	0,00	0,00	0,00	0,00	0,00	0,00	0,35	0,00	0,03	0,00	0,00	0,00	0,00	0,00	0,00	0,00	0,00		0,81	0,00	0,00	0,00	0,00	0,00	0,00	0,57	0,10	0,30	0,00	0,02	0,32	0,08	0,00
22	MS 2	N% 3	Cura 1	CV-BOF 2	0,00	0,00	0,00	0,00	0,00	0,00	0,00	0,00	0,00	0,45	0,00	0,02	0,00	0,00	0,00	0,00	0,00	0,00	0,00	0,00	0,81		0,00	0,00	0,00	0,00	0,00	0,00	0,72	0,14	0,40	0,00	0,01	0,42	0,06	0,00
23	MS 2	N% 3	Cura 2	CV-BOF 1	0,00	0,00	0,00	0,00	0,00	0,06	0,00	0,31	0,06	0,00	0,00	0,00	0,41	0,77	0,95	0,05	0,10	0,00	0,17	0,03	0,00	0,00		0,09	0,00	0,01	0,36	0,10	0,00	0,00	0,00	0,00	0,00	0,00	0,00	0,00
24	MS 2	N% 3	Cura 2	CV-BOF 2	0,00	0,00	0,00	0,00	0,00	0,81	0,00	0,01	0,83	0,00	0,00	0,01	0,33	0,14	0,08	0,00	0,93	0,08	0,00	0,58	0,00	0,00	0,09		0,00	0,32	0,37	0,88	0,00	0,00	0,00	0,00	0,01	0,00	0,00	0,00
25	MS 3	N% 1	Cura 1	CV-BOF 1	0,06	0,08	0,00	0,64	0,47	0,00	0,00	0,01	0,00	0,00	0,43	0,00	0,00	0,00	0,00	0,10	0,00	0,00	0,03	0,00	0,00	0,00	0,00	0,00		0,00	0,00	0,00	0,00	0,00	0,00	0,00	0,00	0,00	0,00	0,00
26	MS 3	N% 1	Cura 1	CV-BOF 2	0,00	0,00	0,00	0,00	0,00	0,41	0,00	0,00	0,41	0,00	0,00	0,08	0,06	0,02	0,01	0,00	0,29	0,39	0,00	0,60	0,00	0,00	0,01	0,32	0,00		0,07	0,27	0,00	0,00	0,00	0,00	0,11	0,00	0,02	0,00
27	MS 3	N% 1	Cura 2	CV-BOF 1	0,00	0,00	0,00	0,00	0,00	0,29	0,00	0,07	0,29	0,00	0,00	0,00	0,90	0,51	0,35	0,01	0,40	0,01	0,03	0,17	0,00	0,00	0,36	0,37	0,00	0,07		0,41	0,00	0,00	0,00	0,00	0,00	0,00	0,00	0,00
28	MS 3	N% 1	Cura 2	CV-BOF 2	0,00	0,00	0,00	0,00	0,00	0,72	0,00	0,01	0,74	0,00	0,00	0,01	0,37	0,16	0,10	0,00	0,94	0,07	0,00	0,50	0,00	0,00	0,10	0,88	0,00	0,27	0,41		0,00	0,00	0,00	0,00	0,01	0,00	0,00	0,00
29	MS 3	N% 2	Cura 1	CV-BOF 1	0,00	0,00	0,00	0,00	0,00	0,00	0,00	0,00	0,00	0,66	0,00	0,01	0,00	0,00	0,00	0,00	0,00	0,00	0,00	0,00	0,57	0,72	0,00	0,00	0,00	0,00	0,00	0,00		0,25	0,60	0,00	0,00	0,62	0,03	0,00
30	MS 3	N% 2	Cura 1	CV-BOF 2	0,00	0,00	0,00	0,00	0,00	0,00	0,00	0,00	0,00	0,43	0,00	0,00	0,00	0,00	0,00	0,00	0,00	0,00	0,00	0,00	0,10	0,14	0,00	0,00	0,00	0,00	0,00	0,00	0,25		0,47	0,01	0,00	0,46	0,00	0,01
31	MS 3	N% 2	Cura 2	CV-BOF 1	0,00	0,00	0,00	0,00	0,00	0,00	0,00	0,00	0,00	0,88	0,00	0,00	0,00	0,00	0,00	0,00	0,00	0,00	0,00	0,00	0,30	0,40	0,00	0,00	0,00	0,00	0,00	0,00	0,60	0,47		0,00	0,00	0,95	0,01	0,00
32	MS 3	N% 2	Cura 2	CV-BOF 2	0,00	0,00	0,00	0,00	0,00	0,00	0,00	0,00	0,00	0,00	0,00	0,00	0,00	0,00	0,00	0,00	0,00	0,00	0,00	0,00	0,00	0,00	0,00	0,00	0,00	0,00	0,00	0,00	0,00	0,01	0,00		0,00	0,00	0,00	0,78
33	MS 3	N% 3	Cura 1	CV-BOF 1	0,00	0,00	0,00	0,00	0,00	0,02	0,00	0,00	0,02	0,00	0,00	0,79	0,00	0,00	0,00	0,00	0,01	0,40	0,00	0,04	0,02	0,01	0,00	0,01	0,00	0,11	0,00	0,01	0,00	0,00	0,00	0,00		0,00	0,45	0,00
34	MS 3	N% 3	Cura 1	CV-BOF 2	0,00	0,00	0,00	0,00	0,00	0,00	0,00	0,00	0,00	0,93	0,00	0,00	0,00	0,00	0,00	0,00	0,00	0,00	0,00	0,00	0,32	0,42	0,00	0,00	0,00	0,00	0,00	0,00	0,62	0,46	0,95	0,00	0,00		0,01	0,00
35	MS 3	N% 3	Cura 2	CV-BOF 1	0,00	0,00	0,00	0,00	0,00	0,00	0,00	0,00	0,01	0,00	0,58	0,00	0,00	0,00	0,00	0,00	0,00	0,13	0,00	0,01	0,08	0,06	0,00	0,00	0,00	0,02	0,00	0,00	0,03	0,00	0,01	0,00	0,45	0,01		0,00
36	MS 3	N% 3	Cura 2	CV-BOF 2	0,00	0,00	0,00	0,00	0,00	0,00	0,00	0,00	0,00	0,00	0,00	0,00	0,00	0,00	0,00	0,00	0,00	0,00	0,00	0,00	0,00	0,00	0,00	0,00	0,00	0,00	0,00	0,00	0,00	0,01	0,00	0,78	0,00	0,00	0,00	

Table A.5 - Compressive strength at 7 days of pastes 3, 5 and 11

ID	Silica modulus (adm.)	Alkali Content (%)	Mass ratio CV-BOF (%)	Cure Method	Compr. strength (MPa)	Cure Method	Compr. strength (MPa)
3	0.75	10	75-25		16.84		63.75
3	0.75	10	75-25		17.09		60.08
3	0.75	10	75-25		17.00		57.12
5	1.25	8	75-25		34.95		56.48
5	1.25	8	75-25	Ambient	36.33	Thermal	55.19
5	1.25	8	75-25		33.82		58.14
11	0.75	8	50-50		14.05		59.79
11	0.75	8	50-50		16.94		59.27
11	0.75	8	50-50		13.81		57.08

Table A.6 - Compressive strength of paste S/N 0.75, N% 6%, FA-SS 75-25, several ages

Age (days)	Cure Method	Compr. strength (MPa)	Cure Method	Compr. strength (MPa)
3		4.48		52.15
3		4.22		55.42
3		4.54		56.54
3		4.39		-
7		16.84		58.75
7		17.09		60.08
7		17.00		57.12
7		16.72		-
14		27.95		63.45
14		32.16		55.96
14	Ambient	30.32	Thermal	60.27
14		30.04		-
28		54.94		63.36
28		50.03		63.10
28		52.21		66.35
28		49.39		-
56		57.67		60.91
56		61.16		58.62
56		64.19		61.95
112		66.02		57.28
112		66.84		59.14
112		70.99		63.87

Table A.7 - Compressive strength of alkali-activated concretes

Age (days)	Aggregate Type	Cure Method	Compr. strength (MPa)	Cure Method	Compr. strength (MPa))
28	Agr. Conv.		39.93		60.39
28	Agr. Conv.		39.9		64.39
28	Agr. Conv.		41.05		67.49
28	Agr. BSSF		34.55		51.46
28	Agr. BSSF		37.24		48.49
28	Agr. BSSF		32.91		50.66
14	Agr. Conv.	Ambient	24.54	Thermal	58.98
14	Agr. Conv.		28.15		57.45
14	Agr. BSSF		19.93		43.73
14	Agr. BSSF		21.16		45.50
7	Agr. Conv.		13.37		52.78
7	Agr. Conv.		14.45		53.82
7	Agr. BSSF		10.19		43.62
7	Agr. BSSF		11.54		41.87

Table A.8 - Ultrasonic pulse velocity (m/s) of alkali-activated concretes, 28 days

ID	Aggregate Type	Cure Method	Ultrasonic Velocity (m/s)	Cure Method	Ultrasonic Velocity (m/s)
1	Agr. Conv.	Ambient	4,187	Thermal	4,998
2	Agr. Conv.		4,096		4,777
3	Agr. Conv.		4,121		4,788
4	Agr. BSSF		4,136		4,298
5	Agr. BSSF		3,930		4,932
6	Agr. BSSF				4,923

Table A.9 - Young's modulus of alkali-activated concretes, 28 days

Young´s Modulus type	Aggregate Type	Cure Method	Young´s Modulus (GPa)	Cure Method	Young´s Modulus (GPa)
Static	Agr. Conv.	Ambient	20.54	Thermal	26.54
Static	Agr. Conv.		19.76		25.83
Static	Agr. BSSF		28.24		35.64
Static	Agr. BSSF		24.79		26.64
Resonant	Agr. Conv.		26.18		30.31
Resonant	Agr. Conv.		22.32		28.99
Resonant	Agr. BSSF		29.46		30.05
Resonant	Agr. BSSF		29.86		37.95

Table A.10 - Electrical resistivity (kΩ) of alkali-activated concretes, 28 days

ID	Aggregate Type	Cure Method	Electrical Resistivity (kΩ)	Cure Method	Electrical Resistivity (kΩ)
1	Conv. Aggr.	Ambient	1.53	Thermal	1.75
2	Conv. Aggr.		1.45		1.65
3	Conv. Aggr.		1.70		1.69
4	SS Aggr.		0.69		0.68
5	SS Aggr.		0.72		0.85
6	SS Aggr.		0.79		0.92

Table A.11 - Alkali-activated concretes chloride ion penetrability (Coulomb), 28 days

ID	Aggregate type	Chloride ion penetration (Coulomb)
1	Conv. Aggr.	8,964
2	Conv. Aggr.	9,117
3	Conv. Aggr.	8,640
4	Conv. Aggr.	9,189
5	SS Aggr.	17,577
6	SS Aggr.	17,253
7	SS Aggr.	16,902
8	SS Aggr.	17,595